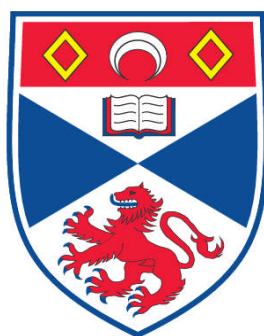


**SYNTHESIS AND CHARACTERISATION OF MATERIALS FOR  
PHOTOELECTROCHEMICAL APPLICATIONS**

**Chamnan Randorn**

**A Thesis Submitted for the Degree of PhD  
at the  
University of St. Andrews**



**2010**

**Full metadata for this item is available in  
Research@StAndrews:FullText  
at:  
<https://research-repository.st-andrews.ac.uk/>**

**Please use this identifier to cite or link to this item:  
<http://hdl.handle.net/10023/1716>**

**This item is protected by original copyright**

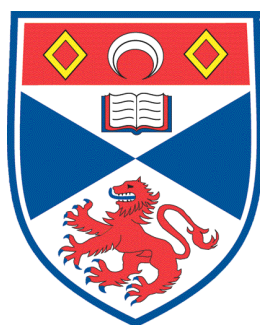
Synthesis and Characterisation of Materials for  
Photoelectrochemical  
Applications

by

Chamnan Random

A Thesis Submitted for the Degree of Doctor  
of Philosophy

University of St Andrews



October 2010



**DEDICATION**

To my grandparents and my parents

## ACKNOWLEDGEMENTS

I am deeply indebted to my supervisor, Professor John T. S. Irvine, who has made available his support in a number of ways throughout this research, including his encouragement and understanding.

This work is dedicated to my family whose love and support has made this all possible.

I gratefully acknowledge Professor Peter Robertson, Dr. Wuzong Zhou who gave me the opportunity to have a collaboration with them.

I wish to express my thanks to JTSI group members, especially Cristain Savaniu, Julie Nairn, Paul Connor, David Miller, Abul Kalam Azad, Xiaoxiang Xu, Sujitra and Pannipha for useful discussion.

I am grateful to Professor John Walton, Dr. Steve Francis, Ross Blackley and Sylvia Williamson for the instrumental support.

My warm thanks are due to technical staffs, Robert E. Cathcart, Brian Walker, Colin Smith, especially George Anthony for their help.

Particular thanks must go to my Thai friends here, Pitak, Pook, Nutt, Oh, Toey, P'Dome, Gluay.

Thanks are also due to my colleagues at Chiang Mai University, Suwaporn Luangkamin and Aroonchai Saiai for their support in Thailand.

For financial support, I wish to express my thanks to The Royal Thai Government and EPSRC.

## ABSTRACT

The preparation of visible light driven photocatalysts for photocatalytic water splitting has been achieved by a CO<sub>2</sub> free, low cost and simple novel method. Combination of peroxide based route with organic free solvent and titanium nitride, carbon free precursor and air and moisture stable, would be useful. Clear red-brown solution of titanium peroxo species was obtained by dissolution of TiN in H<sub>2</sub>O<sub>2</sub> and HNO<sub>3</sub> acid at room temperature without stirring. The resultant red brown solution is then used as a titanium solution precursor for yellow amorphous and yellow crystalline TiO<sub>2</sub> synthesis. Visible light photoactivity of the samples was evaluated by photooxidation of methylene blue and photoreduction producing hydrogen from water splitting.

The high surface area of yellow amorphous TiO<sub>2</sub> exhibits an interesting property of being both surface adsorbent and photoactive under visible light for photodecolourisation of aqueous solution of methylene blue. However, it might not be appropriate for hydrogen production.

Nanoparticulate yellow crystalline TiO<sub>2</sub> with defect disorder of Ti<sup>3+</sup> and oxygen vacancies depending upon synthesis conditions has been characterised by ESR, XPS, CHN analysis and SQUID. Single phase rutile can be produced at low temperature. It is stable at high temperature and the red shift of absorption edge increases with the treatment temperature. Yellow crystalline TiO<sub>2</sub> exhibits an interesting property of being photoactive under visible light. The best photocatalytic performance was observed for 600°C calcination, probably reflecting a compromise between red shift and surface area with changing temperature. Moreover, overall water splitting into

hydrogen and oxygen might be obtained by using this material even in air atmosphere. Photoactivity can be improved by testing under anaerobic atmosphere and/or adding sacrificial agent. Quantum efficiency under visible light is still low but comparable to other reports. The maximum efficiency varies from 0.03 % to 0.37 % for hydrogen production and from 0.03 % to 0.12 % for oxygen production, depending on photon energy and sacrificial agents.

## Table of Contents

<b>Chapter 1 Introduction</b>	1
1. Hydrogen production using renewable source	2
1.1 Corrosion of aluminium	3
1.2 Water splitting	6
1.2.1 Thermochemical water splitting	6
1.2.2 Mechano-catalytic water-splitting	8
1.2.3 Electrolysis	9
1.2.4 Solar cells water splitting	10
1.2.5 Photoelectrochemical water splitting	10
1.2.6 Photocatalytic water splitting	12
1.2.6.1 UV light driven photocatalysts	19
1.2.6.2 Visible light driven photocatalysts	20
1.2.6.3 Improvement of photoactivity	24
1.2.6.4 Overall water splitting	29
1.2.6.5 TiO <sub>2</sub> photocatalyst	31
The aim of this work	36
<b>Chapter 2 Experimental</b>	37
2.1 Synthetic procedure	40

2.1.1 Doping or loading procedure	42
2.1.2 Pt loading	42
2.2 Characterisation	43
2.2.1 XRD studies	43
2.2.2 BET measurement	45
2.2.3 EM studies	46
2.2.3.1 SEM	47
2.2.3.2 TEM	49
2.2.4 TGA studies	50
2.2.5 FT-IR studies	51
2.2.6 Elemental analysis	51
2.2.7 Magnetic measurement	52
2.2.8 UV-Visible diffuse reflectance studies	52
2.2.9 ESR studies	53
2.2.10 XPS studies	55
2.3 Photocatalytic evaluation	57
2.3.1 Photooxidation of methylene blue	57
2.3.2 Photocatalytic water splitting	58
2.4 Actinometry	64
<b>Chapter 3 Characterisation of novel coloured oxides</b>	<b>65</b>
3.1 Characterisation of yellow amorphous TiO <sub>2</sub>	66
3.1.1 TEM and BET surface area	67
3.1.2 XRD	67

3.1.3 TGA	69
3.1.4 FT-IR	71
3.1.5 UV- Visible diffuse reflectance	72
3.1.6 XPS	73
Summary	75
3.2 Characterisation of yellow crystalline TiO <sub>2</sub>	76
3.2.1 XRD	76
3.2.2 UV-Visible diffuse reflectance	83
3.2.3 TEM	86
3.2.4 FT-IR	89
3.2.5 TGA	90
3.2.6 ESR	94
3.2.7 XPS	95
3.2.8 Magnetometry	97
3.2.9 SEM	99
3.2.10 Conductivity dependence upon p(O <sub>2</sub> )	100
Summary	102

## **Chapter 4 Results and discussion on photodecolourisation of methylene blue 103**

4.1 Yellow amorphous TiO <sub>2</sub>	105
4.2 Yellow crystalline TiO <sub>2</sub>	111
4.2.1 Effect of calcination temperature	111
4.2.2 Effect of phase content	113
4.2.3 Effect of colour on visible light photoactivity	115

4.2.4 Effect of dopants or loading elements	116
4.2.5 Effect of photon energy	119
4.2.5 Effect of recyclability	121
<b>Chapter 5 Results and discussion on photocatalytic water splitting</b>	<b>122</b>
5.1 Yellow amorphous TiO <sub>2</sub>	122
5.2 Yellow crystalline TiO <sub>2</sub>	125
5.2.1 Effect of atmosphere	126
5.2.2 Effect of photon energy	129
5.2.3 Effect of sacrificial agent	131
5.2.4 Effect of calcination temperature	137
5.2.5 Effect of phase content	138
5.2.6 Effect of doping or loading elements	139
5.2.7 Effect of Pt loading	139
5.3 Efficiency	141
5.3.1 Photon flux	141
5.3.2 Quantum efficiency	142
<b>Chapter 6 conclusion</b>	<b>145</b>
<b>References</b>	<b>152</b>

# CHAPTER 1

## Introduction

As power sources currently rely on fossil fuels which are rapidly depleting, renewable and clean fuels are required for our energy future. It is envisaged that crude oil and natural gas will fail to meet demand in the near future. Apart from the energy source issue, a major environmental problem needs to be solved as greenhouse gases, especially CO<sub>2</sub> emitted from transformation of fossil fuel to electrical or motive energy, are becoming a major worldwide issue. Improvements in consumption of renewable energy sources, use of clean technology and economy of production should be addressed.

Electricity directly generated by using renewable energy such as wind, tidal, wave and solar cells might provide an alternative. However, there are some restrictions of these sources. Expensive technology and short supply distance are not convenient for investment. Additionally, energy storage is required for these technologies since the amount of electricity depends directly on periodic nature of these energy sources, for example, solar cells can produce electricity just during daytime whereas wind and wave have variations in output depending on climatic condition. As a result, clean and quiet smaller power production fuel cell technology with highly distributed network and less dependence on energy storage is interesting. Hydrogen is an ideal fuel for fuel cell technology and for sustainable energy supply in the future because of its clean conversion with no CO<sub>2</sub> emission. Hydrogen has low volumetric energy density and can easily be ignited even with a static electricity discharge or an agitation of compressed or liquid hydrogen because ignition energy is just 0.03 mJ. Hydrogen

storage still needs to be developed. Metal hydrides<sup>1</sup> have gained much attention for hydrogen storage recently because of safety concerns, although high temperature is required for such stores. Physisorption of hydrogen in a porous structure is also attractive.

Hydrogen can be produced in several ways utilising different sources such as reforming of natural gas, electrolysis of water, biomass and solar energy. In order to be successful in the hydrogen economy, hydrogen production technology needs to be well developed with strong consideration of sustainable and renewable demands. Presently, around 96% of hydrogen is produced by reforming of natural gas (48%), oil (18%) and coal gasification (30%).<sup>2</sup> However, these are not renewable sources and CO<sub>2</sub> is emitted during production. Reforming of biomass still has some limitations with low efficiency, high cost in transportation of biomass and CO<sub>2</sub> emission, although it is an abundant and renewable source. Electrolysis of water is the highest cost although new approaches are under development in order to reduce cost.<sup>3-6</sup>

## **1. Hydrogen production from renewable sources**

Hydrogen production using renewable source would be very interesting with aspect to economic and environmentally friendly issues. Corrosion of aluminium and water splitting might be a potential new sources for the hydrogen economy.

## 1.1 Corrosion of aluminium

CO<sub>2</sub> free hydrogen production can be obtained by the reaction of metal. Aluminium is a good candidate to date as it is cheap and has been used in several applications especially in packaging. It might be used in real time hydrogen production without need of hydrogen gas storage, resulting in a safer system. Producing hydrogen via corrosion of aluminium can be achieved by various reactions, both in water and hydrocarbons. Water based reaction is widely used as it is cleaner and cheaper, although incomplete reaction at surface is still the main barrier even using ball milling and surface modifying by doping or loading. By-products of aluminium corrosion, Al<sub>2</sub>O<sub>3</sub> and Al(OH)<sub>3</sub>, can be used in other applications such as water treatment and paper making. Reproducing aluminium from by-product Al<sub>2</sub>O<sub>3</sub> might be an alternative but cost is higher than the secondary aluminium production from direct aluminum recycling. However, the recycle process of by-product Al<sub>2</sub>O<sub>3</sub> consumes less energy if compared with the primary aluminium production.<sup>7-8</sup>

Water based reaction of aluminium corrosion process can be divided into 3 types as following :

- Aluminum–water reaction in neutral condition

Hydrogen can be produced by direct reaction of aluminium with water around 3.7 wt% in theory, higher than 3.3 wt% and 2.4 wt% from Mg and Zn



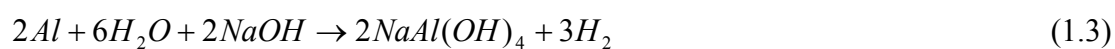
- Aluminum–water reaction at high temperature and pressure

Although the theoretical yield of hydrogen produced by aluminium directly reacting with water at low temperature is low, there is some promise at high temperature and pressure :



- Aluminum–water reaction at low temperature in alkaline environment

As the surface of aluminium in ambient atmosphere is normally coated with an oxide layer which protects against corrosion, hydroxide ion in alkaline solution is added to remove the oxide layer. NaOH is the most common hydroxide ion source used in this process.



Apart from water based reaction, alcohol hydrolysis is also reported, especially in synthesis of aluminium alkoxides.



As it is difficult to store hydrogen, hydrogen produced on board might be an alternative way for transport technology. The potential use of the aluminium-based hydrogen supply system in portable electronics such as laptop has been reported.<sup>8</sup> Fuel cells have been considered for use in electric vehicle but there are still some issues concerning fuel storage. A 225 dm<sup>3</sup> tank of hydrogen stored by conventional high pressure will be needed for a range of 400 kilometers driving whereas a 50 dm<sup>3</sup> tank containing 36 kg of aluminium can be used for a hydrogen on demand system.<sup>8</sup> Water based aluminium corrosion in alkaline condition has been used as a hydrogen source for a PEM fuel cell. It was found that 1 kg of Al would produce 56 moles of H<sub>2</sub>, approximately 1370 dm<sup>-3</sup> at STP.<sup>7</sup>

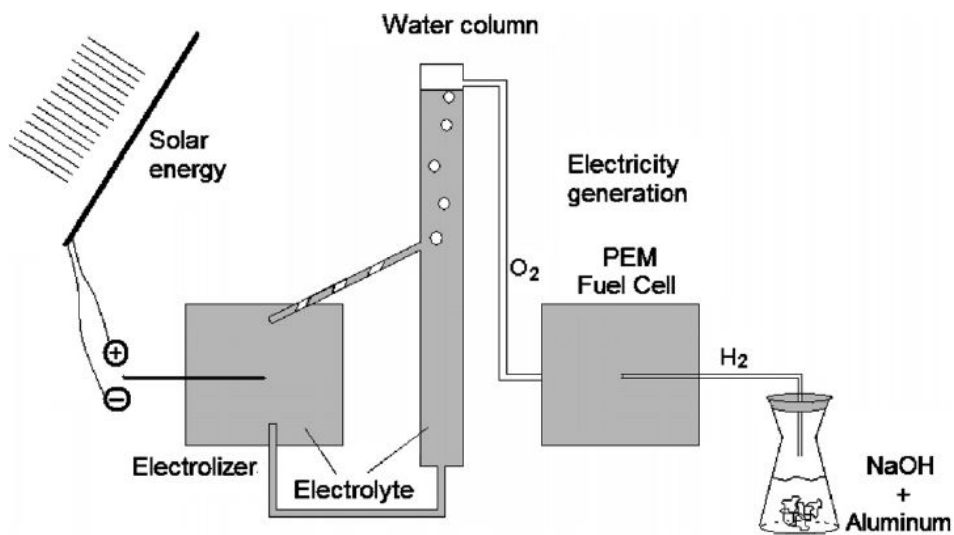


**Figure 1-1 : Electricity generated from a PEM fuel cell using the oxygen from electrolyser and the hydrogen from corrosion of aluminium as a fuel (reproduced from [7]).**

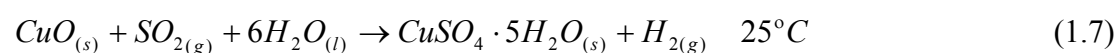
## 1.2 Water splitting

Water splitting utilising renewable energy is a promising way to produce hydrogen. Hydrogen from water splitting can be achieved by several ways such as using chemical reaction, mechanical reaction, electrical reaction and photoreaction.

### 1.2.1 Thermochemical water splitting

Thermochemical reaction might be another route to split water into hydrogen. Reactants using in this process can be incorporated with water and dissociate into hydrogen and oxygen by heating. Apart from producing hydrogen, heat is also used for recycling reactants and being precursor again. As this process uses only heat without converting to electricity and reactants can be recycled, cost for hydrogen production might be cheaper than water electrolysis. Hybrid copper oxide – copper sulphate cycle<sup>9</sup> and sulfur-iodine cycle<sup>2</sup> are promising cycles for thermochemical water splitting.

Copper oxide-copper sulphate cycle involves 2 main steps : first step, hydrogen production from reaction between copper oxide with sulphur dioxide and second step, oxygen production from decomposition of copper sulphate, which is recycled to the first step.<sup>9</sup>





The sulphur – iodine thermochemical water splitting<sup>2</sup> can be illustrated as

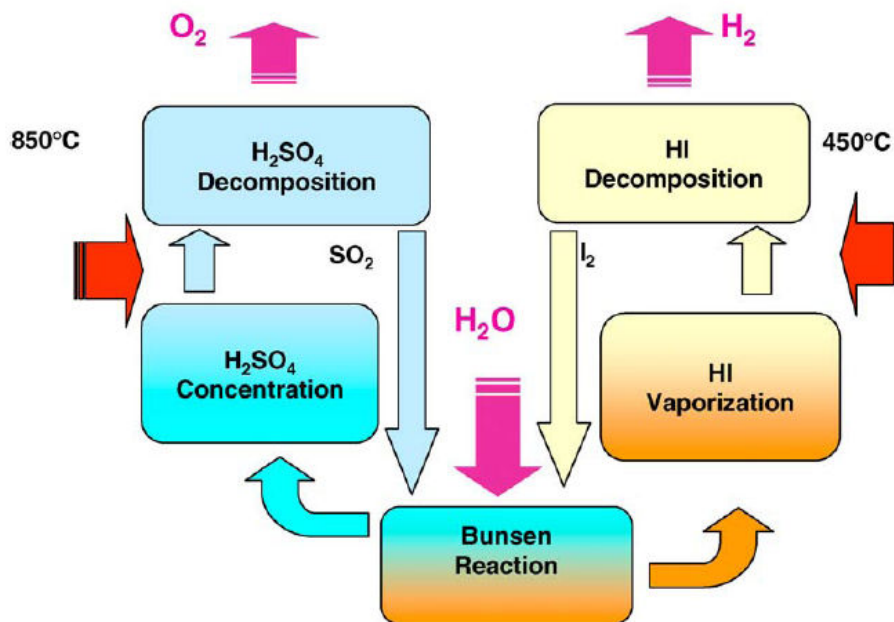
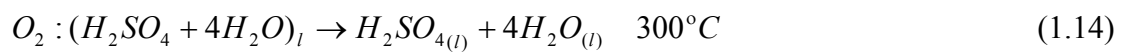
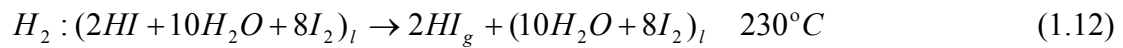
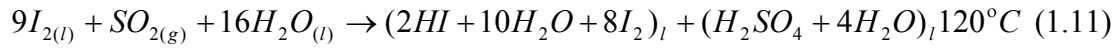
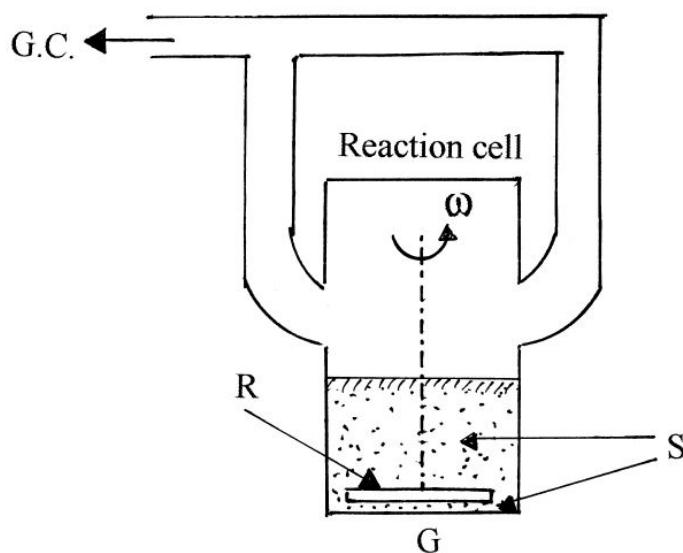


Figure 1-2 : Illustration of sulfur-iodide cycle (reproduced from [2]).

## 1.2.2 Mechano-catalytic water-splitting

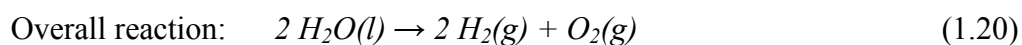
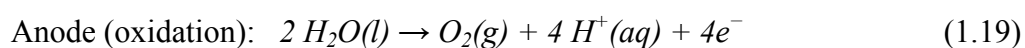
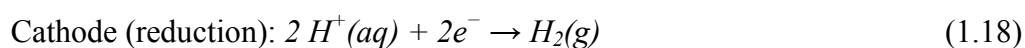
Water splitting by mechanocatalytic water splitting or mechanolysis using a p-type semiconductor might be achieved at room temperature. It can provide hydrogen and oxygen gas simultaneously. In order to achieve this process, p-type semiconductors such as  $\text{Cu}_2\text{O}$ ,  $\text{NiO}$ ,  $\text{Co}_3\text{O}_4$  and  $\text{Fe}_3\text{O}_4$  were dispersed in distilled water and then stirred by using a Teflon stirring rod. The container must be made of glass as friction between the stirring rod and glass surface is a key factor for this process because it can produce electrostatic. Semiconductor powders would be fixed in the crack space on the glass surface after frictional rubbing of stirring rod and generate holes electrostatically. Oxygen and protons will be produced by the reaction between holes and water and hydrogen can be produced by the proton and electron at the glass surface.<sup>10</sup>



**Figure 1-3 : Illustration of mechanocatalytic water splitting, G.C.: gas chromatograph, R: stirring rod; S: semiconductor powder, G: glass surface (reproduced from [10]).**

### 1.2.3 Electrolysis

Hydrogen production by electrolysis of water has the advantage of hydrogen purity but high cost for this technology is still a barrier for a practical use. Electrolysis of water can utilise conventional, nuclear or renewable electricity and is only as clean as the provided electrons. Electrolysis of water can be achieved by immersion of two electrodes connecting to electrical source in water. Hydrogen will be produced at the cathode, while oxygen will be produced at anode.



Sunlight would be a suitable renewable and sustainable energy source. Combination of sunlight and water in hydrogen production would be a promising way for hydrogen economy and fossil fuel replacement. Artificial natural photosynthesis might be affordable. There are various ways using sunlight to split water.

## 1.2.4 Solar cells water splitting

Since electricity produced by solar cells has limitation in transport losses, using a solar cells to split water into hydrogen fuel for other technologies might be more practical. Up to 20% efficiency of water splitting can be achieved by integration of solar cells and an electrolyser. Some of the benefits of this process are long term stability, scalability and high solar to hydrogen conversion efficiency. 18% efficiency can be achieved by using high efficiency solar cells type III-V,  $\text{Ga}_{0.35}\text{In}_{0.65}\text{P}-\text{Ga}_{0.83}\text{In}_{0.17}$ , and polymer electrolyte membrane electrolyser.<sup>5</sup>

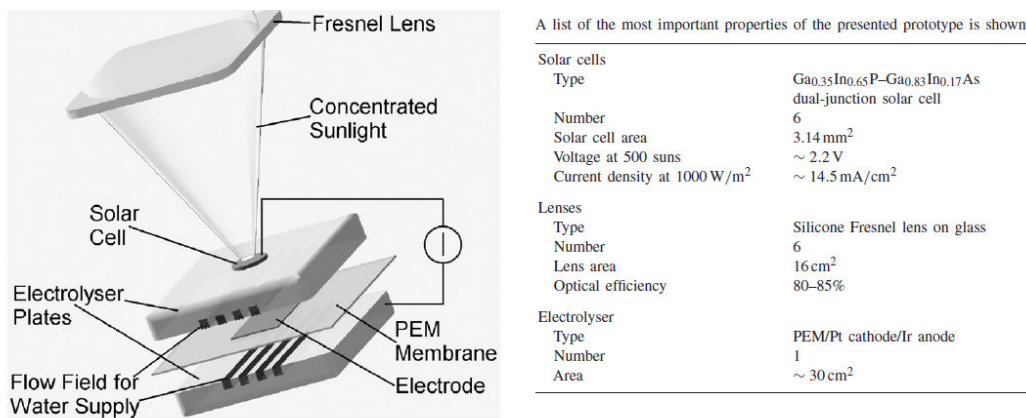


**Figure 1-4 : Illustration of solar cells water splitting (reproduced from [5]).**

## 1.2.5 Photoelectrochemical water splitting

Photoelectrochemical water splitting at a semiconductor electrode is widely known as a potential method to produce hydrogen. When a semiconductor electrode receives photon equal or exceed its band gap energy, photogenerated electrons and holes will be produced. Photogenerated electrons move through the bulk of semiconductor to the

external circuit and re-enter at the counter electrode or cathode, hydrogen is produced from the reaction between re-entered electrons with water. Oxygen will be produced at the semiconductor photoanode by reaction of water with photogenerated holes moving to the surface. The separation of photogenerated electrons and holes is induced by a thermodynamic equilibration of electric field at an interface of semiconductor electrode and electrolyte. The transfer of electric charge produces a region on each side of the junction, in the electrolyte and a thin surface region of semiconductor. The charge distribution in this region is different from a bulk material and known as a space charge layer. Conduction band and valence band in this region is normally bent upward in case of n-type semiconductor and bent downward for p-type semiconductor.<sup>5,11,12</sup>

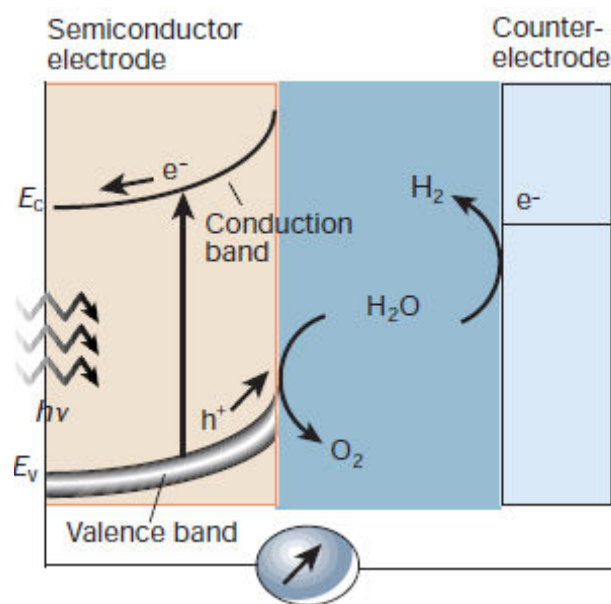


**Figure 1-5 : Principle of operation of photoelectrochemical cells based on n-type semiconductors (reproduced from [11]).**

The materials for photoelectrochemical water splitting should have band gap around 1.8 to 2.2 eV, efficient charge transfer and high surface active sites.<sup>13</sup> In addition, the

life time of photoelectrode should be discussed. The life time for 5 years of  $\text{TiO}_2$  has been reported whereas GaAs and GaP are stable for days or hours.<sup>13</sup> The efficiency of photoelectrochemical cells is dependent on experimental conditions, for example, the incident photon to electron conversion efficiency (IPCE) of 13.5% was achieved at an applied potential of 0.23 V vs. Ag/AgCl/3M KCl at 350 nm by using  $\text{ZnFe}_2\text{O}_4$ ,<sup>14</sup> while IPCE of 43.4% was obtained by using  $\text{TiO}_2$  nanotube electrode under illumination of  $100 \text{ mW/cm}^2$  in 1 M KOH solution.<sup>15</sup>

### **1.2.6 Photocatalytic water splitting**

Photocatalysis is a process that concerns activity of semiconductor material, generally, under light irradiation. It might be called a green process because it can use sunlight and ambient temperature and pressure.

Semiconductor material is the material that its electrical conductivity increases with increasing temperature. The electronic properties can be described by band theory as shown in figure 1-6. The difference of size of band gap and electron filling in valence band is used to classify materials as : metals, semiconductors and insulators. The band theory by physical approach considering the energy and wavelength of electrons in a solid.<sup>16</sup> The band is occurred by a small energy difference between adjacent levels. The molecular orbital theory is discussed from a chemical approach. When there are a large number of atoms in solid, the overlap of molecular orbitals are close in energy and continuum as a band.

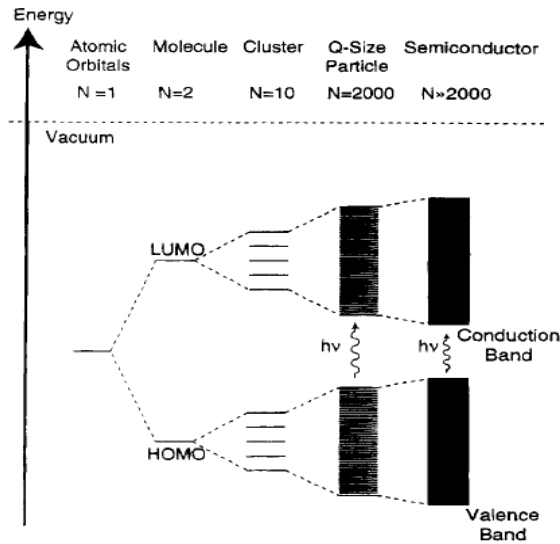


**Figure 1-6 : Illustration of band theory and quantum size effect (reproduced from [17]).**

The band gap energy ( $E_g$ ) of a semiconductor is in the range 0.5 to 3.0 eV.<sup>18</sup> It occurs by a void region between electron filled or the highest point of the valence band and empty or the lowest point of the conduction band, which is different from continuum of electronic states of metal. There are two types of band gap, a direct band gap and an indirect band gap (Figure 1-7). The optical absorption is used to identify the values of the band gap.

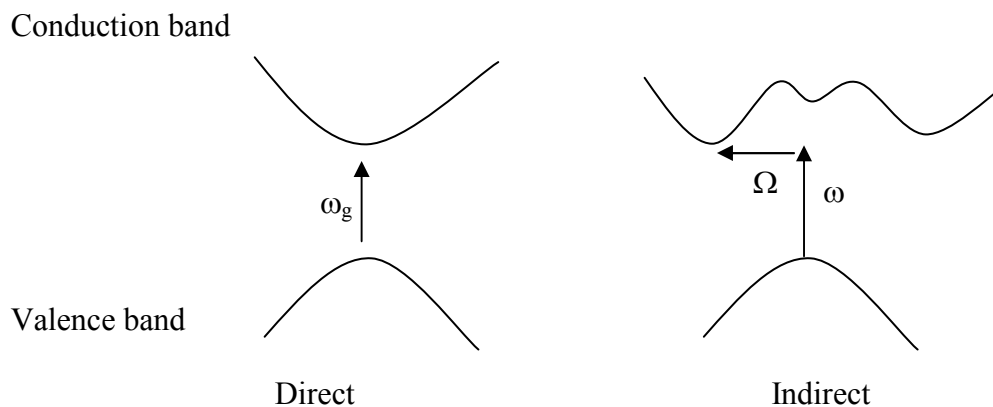


**Figure 1-7 : Direct and indirect band gap**

In the direct band gap or direct absorption process, the threshold frequency for absorption determines the band gap energy,  $E_g = h\omega_g$ , where  $\omega_g$  denotes frequency.

In the indirect band gap, the absorption threshold is at  $h\omega = E_g + h\Omega$ , where  $\Omega$  is the frequency of an emitted phonon.<sup>19</sup> The band gap energy of semiconductor materials varies depending on materials and particle size. The band gap energy of materials is different owing to the orbital hybridisation character, leading to a difference of the band position as shown in figure 1-8.

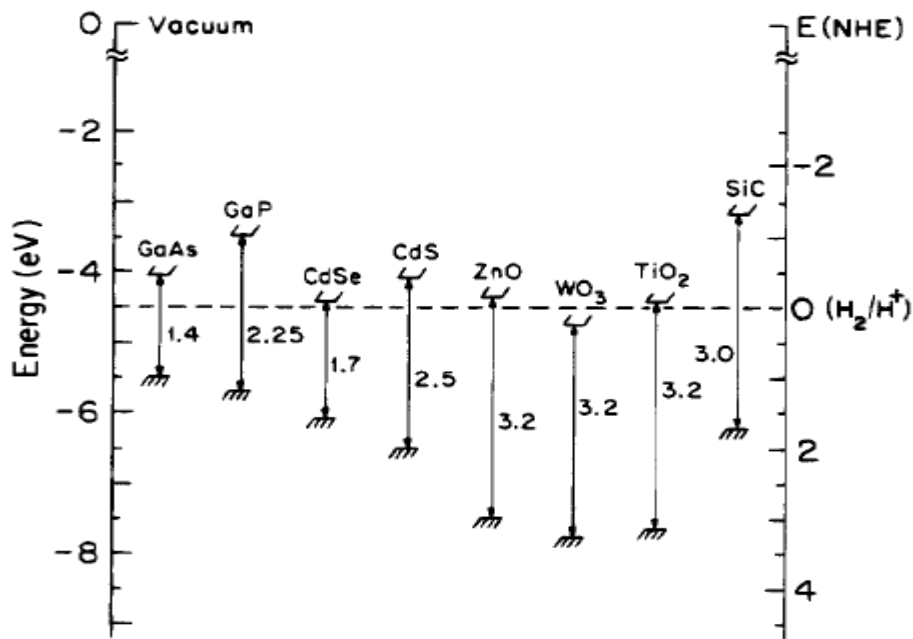
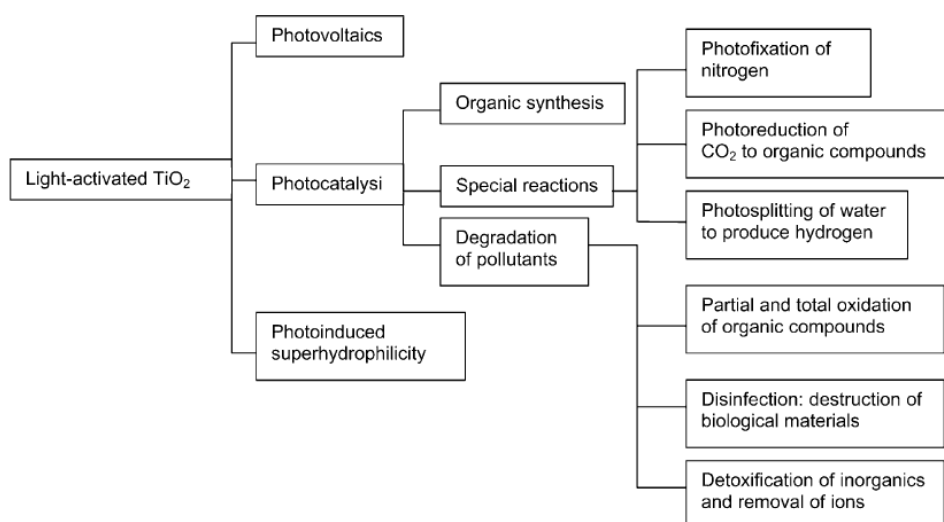


Figure 1-8 : Band edge position of various semiconductors in an aqueous solution pH=1  
(reproduced from [20])

Quantum size effect will occur when particle size of a semiconductor becomes close to de Broglie wavelength of the charge carriers or effective mass in the semiconductor. The electron and hole produced in crystallite dimension smaller than 10 nm are confined and will behave quantum mechanically producing a quantisation of discrete electronic states instead of electronic delocalisation. As a result, the band gap increases and the band edges shift yielding larger redox potentials with decreasing particle size.<sup>17,20</sup>

TiO<sub>2</sub> photoelectrochemical hydrogen production reported by Fujishima and Honda<sup>21</sup> has grown a new era of attention on semiconductor photocatalysis. Photocatalytic process is one of the utilisation of light in chemical reaction as shown in figure1-9.



**Figure 1-9 : Schematic representation of photoinduced processes (reproduced from [22])**

A semiconductor consists of essentially an electron occupied valence band and an unoccupied conduction band. Electrons will be promoted from the valence band to the conduction band and leave holes when receiving photons higher or equal to band gap energy. The valence band hole will behave as an oxidising center, whilst the conduction band electron will be a reducing center, when contact with other substances or in chemical system. This process can be used for oxidative reaction and reductive reaction depending on purpose and suitability of band position.

Mobility of photogenerated electrons and holes would have significant influence on photocatalysis efficiency. There are some possible pathways of transfer. Photogenerated electrons and holes might transfer to surface and react with the adsorbed species or solvent, resulting in chemical reaction. The probability and rate of the charge transfer correspond to the band edge position and redox potential of the adsorbed species. No chemical reaction after excitation would be possible if the photogenerated electron hole pairs recombine with the release of heat. The lifetime of each step based on laser flash photolysis measurements is different as can be seen in figure 1-10.

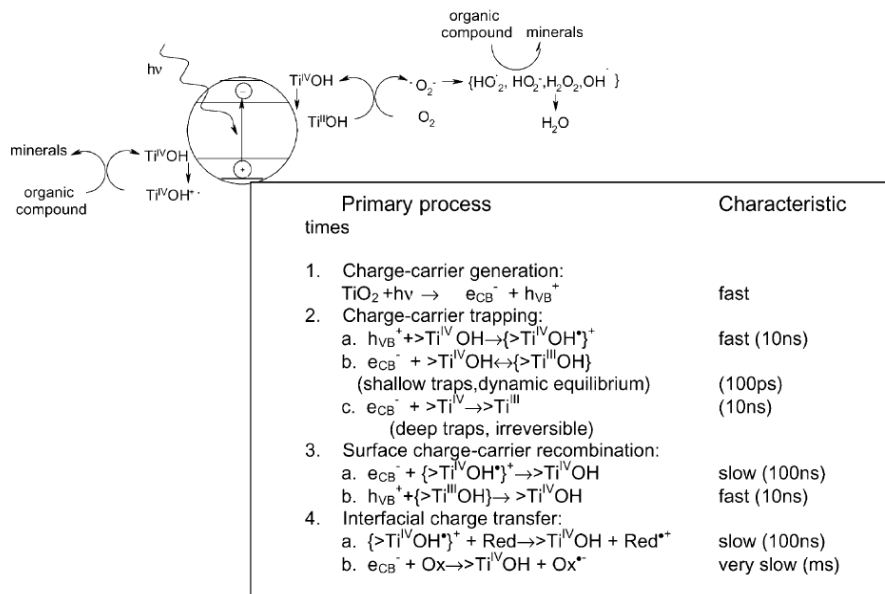


**Figure 1-10 : Illustration of characteristic times for TiO<sub>2</sub> photooxidation of organic compounds (reproduced from [22]).**

The reaction of photocatalysis process would depend upon charge transfer rate and recombination rate.

$$\phi \propto k_{CT} / (k_{CT} + k_R) \quad (1.21)$$

Where  $k_{CT}$  denotes charge transfer rate,  $k_R$  denotes recombination rate and  $\phi$  denotes quantum yield.

There are many factors affecting charge transfer rate and recombination rate, for instance, conduction and valence band positions, sacrificial agent, charge separator.

Photocatalysis can be divided into 2 main categories, photooxidation and photoreduction.

Photooxidation or advanced oxidation process is widely known for waste treatment. It can be used for decomposition a wide range of organic and inorganic pollutants, such

as dyes, pesticides, cyanide, aromatics, alkanes, halogenated hydrocarbons, odour compounds (amines, mercaptans) and dissolved metal compounds.<sup>23-26</sup>

The mechanism of this process was proposed via hydroxyl radical produced by trapping of hydroxide ion at the valence band, although some might produce by electron acceptor of oxygen at the conduction band as shown in figure 1-11. The redox potential for  $\bullet\text{OH}$  has been assigned a value of 2.8 V.

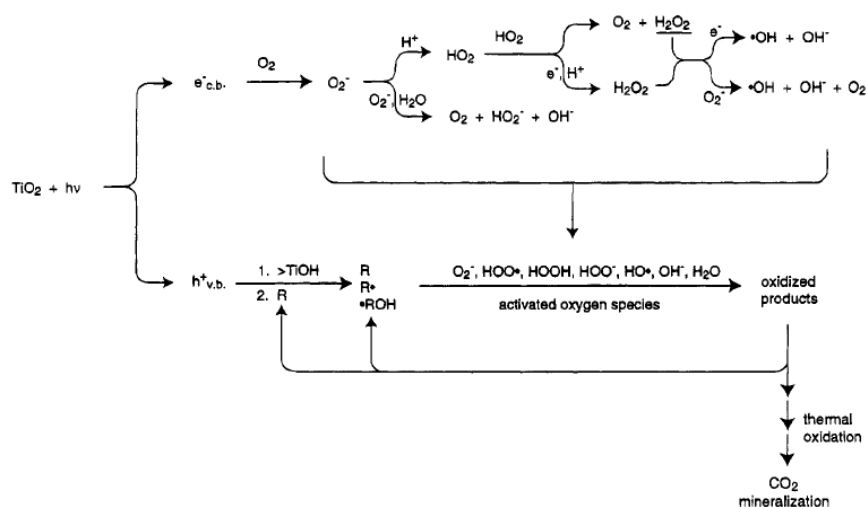


**Figure 1-11 : Active oxygen species in the photoelectrochemical mechanism (reproduced from [17]).**

In contrast to photooxidation where the valence band always has an oxidising power enough to decompose pollutants, reducing power of the conduction band position is sometimes not suitable for reaction. Consideration of the band position is important for photoreduction. Photoreduction of  $\text{CO}_2$  and  $\text{H}_2\text{O}$  has drawn attention from environmental and energy concerns. Stoichiometric water splitting is interesting for mimicking of photosynthesis system. The conduction band of photocatalyst should be more negative than hydrogen production position ( $E_{\text{H}_2/\text{H}_2\text{O}}$ ) while the valence band should be more positive than water oxidation position ( $E_{\text{O}_2/\text{H}_2\text{O}}$ ). There are several

materials such as  $\text{TiO}_2$ ,  $\text{SrTiO}_3$ ,  $\text{ZrO}_2$  that can split water into hydrogen and oxygen implying that the conduction band is accommodated, while  $\text{WO}_3$  cannot produce hydrogen because the conduction band is more positive than the hydrogen production redox potential.<sup>27</sup> The photocatalyst plays an essential role in the photocatalysis process. There are several materials that can be used as the photocatalyst. It may be divided into 2 types according to activity under different photon energy.

#### **1.2.6.1 UV light driven photocatalysts**

There are a number of materials active under UV light because most semiconductor materials can absorb UV light. White powders with band gap energy around 3.2 eV are also active. Titanium compounds such as  $\text{TiO}_2$ ,  $\text{SrTiO}_3$ ,  $\text{CeTi}_2\text{O}_6$  have been proven as good photocatalysts. The majority of studies have utilised  $\text{TiO}_2$  and this is discussed separately in section 1.2.6.5.  $\text{SrTiO}_3$  was found to be suitable for water splitting regarding the band gap energy and the flat band potential. The band gap energy of 3.2 eV with the flat band potential of conduction band at -0.6 V and the valence band at +2.6 V at pH 7 is wide enough for water splitting, which required energy 1.23 eV with the flat band potential at -0.41 V and +0.82 V.<sup>28</sup> It was also found that  $\text{CeTi}_2\text{O}_6$  thin films prepared by deposition of cerium chloride heptahydrate and titanium propoxide in ethanol shows high photoactivity on oxidation of methyl orange and eosin.<sup>29</sup>

Apart from titanate compounds, other materials such as  $\text{H}_4\text{Nb}_6\text{O}_{17}$  based compounds has also been reported as the photocatalyst for photocatalytic hydrogen production under UV light and found that activity increase with increasing co-catalyst.<sup>30</sup>

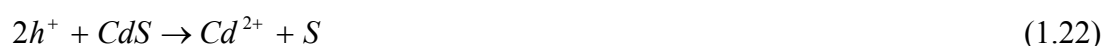
### 1.2.6.2 Visible light driven photocatalysts

As more than 95% solar light reaches earth surface is in the range of visible light (mostly 400–600 nm) and most UV is filtered by ozone layer.<sup>31</sup> Visible light driven photocatalysts have been heralded as a major breakthrough in photocatalysis process.

There are several compounds can be used either without modification or modified by doping , loading and changing morphology or structure.

#### - Unmodified materials

Narrow band gap energy of 2.4 eV of CdS is thought to be promising photocatalyst under visible light. However, photocorrosion of CdS may occur at hole and degrades to Cd<sup>2+</sup> and S.<sup>32</sup>



Sulphite need to be used as a sacrificial agent in the photocatalytic hydrogen production from water splitting in order to react with hole and also could slower the degradation of CdS.<sup>32</sup> Other metal sulphides such as AgGaS<sub>2</sub> and AgInZn<sub>7</sub>S<sub>9</sub> are also active for H<sub>2</sub> evolution from aqueous solutions containing S<sup>2-</sup> and SO<sub>3</sub><sup>2-</sup> as electron donors.<sup>33</sup>

Besides the sulphide compounds, other materials such as BiVO<sub>4</sub> and AgNbO<sub>3</sub> showed high activities for O<sub>2</sub> evolution in the presence of sacrificial agent (Ag<sup>+</sup>).<sup>33,34</sup>

Zirconate compounds are one of the most attractive photocatalysts for photocatalytic hydrogen production as its conduction band is suitable. However, ZrO<sub>2</sub> has too wide band gap energy for visible light. Lanthanide zirconium oxides, Ln<sub>2</sub>Zr<sub>2</sub>O<sub>7</sub> (Ln = La,

Ce, Nd, Sm) have been of particular interest (Figure 1-12). Among them,  $\text{Nd}_2\text{Zr}_2\text{O}_7$  and  $\text{Sm}_2\text{Zr}_2\text{O}_7$  were attractive in hydrogen production with the flat band potential of the conduction band around -0.31 and -0.52 V.

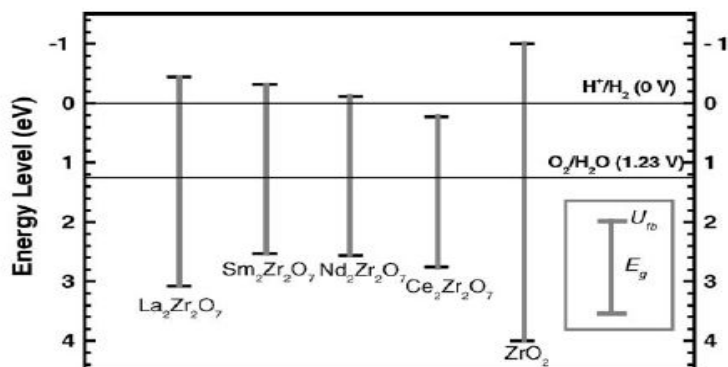


**Figure 1-12 : Illustration of band structure of  $\text{Ln}_2\text{Zr}_2\text{O}_7$  and  $\text{ZrO}_2$  (reproduced from [35])**

Solid solution of perovskite materials are also a potential candidate under visible light. Layered perovskites compounds can be a promising visible light driven photocatalysts owing to its unique character. Layered perovskites  $\text{AgLi}_{1/3}\text{Ti}_{2/3}\text{O}_2$  (Figure 1-13) and  $\text{AgLi}_{1/3}\text{Sn}_{2/3}\text{O}_2$ , band gap approximated from UV diffuse reflectance spectra around 2.7 eV, showed photooxidation activity for  $\text{O}_2$  production and decolourisation of methylene blue at 420 nm monochromatic light. Visible light responses of  $\text{AgLi}_{1/3}\text{Ti}_{2/3}\text{O}_2$  and  $\text{AgLi}_{1/3}\text{Sn}_{2/3}\text{O}_2$  were caused by the band gap excitation between conduction bands consisting of either Ti 3d or Sn 5s5p orbitals and valence bands consisting of Ag 4d orbitals.<sup>36</sup>

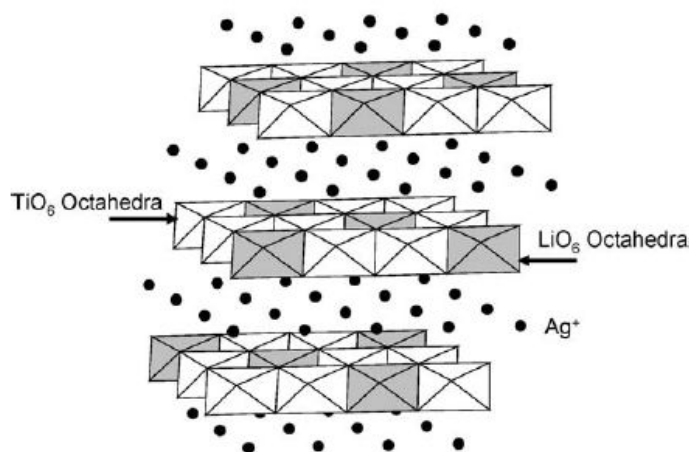


Figure 1-13 : Crystal structure of  $\text{AgLi}_{1/3}\text{Ti}_{2/3}\text{O}_2$  (reproduced from [36])

#### - Modified materials

As there are a few semiconductor materials active under visible light, narrowing the wide band gap semiconductor materials by substituting or doping other elements in the structure has been widely studied.

Layered perovskites of  $\text{CaBi}_4\text{Ti}_4\text{O}_{15}$  (Aurivillius phase),  $\text{K}_{0.5}\text{La}_{0.5}\text{Ca}_{1.5}\text{Nb}_3\text{O}_{10}$  (Dion–Jacobson phase), and  $\text{Sr}_3\text{Ti}_2\text{O}_7$  could also develop to be visible light photocatalyst by substituting lead (Pb) for Ca in  $\text{CaBi}_4\text{Ti}_4\text{O}_{15}$  and Sr in  $\text{Sr}_3\text{Ti}_2\text{O}_7$  or doping Pb into  $\text{K}_{0.5}\text{La}_{0.5}\text{Ca}_{1.5}\text{Nb}_3\text{O}_{10}$  owing to hybridisation of Pb 6s orbital and O 2p orbital, resulting in narrower of band gap energy, as shown in figure 1-14.<sup>37</sup>

Band gap energies and photocatalytic activities for H <sub>2</sub> and O <sub>2</sub> evolution for different structure types						
Structure type	Phase	E <sub>g</sub> (eV)	Photoreduction		Photooxidation	
			H <sub>2</sub> evolution (μmol h <sup>-1</sup> )	Φ <sub>H<sub>2</sub></sub> (%)	O <sub>2</sub> evolution (μmol h <sup>-1</sup> )	Φ <sub>O<sub>2</sub></sub> (%)
Aurivillius	CaBi <sub>4</sub> Ti <sub>4</sub> O <sub>15</sub>	3.36	0	—	0	—
	PbBi <sub>4</sub> Ti <sub>4</sub> O <sub>15</sub>	3.02	11.2	0.27	433	21
	CaBi <sub>2</sub> Nb <sub>2</sub> O <sub>9</sub> <sup>a</sup>	3.18	—	—	—	—
	PbBi <sub>2</sub> Nb <sub>2</sub> O <sub>9</sub> <sup>b</sup>	2.88	3.2	0.4	520	29
Dion–Jacobson	K <sub>0.5</sub> La <sub>0.5</sub> Ca <sub>1.5</sub> Nb <sub>3</sub> O <sub>10</sub>	3.44	0	—	0	—
	K <sub>0.5</sub> La <sub>0.5</sub> Ca <sub>0.75</sub> Pb <sub>0.75</sub> Nb <sub>3</sub> O <sub>10</sub>	3.09	Traces	—	124	6
	K <sub>0.5</sub> La <sub>0.25</sub> Bi <sub>0.25</sub> Ca <sub>0.75</sub> Pb <sub>0.75</sub> Nb <sub>3</sub> O <sub>10</sub>	3.06	Traces	—	168	8
Ruddlesden–Popper	Sr <sub>1</sub> Ti <sub>2</sub> O <sub>7</sub>	3.31	0	—	0	—
	PbTiO <sub>3</sub>	2.98	13.6	0.33	523	28

<sup>a</sup>Photocatalytic activity not measured.

<sup>b</sup>Photocatalytic activity measured with light source equipped with an UV cut-off filter ( $\lambda > 420$  nm).

**Figure 1-14 : Band gap energies and photoactivity for H<sub>2</sub> and O<sub>2</sub> evolution for various layered perovskites (reproduced from [37]).**

Dopants might be a main factor for extending absorption edge to visible light. There are a number of reports studied an effect of doping on photoactivity. InTaO<sub>4</sub> can be used for hydrogen and oxygen production from water splitting but the photoactivity was enhanced when it is doped with Ni around 0.05-0.2 mol%.<sup>38</sup> As well as InTaO<sub>4</sub>, lanthanide titanate compound such as La<sub>2</sub>Ti<sub>2</sub>O<sub>7</sub> exhibits a potential candidate for water splitting when doped with Cr<sup>3+</sup> or Fe<sup>3+</sup>. It showed narrower band gap energy to 2.2 and 2.6 eV, consistent with their hydrogen production. Cr doped La<sub>2</sub>Ti<sub>2</sub>O<sub>7</sub> can produce more hydrogen than Fe doped La<sub>2</sub>Ti<sub>2</sub>O<sub>7</sub>.<sup>39</sup>

Apart from metal ion doping, anions such as S, C, N, F are useful for extending photoactivity toward visible light. S, C co-doped SrTiO<sub>3</sub> gave a red shift into visible light region and the photooxidation of 2-propanol increases 2 times.<sup>40</sup> F doped SrTiO<sub>3</sub> prepared by mechanochemical reaction of SrF<sub>2</sub> with SrTiO<sub>3</sub> showed photoactivity for NO removal. The optimum composition is 5 mol% of SrF<sub>2</sub> and 95 mol% of SrTiO<sub>3</sub>.<sup>41</sup> Moreover, some zirconate compounds can be modified to absorb over wide range of visible light by doping. Red color of Nb<sub>2</sub>Zr<sub>6</sub>O<sub>17</sub> powder can be obtained by nitrogen

doping. The oxynitride  $\text{Nb}_2\text{Zr}_6\text{O}_{17-x}\text{N}_x$  provided the quantum yield of 13.5% in photocatalytic hydrogen production from decomposition of hydrogen sulphide under visible light irradiation.<sup>42</sup>

### **1.2.6.3 Improvement of photoactivity**

In order to improve efficiency of photocatalysis, several techniques of material modification have been explored. As physical properties of materials influence the photoactivity, different physical properties of surface or structure such as nanoparticle, nanotube, Z scheme, defect disorder, including layered and core-shell structure would be useful.

- Influence of particle size.

Nanoparticle size can accelerate photoactivity as can be seen by the observation that nanocrystal  $\text{BiVO}_4$  could decompose methyl orange around 8% better than sample prepared by solid state method.<sup>43</sup>

- Influence of high surface area materials

It is widely known that surface area plays a vital role on photoactivity. There are many attempts to increase photoactivity by configuring surface properties. High surface area 200-300  $\text{m}^2/\text{g}$  of coloured Cu or Ni incorporated mesoporous tantalum oxide is found to be helpful in acceleration of photoactivity of tantalum oxide for water splitting.<sup>44</sup>

- Influence of Z scheme construction.

Z scheme has been confirmed in assisting photoactivity. Construction of Z scheme between Rh doped SrTiO<sub>3</sub>, which produced only hydrogen, and BiVO<sub>4</sub> or WO<sub>3</sub> can generate both H<sub>2</sub> and O<sub>2</sub>.<sup>45</sup> In addition, mimicking of Z-scheme by using redox mediator of I<sup>-</sup>/IO<sub>3</sub><sup>-</sup> in the combination of Pt–WO<sub>3</sub> and the Pt loaded on Cr-Ta doped SrTiO<sub>3</sub> can split water.<sup>27</sup>

- Influence of structure character : nanotube, nanosheet, layered, core-shell

Since nanotube and nanosheet structure of several materials can be prepared, the utilisation of these structures in photocatalysis has been studied extensively. It has been reported that single wall carbon nanotubes irradiated with visible light from camera flash in vacuum can split water into hydrogen about 80 mol % in one flash (0.1-0.2J/cm<sup>2</sup>, 8 ms) and can reach 900 ppm of the mass.<sup>46</sup> Whereas titanium nanosheet coated on CdS photoelectrodes have been revealed for visible light photooxidation of water. Unfortunately, titanium nanosheet coating is not useful for photooxidation of water, probably photogenerated holes could not transfer across titanium nanosheet.<sup>47</sup>

Layered perovskite Sr<sub>2</sub>(Ta<sub>1-x</sub>Nb<sub>x</sub>)<sub>2</sub>O<sub>7</sub> controlling band gap energy by solid solution were studied to explore the photocatalytic water splitting. A Sr<sub>2</sub>(Ta<sub>0.75</sub>Nb<sub>0.25</sub>)<sub>2</sub>O<sub>7</sub> photocatalyst showed a relatively high activity among the solid solutions of Sr<sub>2</sub>(Ta<sub>1-x</sub>Nb<sub>x</sub>)<sub>2</sub>O<sub>7</sub> (0 < X < 1).<sup>48</sup> The results of layered perovskite Sr<sub>2</sub>(Ta<sub>1-x</sub>Nb<sub>x</sub>)<sub>2</sub>O<sub>7</sub>

is consistent with  $\text{Sr}_3\text{Ti}_2\text{O}_7$ , layered perovskite Ruddlesden–Popper phase.  $\text{Sr}_3\text{Ti}_2\text{O}_7$  also exhibits a promising photoactivity under UV light without co-catalyst.<sup>49</sup>

Ikeda et al. studied the effect of core-shell structure on photoactivity. Partially modified core-shell structure of Pt loaded  $\text{SrTiO}_3$ -silica with fluoroalkylsilylation agent has been compared with conventional suspension system in overall water splitting. The former has higher photoactivity than the latter, probably, indicating that different properties of photocatalyst can be obtained by different synthetic method.<sup>50</sup>

#### - Influence of defect disorder

Defect disorder of cerium titanate compounds (Figure 1-15) have been getting attention on photoactivity under visible light because of their colours, such as yellow, red, and grey. Defect disorder of oxygen vacancies ( $V_o^{\bullet\bullet}$ ,  $V_o^\bullet$ ,  $V_o^x$ ), interstitial sites ( $O_i'$ ,  $O_i''$ ,  $O_i^x$ ) and holes on lattice oxygen ( $O_o^\bullet$ ) might act as colour centers.<sup>51</sup>  $\text{Ce}_2\text{Ti}_2\text{O}_7$  (red-brown),  $\text{Ce}_{2/3}\text{TiO}_3$  (black, metal like behaviour), and  $\text{Ce}_4\text{Ti}_9\text{O}_{24}$  (brown), with mainly  $\text{Ce}^{3+}$ , and  $\text{CeTiO}_4$  (yellow) and  $\text{CeTi}_2\text{O}_6$  (pale yellow), with mainly  $\text{Ce}^{4+}$ , showed some activity on photooxidation of MB under visible light but composite powder of  $\text{CeTiO}_4$  with  $\text{SrTiO}_3$  has higher photocatalytic activity.<sup>51</sup> Moreover,  $\text{Ce}^{4+}$ - $\text{TiO}_2$  powder, predominant anatase titania and crystalline cerium titanate (11.18 wt.%  $\text{Ce}_x\text{Ti}_{1-x}\text{O}_2$ ), has shown higher efficiency than nanocrystallites in respect of photocatalytic activity.<sup>52</sup>

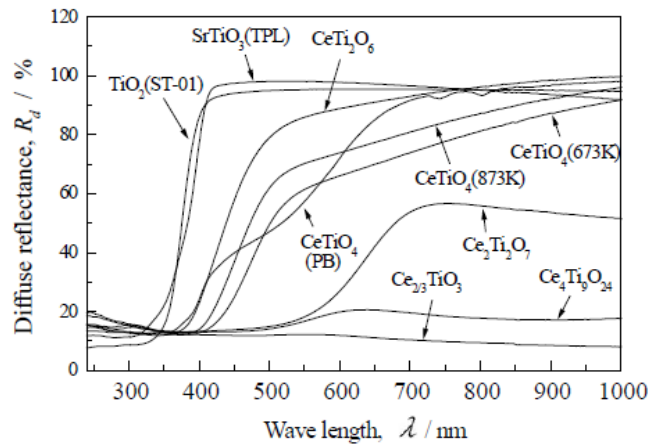


**Figure 1-15 : Diffuse reflectance spectra of the cerium titanates (reproduced from [51]).**

- Influence of the incorporation of unique structure.

Incorporation of photocatalyst material with other unique structure material has been investigated in many ways in order to improve efficiency. Shangguan<sup>53</sup> has reviewed photoactivity rendered by modification of materials and found that pillared layered structure might be interesting for hydrogen production. Pillared layered compounds prepared of interlayer compound host such as  $\text{KTiNbO}_5$ ,  $\text{K}[\text{Ca}_2\text{Na}_{x-3}\text{Nb}_x\text{O}_{3x+1}]$  and pillar metal oxide has been investigated for photoactivity improvement. Silica clusters-pillared  $\text{Ca}_2\text{Nb}_{2.9}\text{Cr}_{0.1}\text{O}_{10}$  layers produced the surface area of  $239 \text{ m}^2/\text{g}$ . Intercalation of CdS in  $\text{K}_2\text{Ti}_{3.9}\text{Nb}_{0.1}\text{O}_9$  evolved hydrogen higher than CdS because photogenerated electrons can be quickly move.<sup>53</sup>

Nafion was also used for this purpose as well. Coating  $\text{TiO}_2$  is one of the techniques to activate  $\text{TiO}_2$  under visible light. Nafion, perfluorinated polymer, has been successfully coated on  $\text{TiO}_2$  and active under visible light for photocatalytic

degradation of dye such as methylene blue and rhodamine. Nafion layer might retard the charge recombination.<sup>54</sup>

In addition to Nafion, fullerene is inspired by scientists. Photodegradation rates could be enhanced by increase charge separation. High migration efficiency at the surface could be modified by adsorbed fullerene, C60, on the surface. C60-modified Bi<sub>2</sub>WO<sub>6</sub> photocatalyst has been reported for improvement of photodecomposition of dyes. Conjugation of  $\pi$  system at the interface is thought to be affected at the surface.<sup>55</sup>

Photocatalytic decomposition of NO<sub>x</sub>(NO, N<sub>2</sub>O) into N<sub>2</sub> and O<sub>2</sub> and photoreduction of CO<sub>2</sub> in water to produce CH<sub>4</sub> and CH<sub>3</sub>OH has been achieved by using selective and unique framework structure of zeolites containing transition metal oxide (Ti, V, Mo, Cr) or incorporation of transition metal ions (Cu<sup>+</sup>, Ag<sup>+</sup>, Pr<sup>3+</sup>)(Figure 1-16). Rapid separation of photogenerated electrons and photogenerated holes is the advantage of this system.<sup>56</sup>

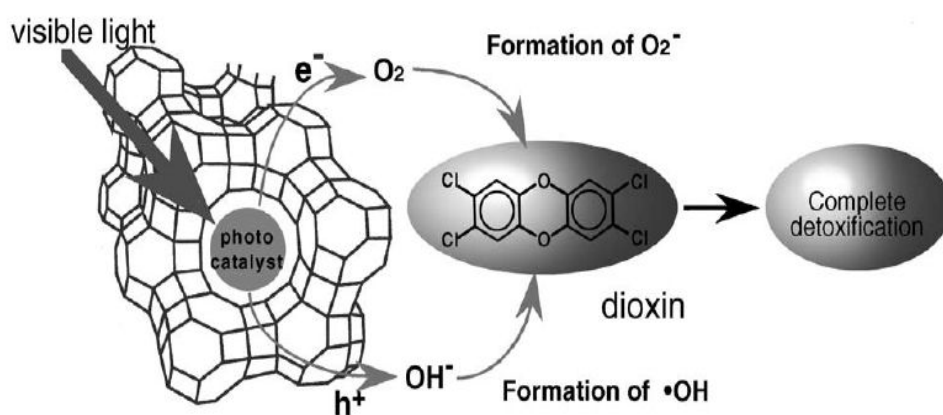


**Figure 1-16 : Illustration of photoactivity of zeolite containing photocatalyst (reproduced from [56]).**

#### - Influence of charge migration

As mention earlier about the improvement of photoactivity by increase of surface area and incorporation of other unique character materials, charge separation might be another factor for that improvement. Charge migration was confirmed as a useful factor for efficiency improvement by the photoactivity of heterogeneous microjunctions of  $\text{TiO}_2\text{-Sr}_{0.95}\text{La}_{0.05}\text{TiO}_{3+\delta}$  on photodegradation of methylene blue. The photodecolourisation of methylene blue was several times better than naked  $\text{TiO}_2$ .<sup>57</sup> Omata and Matsuo also found that the p-n junction of composite between n-type material and p-type material was helpful in photocatalysis process. Composite materials of n-type conductor, with p-type conductor,  $\text{SrZr}_{0.95}\text{Y}_{0.05}\text{O}_{3-\delta}$ ,  $\text{CaZr}_{0.95}\text{Y}_{0.10}\text{O}_{3-\delta}$  and  $\text{CaZr}_{0.95}\text{Ga}_{0.05}\text{O}_{3-\delta}$  have been revealed on photodegradation of methylene blue and formic acid. Results confirmed the higher photoactivitiy was obtained via separation of photogenerated electrons and photogenerated holes through the p-n junction.<sup>58</sup>

#### 1.2.6.4 Overall water splitting

Even though there are several materials that can split water, there are only a few materials that can split water into hydrogen and oxygen simultaneously. Most materials need to have sacrificial agent in order to inhibit the recombination rate of electron hole pairs, resulting in producing just only hydrogen or oxygen.

Tantalum compounds are interesting for overall water splitting as Ni-mixed mesoporous tantalum oxide can decompose water into stoichiometric  $\text{H}_2$  and  $\text{O}_2$  under

ultraviolet irradiation<sup>44</sup> and alkali and alkaline earth tantalates have much attention as a promising group of photocatalyst materials for overall water splitting into H<sub>2</sub> and O<sub>2</sub> because it can split water even without co-catalyst. The photoactivity can be improved by NiO loading and doping, and NiO loading on La doped NaTaO<sub>3</sub> has highest activity. Decrease in particle size rendered by doping was thought to be main factor.<sup>59</sup> Besides tantalum compounds, Arai et al. achieved overall water splitting into H<sub>2</sub> and O<sub>2</sub> ratio of 2 by using divalent metal ion, Zn<sup>2+</sup>, Mg<sup>2+</sup> and Be<sup>2+</sup> doped GaN as photocatalysts under UV light. Both H<sub>2</sub> and O<sub>2</sub> were produced from the initial stage of UV light illumination. Divalent metal ion dopants are thought to produce p-type GaN, leading to an increase in concentration and mobility of holes.<sup>60</sup> Moreover, an inert indium tin oxide electrode in phosphate-buffered water containing Co<sup>2+</sup>, around 1:2 ratio, has also imitated natural photosynthesis to rearrange bonds of water to O<sub>2</sub> and H<sub>2</sub>. HPO<sub>4</sub><sup>2-</sup> is the proton acceptor in the O<sub>2</sub> producing reaction.<sup>4</sup>

Maeda et al. also reported an influence of oxide compounds loading on oxynitride compound. (Rh<sub>2-y</sub>Cr<sub>y</sub>O<sub>3</sub>) loaded (Ga<sub>1-x</sub>Zn<sub>x</sub>)(N<sub>1-x</sub>O<sub>x</sub>) can split water into H<sub>2</sub> and O<sub>2</sub> under visible light. The photoactivity depends on pH because of corrosion of co-catalyst and is independent of gas pressure.<sup>61</sup> The co-catalyst might play an important factor for overall water splitting as can also be seen from BaCeO<sub>3</sub>, which cannot split water simultaneously. It can achieve overall water splitting when using RuO<sub>2</sub> cocatalyst.<sup>62</sup>

#### 1.2.6.5 TiO<sub>2</sub> photocatalyst

Among the photocatalysts, titanium dioxide (TiO<sub>2</sub>) has been the most studied material in these fields of photocatalysis and solar energy conversion due to its activity, it being chemically and biologically inert, strong oxidising power, cost-effectiveness, long-term stability and environmentally friendly.<sup>26</sup> Additionally, the conduction band and the valence band are suitable for photocatalytic water splitting into hydrogen and oxygen. TiO<sub>2</sub> has a potential to be used in several applications such as gas sensors, photovoltaic cells, photonic crystals. It is the most widely used photocatalyst as it can decompose organic substances, inorganic substances and bacteria. It can be applied for many applications such as in self-cleaning glass, water and air purification and antibacterial coatings. It has been used in industry as a capacitors, ink printer heads, sensors for laser printers and ultrasonic devices. It has also been used as some heat-mirror windows such as TiO<sub>2</sub>/Ag/TiO<sub>2</sub> in architectural energy conservation, which reflect invisible solar radiation of 800–2500 nm, and pigment in ultraviolet-protecting cosmetics.<sup>63,64</sup> Since TiO<sub>2</sub> active as a photocatalyst under UV light, there is some research on the photoactivity of TiO<sub>2</sub> used in sunscreen. TiO<sub>2</sub> used in sunscreen is normally modified to inhibit their photoactive and leave a reflective property dominant. However, some cellular damage in cultured cell lines from photoactive of TiO<sub>2</sub> in some sunscreen has been reported.<sup>65</sup>

TiO<sub>2</sub> is the most attractive candidates for solar energy conversion because of its stability and wide range of modification. There are three main phases of TiO<sub>2</sub> : rutile, anatase and brookite. Single phase of anatase and rutile phase can be synthesised in a



light would be obtained from solar energy, resulting in efficiency limitation. For example, a limit of water-splitting efficiency under AM1.5 global solar illumination is 2.2% for rutile and 1.3% for anatase, lower than 10% required for economic hydrogen production.<sup>67,68</sup>

In order to improve efficiency, there are a number of articles reported photoactivity of modified TiO<sub>2</sub> such as unusual but interesting morphology of nanoflowers TiO<sub>2</sub> films (Figure 1-18),<sup>69</sup> zeolite supported TiO<sub>2</sub>,<sup>70</sup> nanotube TiO<sub>2</sub>,<sup>71</sup> doped TiO<sub>2</sub>,<sup>72</sup> Hydrated TiO<sub>2</sub><sup>73</sup> and Porous TiO<sub>2</sub>.<sup>74</sup>

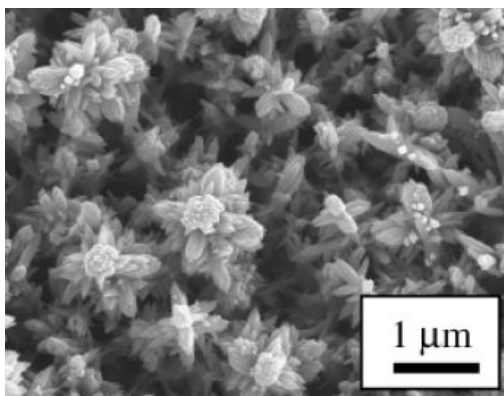


**Figure 1-18 : image of nanoflower TiO<sub>2</sub> (reproduced from [69]).**

#### **- Visible light driven TiO<sub>2</sub> photocatalysts**

Visible light active materials would be very attractive to photocatalysis or solar energy conversion applications as high efficiency might be reached for the practical applications. Great effort has been made on the photocatalytic degradation of pollutants on the purpose of environment and photocatalytic water splitting on the purpose of renewable energy by surface and matrix modification of TiO<sub>2</sub>. The surface

modification of  $\text{TiO}_2$  is virtually on the basis of the sensitisation, which occurs via the electron transfer between the modifier potential energy and the conduction band of  $\text{TiO}_2$ .<sup>75</sup>

Nonstoichiometric rutile  $\text{TiO}_{2-x}$  seems to be an alternative material for visible light applications because absorption edge is extend to visible light. Various nonstoichiometric  $\text{TiO}_{2-x}$  have been prepared by reducing  $\text{TiO}_2$  in 7 vol% hydrogen at various temperatures.  $\text{Ti}_x\text{O}_{2x-1}$  phase may coexist with rutile phase when reducing at higher temperatures.  $\text{TiO}_{2-x}$  when  $x=0.006$  was found to be the best photoanode in photoelectrochemical cell.<sup>76</sup>

Doping  $\text{TiO}_2$  with cations or anions also increases absorption toward visible light. There are a number of results under visible light obtained by this modification. Nitrogen-doped  $\text{TiO}_2$  is widely examined as a visible light photocatalyst because of its simple and extent of precursors. Pd loaded  $\text{TiO}_{2-x}\text{N}_x$  prepared by nitridation of  $\text{TiO}_2$  with alkylammonium salts at room temperature was active in photooxidation of MB and ethylene.<sup>68</sup> Nitrogen doped  $\text{TiO}_2$  prepared by sol-gel method using  $\text{NH}_4\text{Cl}$ ,  $\text{NH}_3$ ,  $\text{N}_2\text{H}_4$ ,  $\text{NH}_4\text{NO}_3$  and  $\text{HNO}_3$  as nitrogen sources have been confirmed the presence of residual thermally stable single N-atom impurities either as bulk diamagnetic,  $\text{N}^-$ , centers or as bulk paramagnetic,  $\text{N}^+$ , centers. Substitutional or favour of interstitial of nitrogen atom would be occupied in the structure and narrower band gap energy into visible light absorption, as shown in figure 1-19.

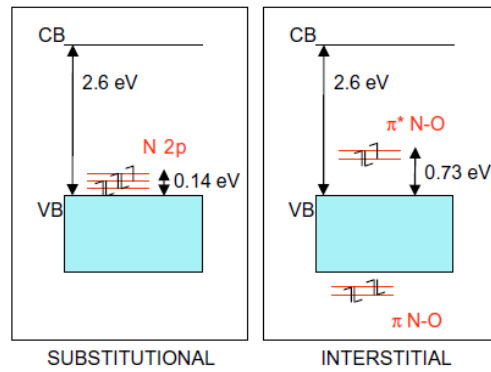


**Figure 1-19 : Electronic structure of N doped TiO<sub>2</sub> (reproduced from [77]).**

However, There is some work suggesting that nitrogen might just act as a blocker for reoxidation whilst oxygen deficient sites formed in grain boundary play an essential role in visible light activity.<sup>78</sup>

TiO<sub>2</sub> doped with transition metal ions also exhibits visible light responses such as TiO<sub>2</sub> co-doped with antimony and chromium, which evolved O<sub>2</sub> from an aqueous silver nitrate solution,<sup>79</sup> and V<sup>4+</sup> doped TiO<sub>2</sub>.<sup>31</sup> However, no improvement might be found after doping, for example, Cr<sup>3+</sup> and Mo<sup>5+</sup> doped TiO<sub>2</sub>.<sup>80</sup>

In addition to doping, composite powders could be useful. Composite powder of TiO<sub>2</sub> and polymeric carbon nitride, C<sub>3</sub>N<sub>4</sub> (Figure 1-20), can achieve photocatalytic hydrogen production under visible light. Electron injection from visible light active yellow C<sub>3</sub>N<sub>4</sub> to TiO<sub>2</sub> was proposed. However, C<sub>3</sub>N<sub>4</sub> itself can be a photocatalyst with efficiency around 0.1% under wavelength 420-460 nm after modification with Pt.<sup>6</sup>

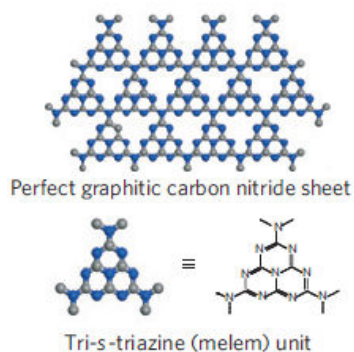


**Figure 1-20 : Crystal structure of graphitic carbon nitride (reproduced from [6]).**

### **The aim of this work**

As mention earlier about the requirement of renewable and clean fuels for our energy future, photocatalytic water splitting using water and solar energy as a renewable and carbon dioxide free power sources would be interesting for producing hydrogen that may be used as a fuel for our energy future. However, the efficiency of this process is still low as most photocatalysts cannot absorb visible light. Visible light active materials would be very attractive as high efficiency might be reached. Titanium dioxide ( $\text{TiO}_2$ ) has been the most promising material due to its activity, long-term stability and the conduction band and the valence band edges are suitable for photocatalytic water splitting into hydrogen and oxygen. Therefore, this work is focusing on the synthesis and characterisation of visible light driven  $\text{TiO}_2$  photocatalysts by a novel, simple and clean method, including the investigation of its photoactivity under visible light. Visible light photoactivity of the samples are evaluated by photooxidation of methylene blue and photoreduction of hydrogen from water splitting.

## CHAPTER 2

### Experimental

There are a lot of works studying photocatalytic water splitting but the number of reported photocatalysts which are able to decompose water into hydrogen and oxygen efficiently is limited. The efficiency of a photocatalyst is dependent not only on the materials but also on the synthetic method. Similar materials prepared by different methods might give significantly different results. Surface properties, crystallinity and doping or loading of catalytic elements all affect the photoactivity.<sup>81</sup>

TiO<sub>2</sub> is so far widely accepted as a promising photocatalyst. Recently, metal ion and anion doped TiO<sub>2</sub>, especially nitrogen doping, by wet method and solid state method have been successful in extending the absorption edge of TiO<sub>2</sub> towards visible light. However, there may be some disadvantages of these methods, for instance, low surface area, high temperature, glove box or inert gas atmosphere needs to be used for air and moisture sensitive precursors and CO<sub>2</sub> emission during synthesis. Therefore, synthesis of visible light activated TiO<sub>2</sub> by another method that economy and environmentally friendly would be interesting.

This work focuses on utilising a peroxide based route and using TiN as an alternative novel precursor. The peroxide based route without any organic solvent and chloride ion should be useful for synthesis of photocatalysts, while TiN is an air and moisture stable compound that has rarely been used as a precursor for TiO<sub>2</sub> synthesis before.

It is known that aqueous solutions of Ti(IV) and hydrogen peroxide give a peroxytitanato [Ti(OH)<sub>3</sub>O<sub>2</sub>]<sup>-</sup> ion, often called peroxytitanic acid. The mechanism of

the peroxytitanic acid formation from the titanium metal is very complex and not completely understood. However, at pH=11, the reaction can be described by equation 2.1 :



Hydrogen peroxide in excess is necessary to stabilise the solution of peroxytitanic acid. The excess of H<sub>2</sub>O<sub>2</sub> will be decomposed slowly upon ageing with evolution of oxygen gas. When most of the H<sub>2</sub>O<sub>2</sub> is consumed, a yellow gel usually forms spontaneously, even in neutral solution.<sup>82</sup> This method is interesting for titanate compounds synthesis and use for photocatalysts because small particle size, green chemistry (no organic solvent and chloride ion) and ease of controlling the chemical composition would be obtained.

There have been some successes in the synthesis of titanium dioxide by using peroxide based routes with different precursors. Previously, various titanium peroxo complexes with organic ligands could be isolated in solid form but they are often unstable, only few of them were obtained in single-crystal form for which the reliable structural data were reported.<sup>83</sup> Stable solutions at temperatures lower than 5°C can be obtained by dissolution of H<sub>2</sub>TiO<sub>3</sub> in an ice-cooled solvent consisting of H<sub>2</sub>O<sub>2</sub> and ammonia.<sup>84</sup> Titanium peroxo solutions prepared by titanium species such as titanium powder,<sup>63</sup> TiOSO<sub>4</sub>,<sup>85</sup> titanium chloride or titanium alkoxide<sup>86,87</sup> can be used as precursors not only for TiO<sub>2</sub> powder but also for fabrication of TiO<sub>2</sub> films.<sup>88</sup>

The peroxide based route can also be used to produce more complicated titanate compounds. Titanate compounds have attracted attention for their applications in the electronic industry because of its characteristic ferroelectric, piezoelectric and pyroelectric properties. They are normally prepared by a solid state method from metal oxide or metal carbonate. High temperature is needed, low surface area and inhomogeneous porosity are limitations. Lower sintering temperature, higher surface area and homogeneity might be achieved by wet synthesis. BaTi<sub>2</sub>O<sub>5</sub> can be obtained after firing the precipitated powder from the reaction of peroxotitanate with citric acid at 800°C.<sup>89</sup> Similarly, PbTiO<sub>3</sub> is successfully synthesised at reduced temperatures (500 °C) using organic and chloride free peroxo precursor.<sup>90</sup> Chemical composition is easily controlled by the peroxide based route as reported in the strontium titanates family, SrTiO<sub>3</sub>, Sr<sub>2</sub>TiO<sub>4</sub>, Sr<sub>3</sub>Ti<sub>2</sub>O<sub>7</sub> and Sr<sub>4</sub>Ti<sub>3</sub>O<sub>10</sub>.<sup>91</sup> Apart from titanate compounds, the peroxide based route has also been successful in synthesis of high surface area up to 275 m<sup>2</sup>/g nanoparticle Nb<sub>2</sub>O<sub>5</sub> by peptised peroxo niobic acid.<sup>92</sup>

## 2.1 Synthetic procedure

As the aim of this work is to synthesise novel visible light activated photocatalysts, carbon free precursors, TiN, H<sub>2</sub>O<sub>2</sub> and HNO<sub>3</sub>, are chosen in this work. The preparation process is simple and organic free: 1.0 g of TiN (Alfa Aesar), an alternative precursor for TiO<sub>2</sub> preparation, is completely dissolved in 50 ml of 30% hydrogen peroxide under acidic condition adjusted by using HNO<sub>3</sub> acid (pH≤1). After ageing at room temperature without any stirring for 24 hours, a clear red-brown solution is obtained. The obtained precursor solution is stable for several days under ambient atmosphere. The resultant red brown solution is then used as a titanium solution precursor for yellow amorphous and yellow crystalline TiO<sub>2</sub> synthesis. Yellow amorphous precipitate is formed after adjusting the pH of the solution to 2 by slowly adding ammonia solution with constant stirring. The precipitate was filtered and washed with distilled water several times. It was then dried at room temperature. Yellow crystalline powders are obtained after evaporation of the resultant red brown solution at 90 °C and drying at 90 °C or 150 °C. A flowchart of the synthesis is shown in figure 2-1.

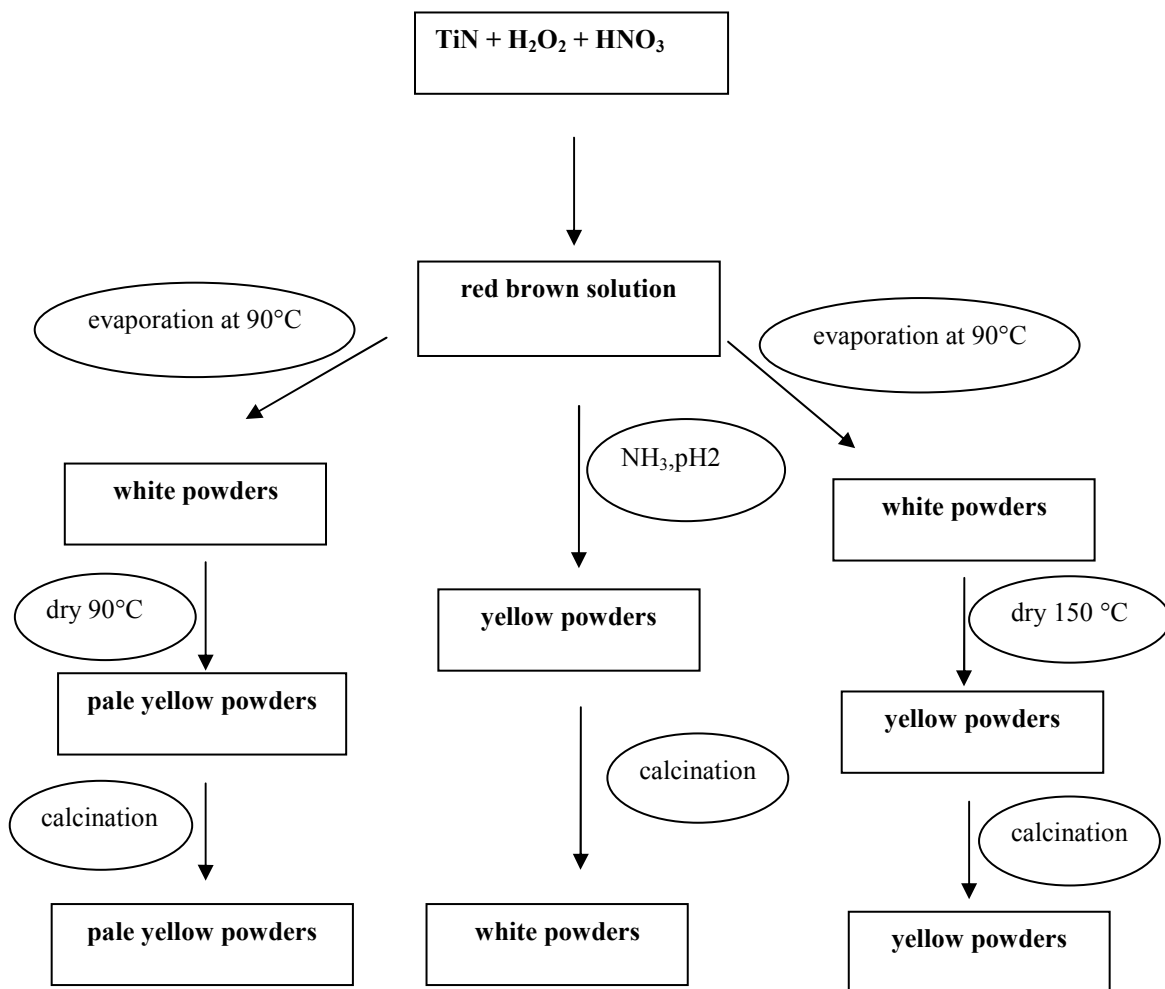


**Figure 2-1 : A flowchart of the materials synthesis**

### 2.1.1 Doping or loading procedure

As some work reports that cation or anion ion doping can accelerate photoactivity,<sup>93,94</sup> some metal ions were doped into yellow crystalline TiO<sub>2</sub> by adding small amount of aqueous metal salt solution into the red brown solution before evaporating and drying. Ce, Ni, Li, Fe, La and Cu doped or loaded yellow TiO<sub>2</sub> were prepared by using nitrate compounds as starting materials whereas ZnSO<sub>4</sub> is used for Zn doping. A solution of Nb metal dissolved in solution of H<sub>2</sub>O<sub>2</sub> and NH<sub>3</sub> was prepared for Nb doping.

### 2.1.2 Pt loading

Platinum loading is frequently reported as a charge separation agent.<sup>50</sup> In this study, the yellow crystalline TiO<sub>2</sub> was loaded with platinum metal by photodeposition method of H<sub>2</sub>PtCl<sub>6</sub>. Yellow TiO<sub>2</sub> powder was added into a stirred aqueous solution of H<sub>2</sub>PtCl<sub>6</sub> and methanol. The suspension was then purged with nitrogen gas and irradiated with UV light for 1 hour, followed by filtering and washing several times with water and drying at 90°C for 1 hour.<sup>50,95</sup>

## 2.2 Characterisation

### 2.2.1 XRD studies

XRD technique is an important method to identify non molecular and crystalline substances. It can be used to determine the crystal structure, unit cell parameters and content, including crystallite size. This structural data is useful in the explanation of trends in many properties.

X- rays are electromagnetic radiation of wavelength around 1 angstrom. Diffraction arises from an interference between in phase adjacent scattering beams (Figure 2-2). When X-rays are scattered by two adjacent parallel planes of atoms or ions in the crystal separated by perpendicular distance or *d-spacing*,  $d$ , the angle of incident at which constructive interference occurs between beams of wavelength,  $\lambda$ , will be related by Bragg's law

$$n\lambda = 2d \sin \theta \quad (2.2)$$

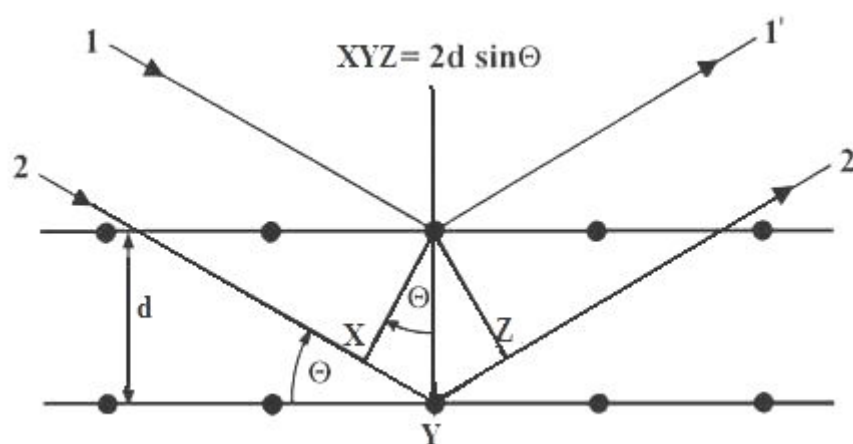


Figure 2-2 : Derivation of Bragg's law

There are 2 types of XRD : powder X-ray diffraction and single crystal X-ray diffraction. Powder X-ray diffraction is used to identify polycrystalline materials, which comprises of thousands of crystallites. Whereas single crystal X-ray diffraction is used for single crystal structure determination.

Since TiO<sub>2</sub> synthesised in this work is in a polycrystalline form, phase identification is carried out by powder X-ray diffraction. The phase contents of the samples can be estimated from the respective XRD peak intensities using the following equation

$$f_A = \frac{1}{1 + \frac{1}{K} \frac{I_R}{I_A}} \quad (2.3)$$

where  $f_A$  is the fraction of anatase phase in the powder, and  $I_A$  and  $I_R$  are the intensities of the anatase (101) and rutile (110) diffraction peaks, respectively.  $K=0.79$  when  $f_A > 0.2$ ,  $=0.68$  when  $f_A \leq 0.2$ .<sup>96,97</sup>  $K$  is a constant in the relation between the weight ratio and intensity ratio for anatase and rutile,  $W_A/W_R = K(I_A/I_R)$ . It is expected that  $K$  is constant over a certain range of concentration.<sup>97</sup>

Apart from phase identification, it can be used to determine approximate crystallite size. The average crystallite size can be estimated from peak broadening by the Debye-Scherrer equation on the anatase (101) and rutile (110) diffraction peaks.

$$D = \frac{K\lambda}{\beta \cos \theta} \quad (2.4)$$

where  $D$  is the average crystallite size in angstroms,  $\lambda$  is the wavelength of the X-ray radiation (Cu K<sub>α</sub>) 0.154056 nm),  $\beta$  is the full width at half-maximum of the highest

intensity peak and  $\theta$  is the radian diffraction angle.  $K$  is a dimensionless constant which is taken as 0.89 here, assuming every point on the lattice emits a spherical wave in a two dimensional lattice.  $K$  may range from 0.89 to 1.39 depending on the specific geometry of the scattering objects.  $K= 0.94$  for a cubic three dimensional crystal and  $K= 1.33$  for perfectly spherical object.<sup>98</sup>

XRD patterns of materials in this work were collected with a STOE STADI P diffractometer operating in transmission mode, which need small amount of sample, and using STOE Win X<sup>POW</sup> software for interpretation.

### 2.2.2 BET measurement

The BET surface area measurement and pore analysis were obtained by nitrogen adsorption with use of Micromeritics ASAP 2020 V3.00 H surface area analyser.

The BET method is widely used for the calculation of surface areas of solids by physical adsorption of gas molecules, assuming there is no interaction between each layer. Prior to determining the surface area, the adsorbed impurities on the surface of samples need to be removed by heating, evacuating and/or flowing gas. Then, the sample is cooled, usually, with liquid nitrogen. After degassing, an adsorptive gas will be introduced into the chamber and the surface area can be analysed by measuring the volume of gas adsorbed at specific pressures.

The BET equation<sup>99</sup> is expressed by :

$$\frac{P}{X(P_0 - P)} = \frac{1}{X_m C} + \frac{C-1}{X_m C} \frac{P}{P_0} \quad (2.5)$$

Where  $P$  and  $P_0$  are the equilibrium and the saturation pressure of adsorptive gas at the temperature of adsorption,  $X$  is the adsorbed gas quantity and  $X_m$  is the monolayer adsorbed gas quantity and  $C$  is the BET constant. Equation 2.5 can be plotted as a straight line and  $X_m$  is calculated from the slope and intercept.

The surface area( $S$ ) is then evaluated by equation 2.6 :

$$S = \frac{X_m N_o A_o}{wM} \quad (2.6)$$

Where  $N_o$  is Avogadro's number,  $A_o$  is adsorption cross section,  $M$  is molar volume of adsorptive gas,  $w$  is mass of adsorbent material.<sup>99</sup>

### 2.2.3 EM studies

In order to examine the morphology and topography of very small specimens, electron optical studies on specimens will give much more information than optical microscopy. Electron microscopy is a powerful tool to study microstructure of nanomaterials. An electron microscope consists of an electron gun, anode, lens, apertures and image recording. The electron, which is commonly produced by heating a tungsten filament, will be attracted by anode and accelerated down the vacuum column and interact with specimens. The electron microscope uses electrostatic and

electromagnetic lenses to control the electron beam and focus it to form an image. Wavelength of the beam might need to be adjusted to close to size of specimens in order to provide more reaction and get more image resolution. As the electron leaves the filament with high potential energy and reaches the anode with high kinetic energy, conservation of energy is applied as following equation

$$eV = \frac{1}{2}mv^2 = \frac{h^2}{2m\lambda^2} \quad (\text{De Broglie equation } p = mv = \frac{h}{\lambda})$$

$$\lambda = \frac{h}{\sqrt{2meV}} \quad (2.7)$$

When  $V$  is very large, relativistic correction is required because velocity,  $v$ , is close to speed of light,  $c$ .

$$\lambda = \frac{h}{\sqrt{2m_0eV_0 \left( 1 + \frac{eV_0}{2m_0c^2} \right)}} \quad (2.8)$$

Where  $m_0$  denotes electron rest mass,  $V_0$  denotes accelerating voltage.

### 2.2.3.1 SEM

Scanning electron microscope can provide information on surface morphology of the specimen. When the electron beam produced from filament, it can be focused by condenser lens to a spot less than 4 nm and a rectangular raster is scanned over the specimen after pass through two sets of scan coils (Figure 2-3). There are several phenomena occur during primary electron bombarding specimen such as emission of

secondary electrons, backscattered electrons, X-rays, photon(light) and absorption of electron by the specimen. The secondary electron detector is generally used for image formation with the scanning electron microscope.<sup>100</sup>

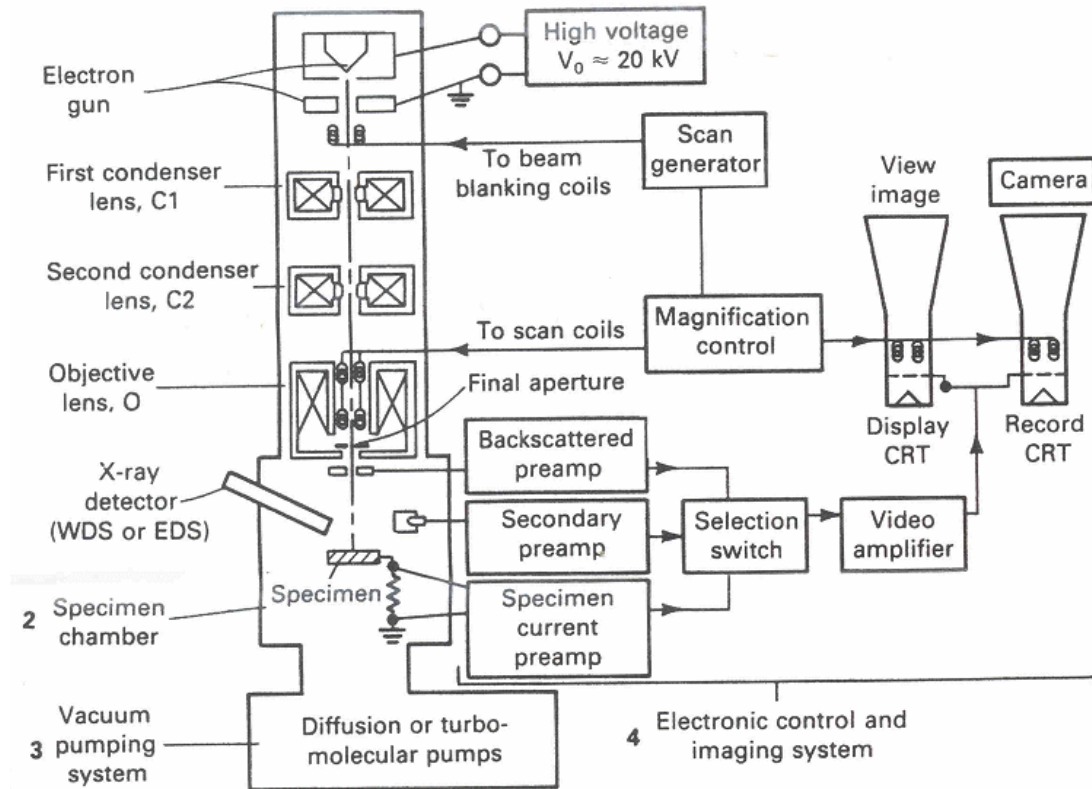


**Figure 2-3 : A schematic diagram of SEM spectroscopy (reproduced from [101])**

SEM images in this work were obtained with a Jeol JSM 5600 SEM, which uses a tungsten filament as electron source and there is a camera for taking digital micrographs of the specimen. The nominal resolution is 3.5 nm, accelerating voltage 0.5 to 30 kV, and magnification is up to 300,000x.

### 2.2.3.2 TEM

Transmission electron microscope (Figure 2-4) is used to study thin specimen as the image is formed when electrons strike the specimen. Phase contrast and diffraction contrast are important factors in image formation of crystalline specimen. The thickness of a specimen should be less than 0.5 micrometers.<sup>102</sup>

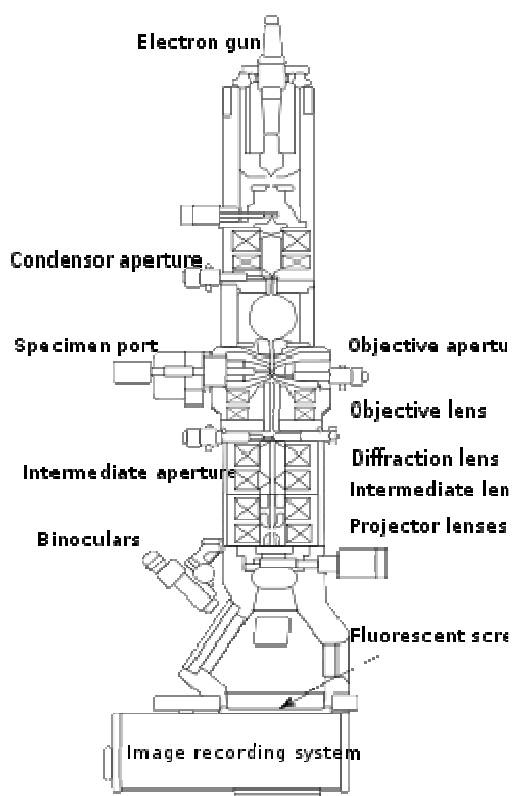


**Figure 2-4 : A schematic diagram of TEM microscope (reproduced from [103])**

Transmission electron microscopy was performed in this work using a Jeol JEM 2011 HRTEM, which uses a LaB<sub>6</sub> filament as the electron source and there is a built in digital camera for taking micrographs of the specimen. The resolution is 0.18 nm, accelerating voltage 80, 100, 120, 160, 200 kV and magnification up to 1,200,000x.

#### 2.2.4 TGA studies

Thermal analysis is a technique that analyses changes in property such as phase transition, melting and decomposition against temperature. Thermal analysis can be divided into several techniques : DTA, DSC and TGA. Differential thermal analysis, DTA, is a technique that compare between temperature of sample and reference during same heating procedure. Differential scanning calorimetry, DSC, is a technique that, when used in correct manner, controls the temperature of sample and reference to be the same by using separate power supplies. The difference of power used in each power supply correlated to endothermic and exothermic reaction of sample. Most modern high temperature DSCs actually use algorithms to convert a temperature lag or lead into a corresponding calorimetry value, so-called power compensated DSC.

In this work, thermogravimetric analysis, TGA, have been used to analyse some properties of the materials. TGA measures a mass change of sample on heating. This technique consists of thermobalance, which can be heat and weigh sample simultaneously. The difference of weight is useful for analysis species occurring during dehydration, desorption and decomposition. It can be also used for studying a reduction-oxidation reaction of the sample, especially transition metals, by controlling atmosphere. Moreover, combination of TGA and mass spectrometer can be used for investigation of evolved species on heating.

TGA data in this work were obtained with a TA Instruments SDT 2960: TGA/DTA under oxidising atmosphere to 1250°C, whereas TG-MS is also be used to confirm the evolved species by using Thermogravimetric Analysis - Netzsch STA 449C with

Mass Spec: TGA/DSC or TGA/DTA under oxidising or reducing atmosphere to 1600°C, coupled to a Pfeiffer mass spectrometer (200amu).<sup>104</sup>

### 2.2.5 FT-IR studies

Fourier transformation infrared spectroscopy is a technique to study vibrational spectrum of a sample when exposed in infrared radiation and recorded variation of the transmission with frequency. The spectrum is extracted by converting information from time domain to frequency domain.<sup>104</sup>

Infrared spectra in this work were obtained with a Perkin Elmer Spectrum GX IR spectrometer.

### 2.2.6 Elemental analysis

Elemental analysis or CHN analysis can be used to identify carbon, hydrogen, nitrogen, oxygen and sulphur content of a sample after decomposition at high temperature. It converts organic compounds to gaseous molecules and a resulting mixture is analysed by passing through a series of thermal conductivity detectors.

Carlo Erba CHNS analyser was used in this work.<sup>104</sup>

### 2.2.7 Magnetic measurement

Superconducting quantum interference device, SQUID, is a technique that can be used to measure very weak magnetic field, based on the quantisation of magnetic flux and current loops in the superconductor. It is a very sensitive magnetometer, sensitive enough to detect magnetic field as low as  $5 \times 10^{-8}$  T.

DC magnetic measurements were performed in a Quantum Design MPMS-XL Superconducting Quantum Interference Device (SQUID) magnetometer. Magnetisation versus temperature behaviours were studied between 5K and 300K, either zero field cooled (ZFC) or field cooled (FC). The ZFC magnetisation was obtained by cooling the sample to 5K in zero field, turning on magnetic field 1 kOe and measuring the magnetisation as the sample warmed up to 300K. The FC magnetisation was subsequently obtained by measuring the magnetisation in the same applied field as the sample cooled to 5K.<sup>105</sup>

### 2.2.8 UV-Visible diffuse reflectance studies

UV-visible diffuse reflectance is an essential tool to investigate a band gap energy. In general electromagnetic radiation can be reflected either in specular mode, an angle of reflectance equal to the angle of incidence, or diffuse mode, scattered in all directions. In this work, an integrating sphere is used in combination with Lambda 35 spectrometer (Figure 2-5). It can collect and measure specular and/or diffuse reflectance. The Lambda 35 is controlled from a Windows® based computer using

UV WinLab™ software. UV-visible diffuse reflectance has been used widely in band gap approximation, surface characterisation and colour measurements.<sup>106</sup>

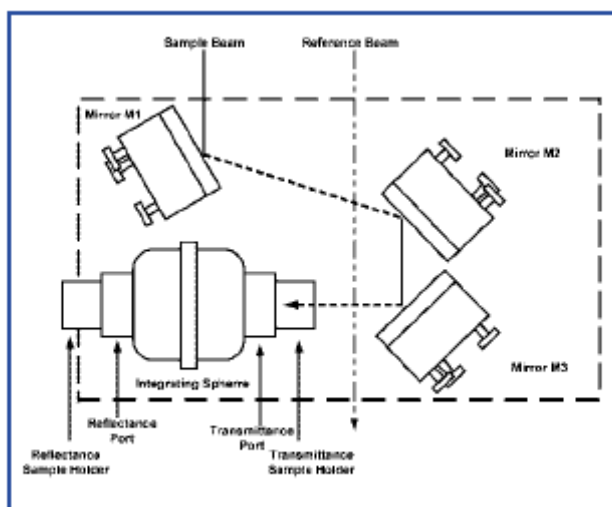


**Figure 2-5 : A schematic diagram of UV-Vis diffuse reflectance spectrometer  
(reproduced from [106])**

### 2.2.9 ESR studies

Electron spin resonance, ESR, or electron paramagnetic resonance, EPR, is a technique used to study compounds possessing unpaired electrons, it can be used for organic compounds and inorganic compounds, especially transition metal compounds. The principle of ESR is analogous to nuclear magnetic resonance, NMR, but monitoring electron spin excitation in magnetic field instead of atomic nuclear spin. Moreover, the spectrum from ESR is illustrated in first derivative peak because a broad signal is normally obtained from ESR, while NMR can use absorption peak directly.

The electron has a spin quantum number,  $s = \frac{1}{2}$  with magnetic moment  $m_s = \pm 1/2$ . It will align itself either parallel ( $m_s = -1/2$ ) or antiparallel ( $m_s = +1/2$ ) on application of an external magnetic field,  $B_0$  and there is a difference in energy,  $\Delta E$ , as shown in figure 2-6.

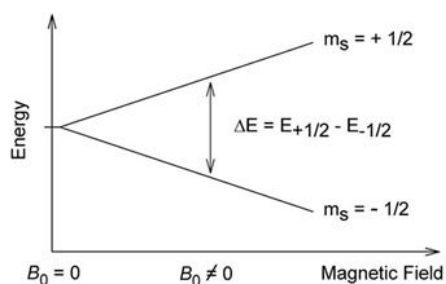


**Figure 2-6 : A magnetic field diagram of ESR**

$$\Delta E = g\mu_B B_0 \text{ or } h\nu = g\mu_B B_0 \quad (2.9)$$

Where  $g$  denotes  $g$ -value and  $\mu_B$  denotes the Bohr magneton

Magnetic field and frequency are the parameters that can be varied until resonance occurs. The conventional ESR instrument generates spectra by irradiating sample with constant microwave frequency around 9 GHz and varying magnetic field.

The  $g$  value of free electron is 2.0023. For electron in transition metal complexes, the  $g$  value might be highly anisotropic and have several values.

As there is also magnetic coupling of electron spin and magnetic nuclei, 2 types of peak structure can be observed : hyperfine structure and fine structure. Hyperfine structure caused by a magnetic coupling of one unpaired electron to adjacent magnetic nuclei and produce  $2I+1$  peaks, where  $I$  denotes nuclei spin. Fine structure caused by

a system that consists of more than one unpaired electron, which produces a more complicated spectrum. ESR can be used to identify a distribution of electron in metal compounds, leading to understanding in oxidation state and structure.<sup>104</sup>

ESR measurements were carried out using a Bruker EMX 10/12 ESR spectrometer at room temperature, 300dT, 9.52GHz, 100kHz, 2.0mW, 1Gpp, 5e4Gain, 20ms, 40ms, 1sc.

#### 2.2.10 XPS studies

X-ray photoelectron spectroscopy, XPS, is a photoionisation based technique. XPS is a surface chemical analysis technique, which can analyse the kinetic energy and number of electrons that escape from the top 1 to 10 nm of the material. Elemental composition, empirical formula, electronic state and oxidation state of the elements can be analysed by the kinetic energy of electron that is emitted from materials during X-ray irradiation.

XPS is based on a single photon in/electron out process (Figure 2-7). The kinetic energy of photoelectron,  $E_K$ , is related to the ionization energy of electron.

When a sample is bombarded with X-ray, electrons will be emitted from core shell.



$$E(S) + h\nu = E(S^+) + E(e') \quad (2.11)$$

As the energy of an electron is a kinetic energy,  $E(e')=E_K$ , it can be rearranged to

$$E_K = h\nu - (E(S^+) - E(S)) \quad (2.12)$$

Since  $(E(S^+) - E(S))$  represents the difference of energy between neutral atom and ionised atom, which is binding energy, so that

$$E_K = h\nu - B.E. \quad (2.13)$$

Binding energy is a characteristic of an element and its oxidation state. Therefore, the presence of peak at each binding energy reveals a specific element and its environment.<sup>107</sup>

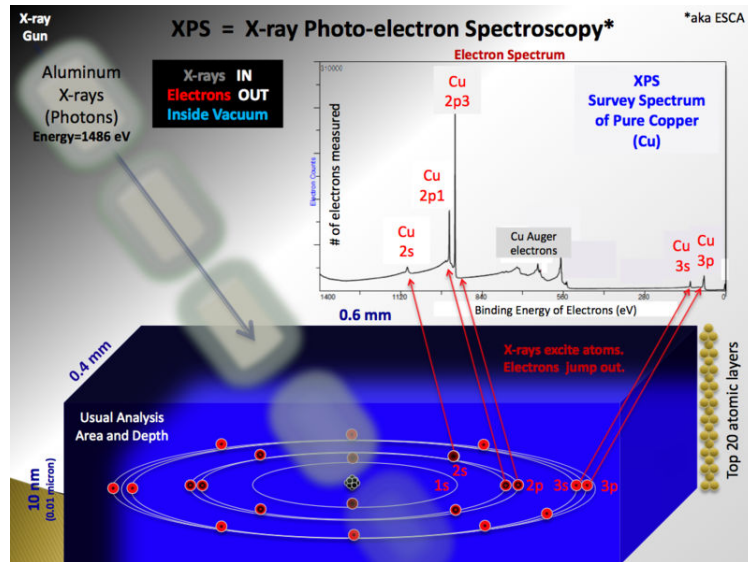


**Figure 2-7 : A schematic diagram of XPS spectroscopy (reproduced from [108])**

The XPS instrument used in this work is a VG ESCALAB2. It operates at a base pressure below  $1 \times 10^{-9}$  mbar. It is equipped with a fast entry lock for sample insertion, Ar ion sputtering and sample heating are also available. The X-ray system is water cooled with Al/Mg anode operated at a voltage of 10kV and an emission current of 40mA, this gives a working power of 400W. The hemispherical electron energy

analyser is equipped with an extraction lens system that defines a minimum spot size for analysis of approx. 3mm diameter. Electron detection is via a single channeltron electron multiplier and the counting electronics and data acquisition are controlled by computer. Sampling is generally performed in 0.1eV steps, a dwell time of 0.5 seconds and a pass energy of 20 eV. In all cases 10 scans are combined to produce the final spectrum. The spectra were analysed using the CASAXPS software. Peaks were generally fitted using a Guassian-Lorentzian peak shape with a Shirley type background.

### **2.3 Photocatalytic evaluation**

Visible light photoactivity of the samples is evaluated by photooxidation of methylene blue and photoreduction of hydrogen from water splitting.

#### **2.3.1 Photooxidation of methylene blue**

Visible light activity is typically evaluated on the basis of the decomposition of methylene blue (MB) in an aqueous solution. The sample powder was suspended in 200mL of  $1 \times 10^{-4}$ M MB solution by air bubbling. This mixture is first suspended in the dark for 30 minutes to reach the adsorption equilibrium before irradiation with a high intensity discharge 250 W iron doped metal halide UV bulb (UV Light Technology Ltd., Birmingham, UK) equipped with UV cutoff filter,  $\lambda \geq 420$ nm (Borosilicate Coated GlassHM07, UQG(optic) Ltd., Cambridge UK). The mixture temperature is controlled at about 25°C using a water bath for infrared radiation and

lamp heating removal. After irradiation, 2 mL of the mixture was collected and centrifuged at the irradiation time intervals (hourly). The photoactivity is examined by monitoring the reduction of the absorbance at 665 nm. The spectrophotometric measurements are carried out using a Perkin Elmer Lambda35 UV/Vis spectrometer. A ten-fold dilution is used for the high absorbance solutions.

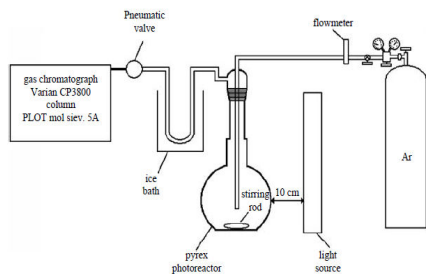
### 2.3.2 Photocatalytic water splitting

As hydrogen gas and some other gases will be evolved as products by the photocatalytic water splitting, a gas tight vessel with valves for controlling gas purging and gas sampling is required. Several types of photocatalytic water splitting reactors have been used previously, for example, lamp located on the side of glass photoreactor,<sup>112</sup> lamp located on the top of glass photoreactor,<sup>113</sup> lamp located on the side of PTFE photoreactor<sup>114</sup> (Figure 2-8). A small glass vessel is generally used as a reactor with light just passes through once without reflecting back to activate this photocatalyst again. This work focuses on a practical application, so that a big box is preferred as it might better reflect to a practical application. The box used in this work is made of aluminium metal as a frame with PTFE, polytetrafluoroethylene, liner inside. Suspension of photocatalysts and aqueous solution is just in the PTFE liner with a glass window on top, avoiding contact to aluminium as shown in figure 2-9. Aluminium was chosen as a light reflector to increase the chance of photocatalyst to absorb light as many times as possible. PTFE was chosen for the liner of the box because it can be used with most chemicals without corrosion, even with very aggressive reagents like concentrated sulfuric acid at elevated temperatures. There are several studies using it as a photoreactor due to its good transparency to UV light in

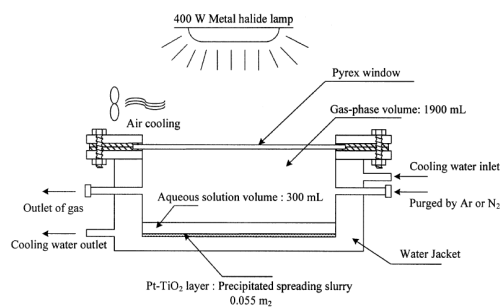
the range of 230-400 nm.<sup>109,110</sup> Whereas, glass, plastic and stainless steel may not resist some solvents, acids and bases. Quartz is widely used as a photoreactor but it has some disadvantages such as expensive, fragile.

The photocatalytic water splitting in this work was evaluated by suspending and stirring 0.1 g of TiO<sub>2</sub> in 200 mL of pure deionised water, or methanol solution or oxalic solution in case of sacrificial agent investigation. The photoactivity was determined in anaerobic atmosphere (nitrogen) also in aerobic atmosphere (air) for comparison. When considering a practical application, it would be interesting if hydrogen can be produced under air atmosphere. Usually, photoactivity will be achieved under inert atmosphere, just a few reports of good results exist under aerobic condition.<sup>111</sup> The solution was purged with nitrogen gas for 30 minutes, if needed, and then the suspension was illuminated from above with the high intensity discharge 250W iron doped metal halide UV bulb equipped with UV cut-off filter,  $\lambda \geq 420\text{nm}$ . The evolved gases were monitored by gas chromatography. Temperature of the box is around 50°C owing to heat of the lamp. There is no a cooling system attached to the box because it was found that photoactivity of hydrogen production also depends on temperature. An optimal temperature is around 60-80°C, which relates to the adsorption/desorption equilibria at the active sites of TiO<sub>2</sub> and diffusion rates to and from the surface.<sup>73</sup> Keeping temperature around 50°C might be consistent to the practical application using sunlight.

A



B



C

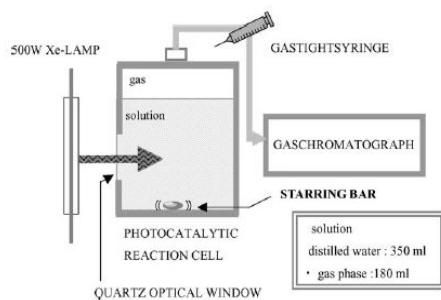


**Figure 2-8 : Illustration of some types of photoreactor, A : Lamp located on the side glass photoreactor ( reproduced from [112]), B : lamp located on the top glass photoreactor (reproduced from [113]), C : lamp located on the side PTFE photoreactor (reproduced from [114])**

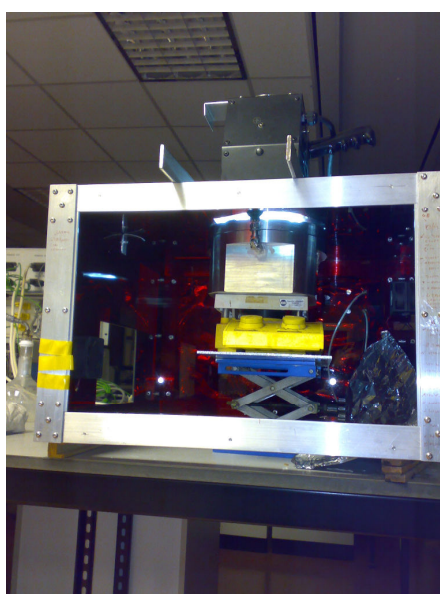
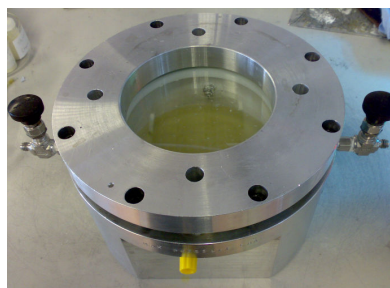


**Figure 2-9 : Illustration of the box and experimental set up in this work**

The metal halide bulb used in this work contains mercury vapour and some metal halide. Therefore, the main emission wavelengths are similar to mercury lamp. Extra wavelengths from iron doping provides a continuum wavelength of iron doped metal halide as shown in figure 2-10.

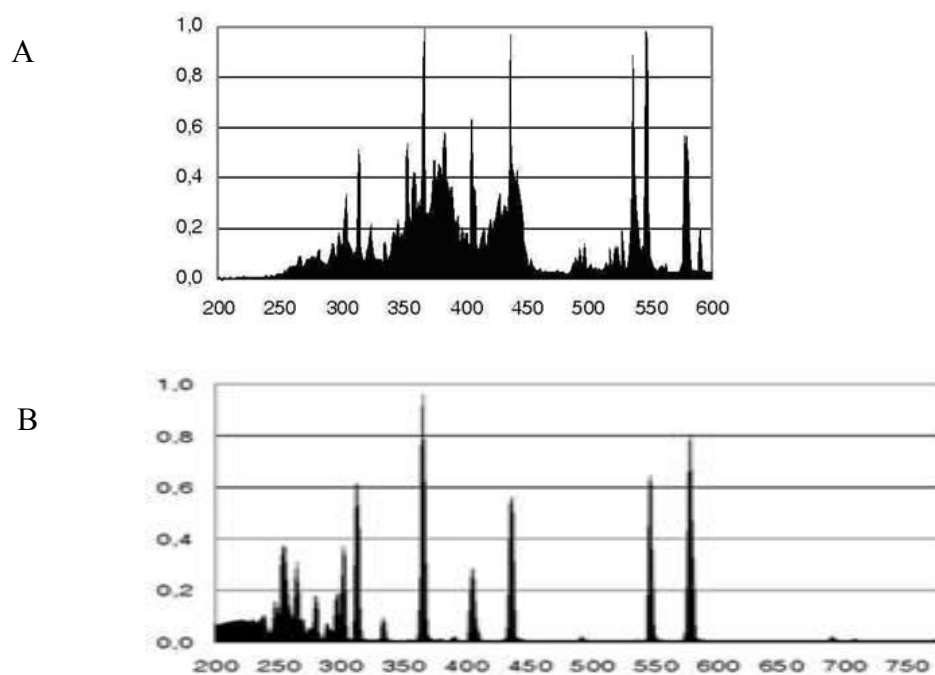


**Figure 2-10 : The emission wavelength of (A) Iron doped metal halide lamp, (B) Mercury lamp(reproduced from [115])**

Transmission spectrum of UV cut-off filter and glass window illustrated in figure 2-11 confirmed visible light photoactivity measurement. UVA can also be measured by changing filter to black filter, which has a transmission range around 315-405 nm.

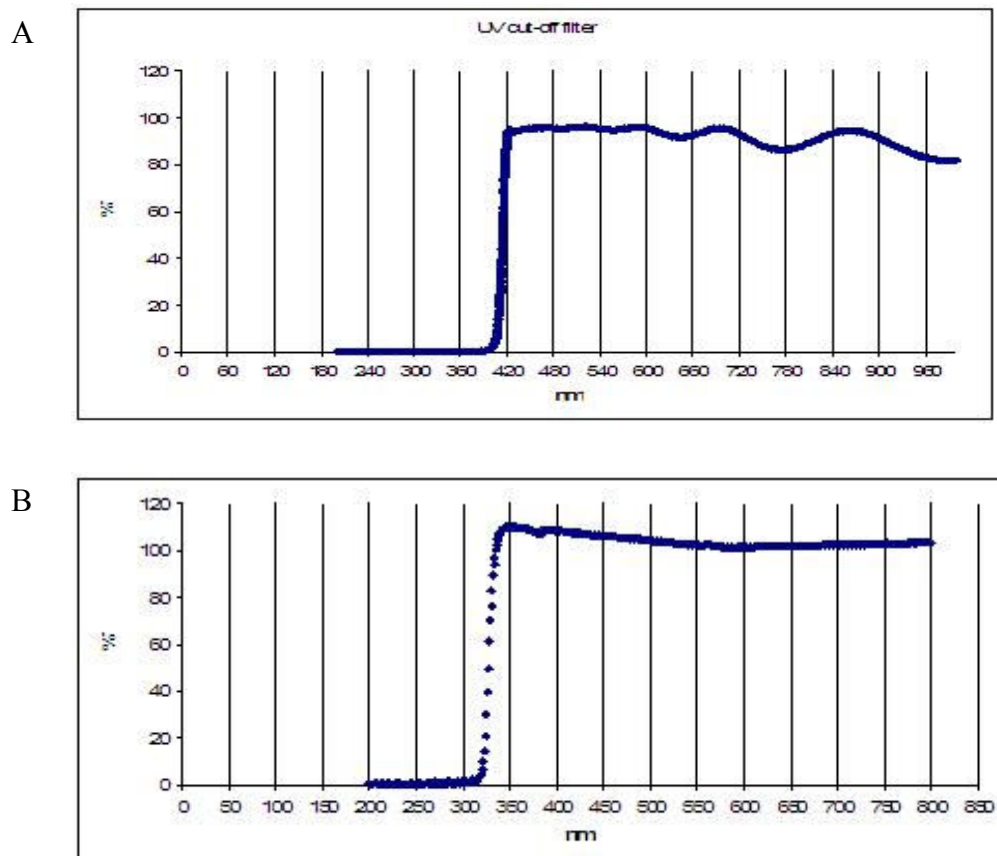


**Figure 2-11 Transmission spectra of (A) UV cut-off filter, (B) glass window.**

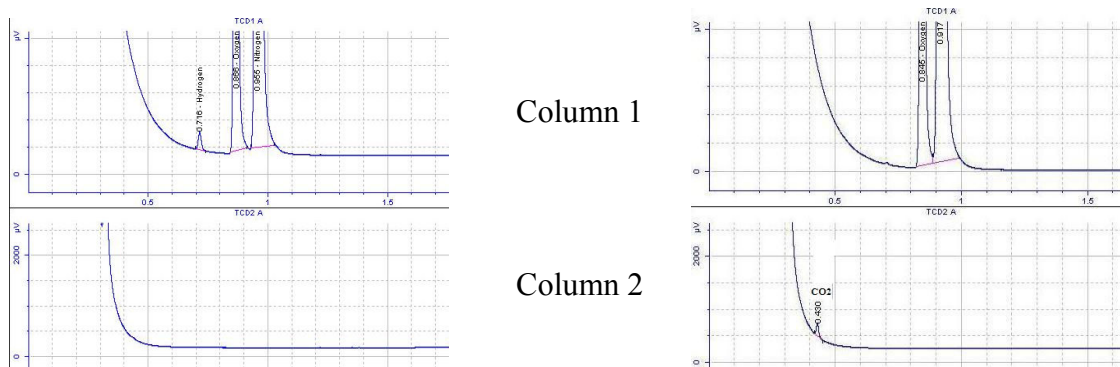
### 2.3.2.1 Gas chromatography

Gas chromatography is one of the most widely used analytical techniques. It is used to separate mixture components by the relative attraction of each component to a stationary phase while a gas mobile phase passes through the stationary phase. The sample used in a gas chromatography need to be a gas or can be converted to a gas phase at the temperature of the column. It can be used for both qualitative and quantitative analysis. Retention time of each species, which is the time required to elute the species from the stationary phase, is used to identify the mixture components.

Gas chromatography instrument used in this work is Agilent 3000 Micro GC<sup>105</sup>. It consists of a heated injector, sample column, reference column, thermal conductivity detector (TCD), electronic pressure control (EPC) hardware, gas flow solenoids, and control board.

- Sample injection : Back flush type, 1  $\mu\text{L}$  injection volume, internal sample vacuum pump, sample inlet temperature 130  $^{\circ}\text{C}$ , injector temperature 90  $^{\circ}\text{C}$ , back flush time 9 s, run time 120 s.
- Column 1 :  $\text{H}_2$ ,  $\text{O}_2$ ,  $\text{N}_2$  were analysed by using Molecular sieve 5A PLOT column, column temperature 75  $^{\circ}\text{C}$ , Ar carrier gas.
- Column 2 :  $\text{CO}_2$  was analysed by using PLOT U column, column temperature 120  $^{\circ}\text{C}$ , Ar carrier gas.

Thermograms showing  $\text{H}_2$ ,  $\text{O}_2$ ,  $\text{N}_2$  and  $\text{CO}_2$  peaks obtained from some experiments in this work are shown below



- Detector : Thermal conductivity detector using Wheatstone Bridge design.

## 2.4 Actinometry

In order to calculate efficiency, absorbed photon flux of the system needs to be measured. A chemical actinometer was used to calculate photon flux in this work. Ferrioxalate actinometer or iron(III) potassium oxalate trihydrate [potassium tris(oxalato) ferrate(III) trihydrate],  $K_3[Fe(C_2O_4)_3] \cdot 3H_2O$ , photoreduction (Hatchard–Parker actinometer) have been chosen. The difference between absorbance of 0.006 M  $K_3[Fe(C_2O_4)_3] \cdot 3H_2O$  solution in the dark and under irradiation is used for calculation.

A 0.006 M  $K_3[Fe(C_2O_4)_3] \cdot 3H_2O$  solution is prepared and 3 cm<sup>3</sup> ( $V_1$ ) of the solution are irradiated under efficient stirring. 1 cm<sup>3</sup> ( $V_2$ ) of the irradiated solution is added into a 10 cm<sup>3</sup> ( $V_3$ ) volumetric flask containing a mixture of 4 cm<sup>3</sup> 0.1 % 1.10-phenanthroline solution and 0.5 cm<sup>3</sup> buffer solution from stock (buffer stock solution is prepared by dissolving 82 g  $NaC_2H_5CO_2$  in 10 cm<sup>3</sup> conc.  $H_2SO_4$  and dilution to 1 dm<sup>3</sup> with distilled water). Distilled water is added to the flask to the 10cm<sup>3</sup> mark.

A reference 0.006 M  $K_3[Fe(C_2O_4)_3] \cdot 3H_2O$  solution in the dark condition is prepared in the same way without irradiation. The absorbance difference between the two samples is measured at 510 nm after being kept for 1 hour (optical pathlength,  $l$ , = 1 cm,  $\epsilon(510 \text{ nm}) = 11,100 \text{ dm}^3 \text{ mol}^{-1} \text{ cm}^{-1}$ ).

The photon flux,  $q_{n,p}/\text{einstein s}^{-1}$ , can be calculated by following equation :

$$q_{n,p} = \frac{\Delta A \cdot V_1 \cdot V_3}{\phi(\lambda) \cdot \epsilon(510nm) \cdot V_2 \cdot l \cdot t} \quad (2.14)$$

where  $t$  = irradiation time and  $\Phi(\lambda) = 1.11$  at 436 nm.<sup>116</sup>

However, the ferrioxalate actinometer just absorb wavelength range 250-500 nm, it might not reflect the whole emitting wavelength of the lamp.

## CHAPTER 3

### Characterisation of novel coloured oxides

Dissolution of titanium nitride in hydrogen peroxide solution gives a yellow colour under basic conditions and red brown colour under acidic conditions. The colour of solution from reaction between titanium solution and hydrogen peroxide is used for colourimetric quantitative determination of amount of titanium ion or concentration of hydrogen peroxide as it follows Beer's law.<sup>117,118</sup>

The yellow solution obtained by dissolution of titanium nitride with hydrogen peroxide and ammonia at pH10 is not stable, it will precipitate a yellow powder when hydrogen peroxide is completely consumed or decomposed with ageing, normally after leaving overnight after dissolution.

The resultant red brown solution at pH2 is stable for several days or several weeks under aerobic condition at ambient temperature. Two yellow powders with different properties can be prepared from this solution by filtration and evaporation.

- Yellow amorphous powder was formed after adjusting the pH of the solution to 2 by slowly adding ammonia solution, then filtering and drying at room temperature.
- Yellow crystalline powders were obtained after evaporation of the resultant red brown solution at 90 °C and drying around 90-150 °C.

### 3.1 Characterisation of yellow amorphous TiO<sub>2</sub>

Coloured amorphous titanium dioxide powders or titanium peroxo compounds were prepared by filtration after adjusting the pH of the red brown obtained from dissolution of titanium nitride at  $\text{pH} \leq 1$  with ammonia solution to pH2 and pH10. An intensely coloured yellow powder was obtained at pH2 and a green-yellow powder was obtained at pH10. In general, coloured titanium peroxo powders are not quite stable, it will turn to white with ageing, which corresponds to colour of powder formed at pH10 that gradually turn into white with ageing as well as the yellow powder formed at pH2 using titanium powder as precursor. It is interesting that intense yellow powder obtained at pH2 and using titanium nitride as precursor is more stable and can be kept in a clear vial at ambient atmosphere for several months. Since the yellow powder formed at pH2, thereafter called “Yamor-pH2”, is more stable than pH10, Yamor-pH10, photoactivity will focus on Yamor-pH2.

### 3.1.1 TEM and BET surface area

The ultrafine particles with amorphous structure can be seen from TEM image in figure 3-1. As a result, a high BET surface area of 261 m<sup>2</sup>/g was obtained.

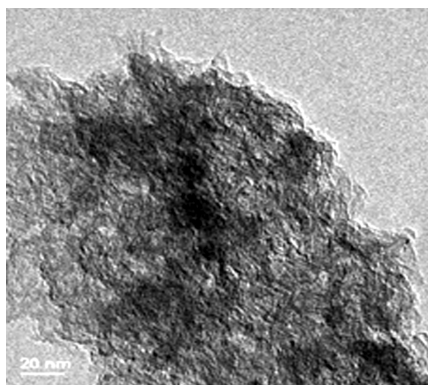


**Figure 3-1 : TEM image of yellow amorphous TiO<sub>2</sub> prepared at pH2.**

### 3.1.2 XRD

The XRD pattern of the as-prepared powder confirmed the amorphous structure of Yamor-pH2 as no diffraction peaks can be observed as shown in Figure 3-2. Yamor-pH2 is quite stable under air atmosphere (the sample used throughout this work was kept for several months in the aerobic vial). However, colour and phase transformation of yellow amorphous to white anatase/rutile occurred on heat treatment.

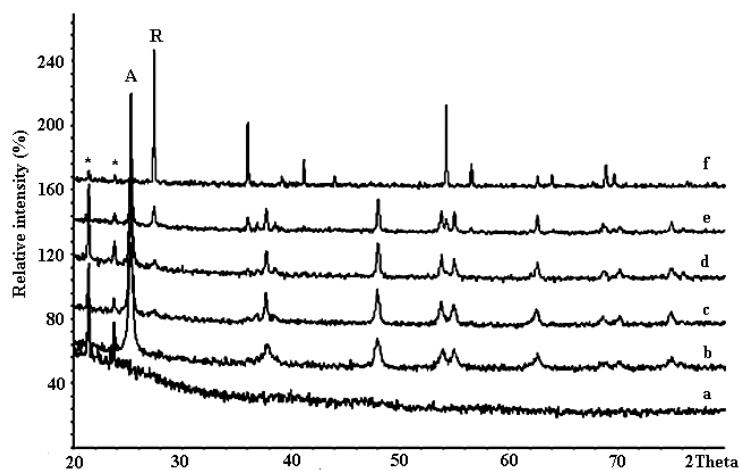


**Figure 3-2 : XRD patterns of as-prepared Yamor-pH2 (a) and after calcining at temperatures of (b) 400°C, (c) 800°C, (d) 850°C, (e) 900°C, (f) 1,100°C**

**(\*: Vaseline specific peaks, A: anatase, R: rutile).**

Anatase is presented after calcination at 400°C and remained as a major phase until 900°C. This indicated that a high temperature stable anatase phase can be produced by this method. Phase transformation from anatase to rutile can be observed at about 800–850°C which was higher than TiO<sub>2</sub> prepared by conventional methods. Furthermore, it was found that the crystallite sizes of TiO<sub>2</sub> after calcination at 600°C and 900°C calculated by Scherrer equation are 31 and 51 nm, respectively. The obtained phase transformation temperature and particle size were consistent with the previous work that synthesised TiO<sub>2</sub> by peroxide-based route and using H<sub>2</sub>TiO<sub>3</sub> as precursor. However, the stability of anatase phase in this work was higher than TiO<sub>2</sub> synthesised by the peroxide-based route using TiCl<sub>3</sub> as precursor. The peroxide-based route, therefore, is interesting for TiO<sub>2</sub> preparation because of the high temperature anatase-rutile phase transformation, it depends on precursor and synthesis condition though. TiN is interesting to be used as an alternative precursor in a peroxide-based route because of its air and moisture stability, organic and chloride ion-free route, simplicity, and low cost.

### 3.1.3 TGA

Thermogram and its differential plot of Yamor-pH2 and Yamor-pH10 were shown in figure 3-3. The presence of adsorbed water on the surface might be observed from weight loss upon heating until 100°C. A gradual decrease extending from 100-300°C was observed due to a decomposition of water and hydroxyl group. However, weight loss of Yamor-pH2 still gradually decreased from 400-550°C, which is different from 15% weight loss step around 400°C of Yamor-pH10. Bonded peroxy species may possibly decompose at 400-600°C and oxygen is released (endothermic effect).<sup>91,89</sup> It might be concluded that bonding of peroxy species in Yamor-pH2 is different from Yamor-pH10, as there is no drastic weight loss at 400°C and can be seen clearly from the differential plot (figure 3-3b). There is no weight loss beyond 550°C for both histories.

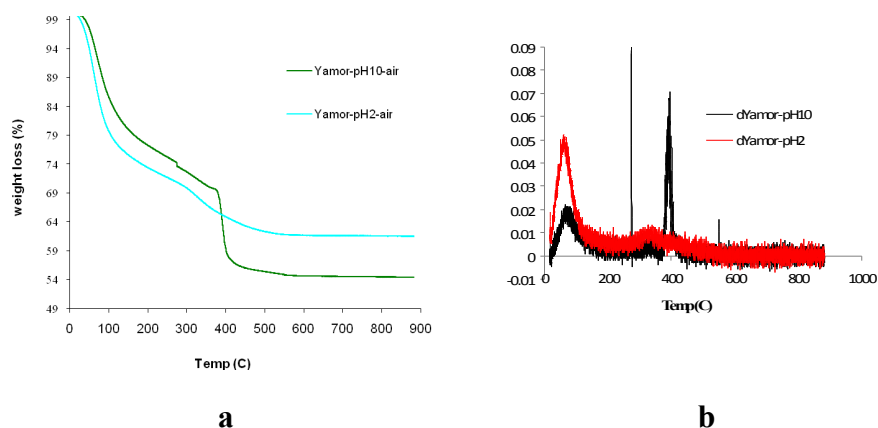


**Figure 3-3 : Thermogram (a) and differential plot (b) of Yamor-pH2 (7.222mg) and Yamor-pH10 (15.515mg) from room temperature to 900°C under air atmosphere with heating rate 5°C/min.**

TG-MS in argon was used to clarify decomposed species during increasing temperature of Yamor-pH2. TGA and DSC thermograms under argon atmosphere can be seen in figure 3-4. Weight loss up to 300°C is possibly due to adsorbed water as peaks of mass number 17 and 18 of H<sub>2</sub>O parent molecule were detected by mass spectrometer. There may be some O<sub>2</sub><sup>2-</sup> decomposed as well since mass number 32 was observed as shown in figure 3-5a, 3-5b. However, it is clearly shown that O<sub>2</sub><sup>2-</sup> is the main species that loss during 300-500°C .

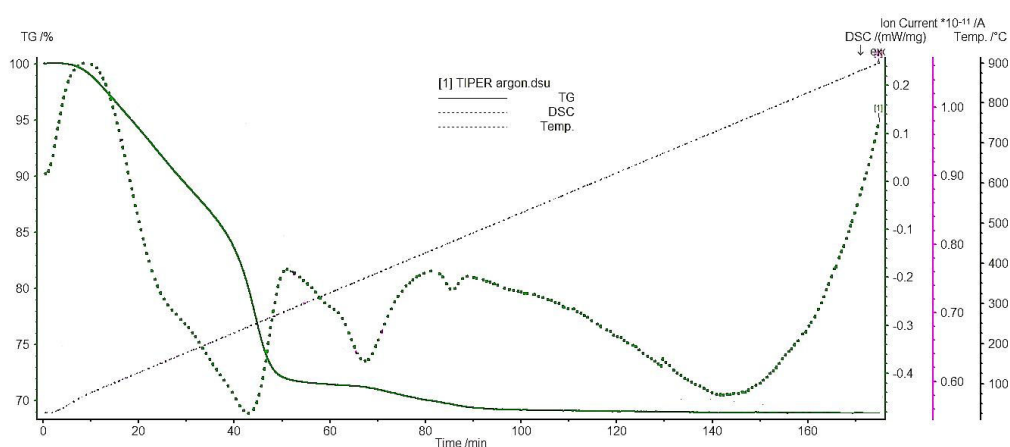


**Figure 3-4 : Thermogram of Yamor-pH2 under argon atmosphere with heating rate 5°C/min.**

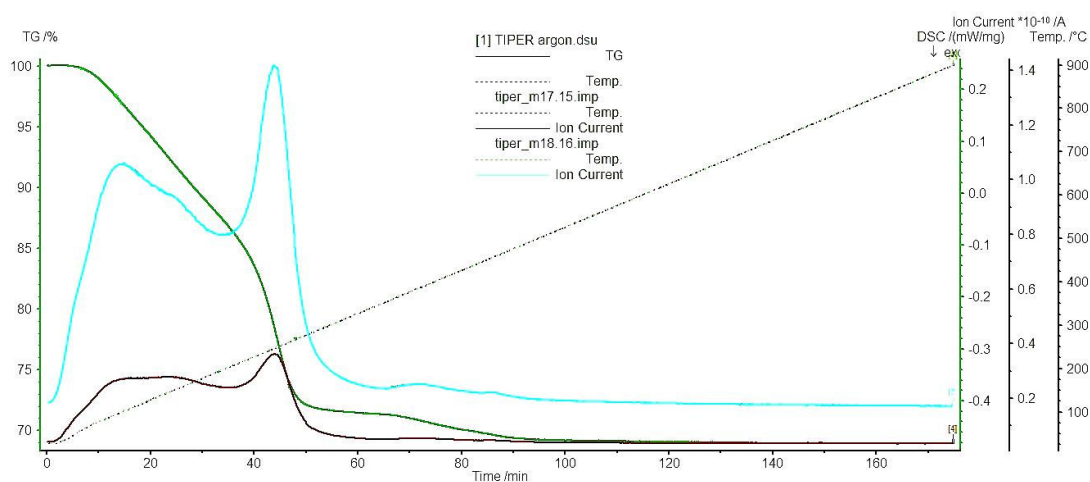


**Figure 3-5a : Thermogram of Yamor-pH2 and mass number 17 and 18 spectra.**

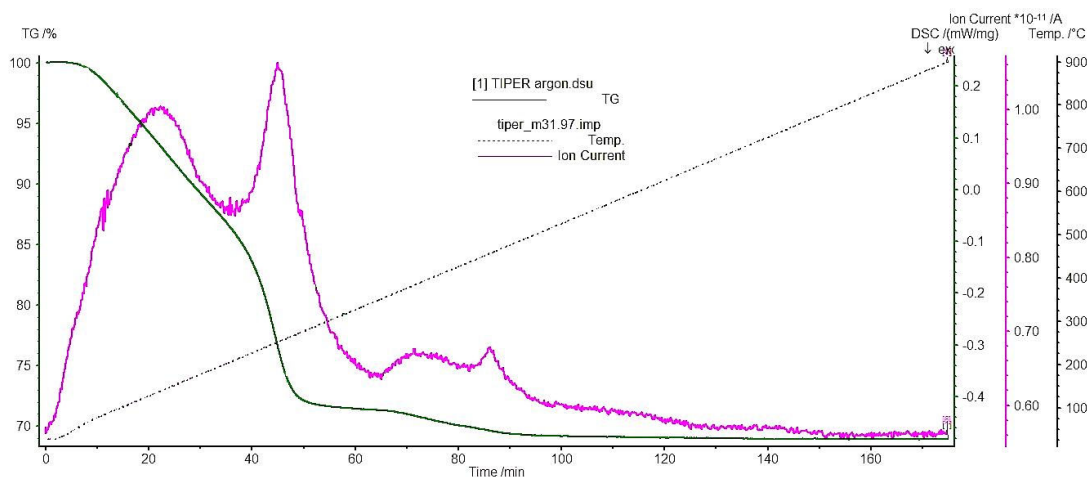


**Figure 3-5b : Thermogram of Yamor-pH2 and mass number 32 spectrum.**

### 3.1.4 FT-IR

FT-IR spectrum confirmed the titanium peroxy species as there is a band around 900  $\text{cm}^{-1}$  of O-O stretching vibration character of peroxy group.<sup>84,119,120</sup>

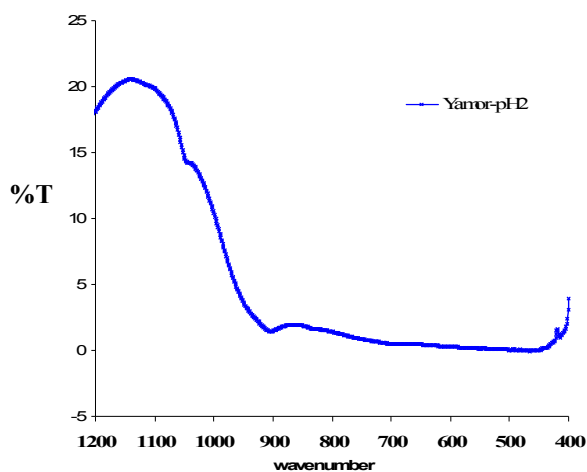


**Figure 3-6 : Infrared spectrum of Yamor-pH2.**

### 3.1.5 UV- Visible diffuse reflectance

Band gap energy can be estimated by a band edge position of UV-Vis diffuse reflectance spectrum. Amorphous normally has a wider band gap energy than crystalline powder.<sup>73</sup> Particle size and phase also affect to the band gap energy. Smaller particle size yielding higher band gap energy is a quantum size effect.<sup>17</sup> Comparison between Yamor-pH2 and white rutile phase TiO<sub>2</sub> was shown in figure 3-7, it was found that Yamor-pH2 shows the red shift of the absorption edge into the visible region. Ymor-pH10 has a red shift of adsorption edge into visible light region in parallel with Yamor-pH2 as shown in figure 3-8.

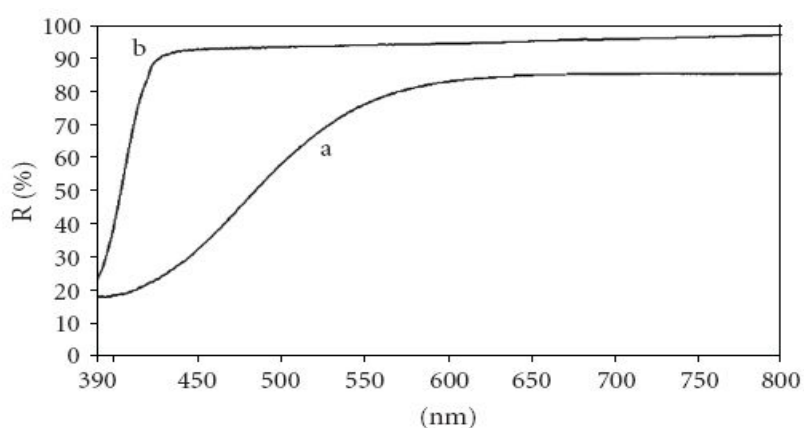


**Figure 3-7 : The UV-Vis diffuse reflectance of (a) Yamor-pH2, (b) commercial rutile TiO<sub>2</sub>.**

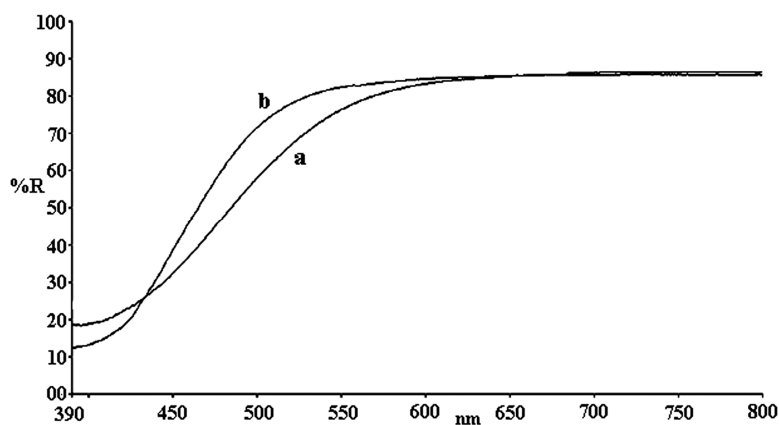


**Figure 3-8 : The UV-Vis diffuse reflectance of (a) Yamor-pH2, (b) Yamor-pH10.**

### 3.1.6 XPS

Ti and O XPS data show the presence of small peaks of Ti species other than  $\text{Ti}^{4+}$ , possibly  $\text{Ti}^{3+}$  on the amorphous surface. Broadening of the O XPS signal was observed with an additional set of O peaks at lower binding energy indicating that different environment of oxygen are present. Two O1s peaks were normally detected from XPS, which is a small peak of oxygen from surface hydroxyl groups at higher binding energy and main peak of lattice oxygen in  $\text{TiO}_2$  at lower binding energy. There may be one more peak at higher binding energy than surface oxygen of O-C as shown in  $\text{TiO}_2$  spectrum in figure 3-10, possibly owing to using graphite as an internal standard during operation. However, O1s peak at lower binding energy than lattice of oxygen can be observed in case of Yamor-pH2, which might be an oxygen from peroxo group.<sup>121,122</sup>

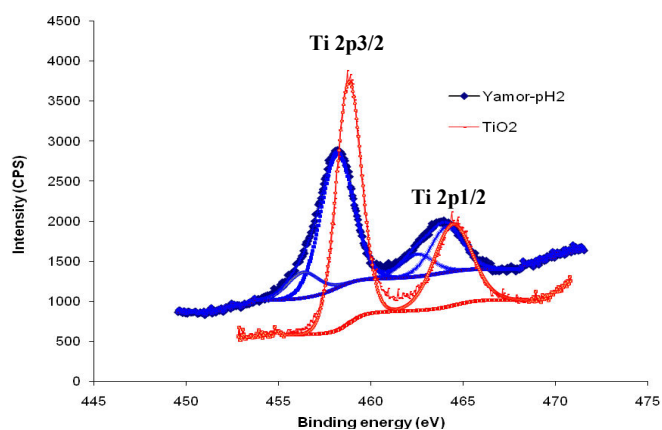


**Figure 3-9 : XPS spectra of titanium species comparing between Yamor-pH2 and  $\text{TiO}_2$ .**

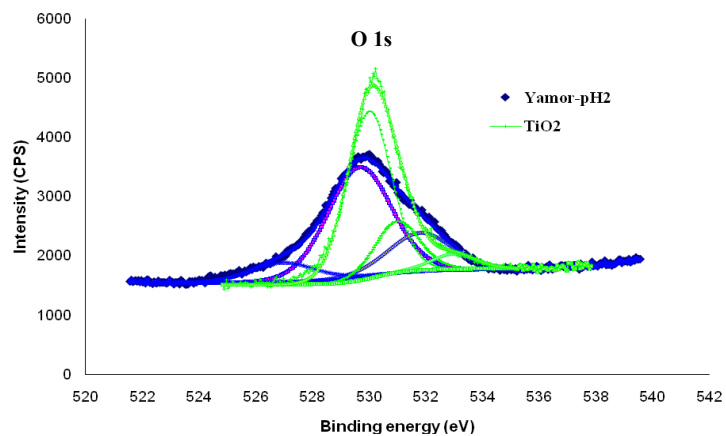


**Figure 3-10 : XPS spectra of oxygen species comparing between Yamor-pH2 and rutile  
TiO<sub>2</sub>.**

## Summary

According to our focus on evaluation of the visible light photoactivity of yellow amorphous TiO<sub>2</sub>, TEM, BET, XPS, FT-IR and UV-Vis diffuse reflectance were only examined with the as-prepared powder. Yamor-pH2 is attributed to the  $\eta^2$ -peroxide ( $\eta^2$ -TiOOH) because of transformation of Yamor-pH2 to white powder on heating similar to the  $\eta^2$ -titanium peroxy species in the TS-1/H<sub>2</sub>O<sub>2</sub>/H<sub>2</sub>O system reported by Bonino et al.<sup>123</sup> Moreover,  $\eta^2$ -peroxide was assigned to the adsorption structure formed by the addition of H<sub>2</sub>O<sub>2</sub> on the surface of rutile TiO<sub>2</sub><sup>124</sup> and found that the  $\eta^2$ -peroxide species obtained upon loading H<sub>2</sub>O<sub>2</sub> into TS-1 was photodissociated efficiently under irradiation with visible.<sup>125</sup> This peroxy species can be restored when further addition of H<sub>2</sub>O<sub>2</sub> indicating the interaction with H<sub>2</sub>O<sub>2</sub> and does not cause any evident extensive damage to the Ti(IV) structure.

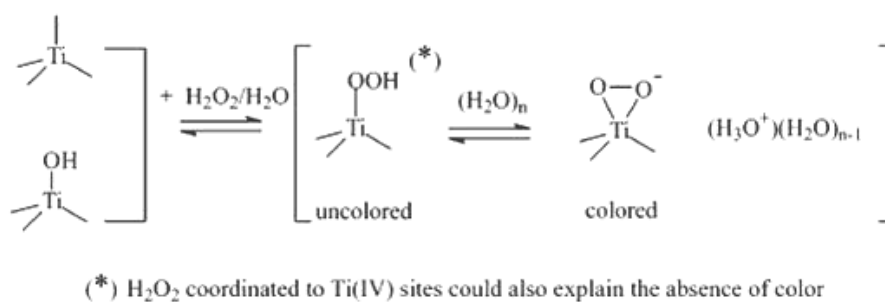


**Figure 3-11 Proposed mechanism of interaction between H<sub>2</sub>O<sub>2</sub>, H<sub>2</sub>O and Ti by Bonino et al. (reproduced from[123]).**

## 3.2 Characterisation of yellow crystalline TiO<sub>2</sub>

Yellow crystalline powders were obtained by evaporation and drying of the resultant red brown solution of dissolution of TiN in hydrogen peroxide and nitric acid. Powders after evaporating at 90 °C were dried at two temperatures, around 90 °C and 150 °C. Pale yellow powders were obtained at 90°C drying while 150 °C drying produced yellow powders.

### 3.2.1 XRD

The XRD pattern of the as-prepared yellow powder after drying at around 150 °C shows mainly amorphous phase with broad peaks of rutile phase character (Figure 3-12a). The intensity of yellow colour and crystallinity of rutile phase increase with increasing heating temperature treatment. No anatase phase can be observed (Figure 3-12b,c,d,e). It can be concluded that a rutile phase TiO<sub>2</sub> without any anatase phase can be prepared even with only a low temperature treatment by this method, in spite of the anatase to rutile phase transformation temperature prepared by conventional method being around 600-700 °C.

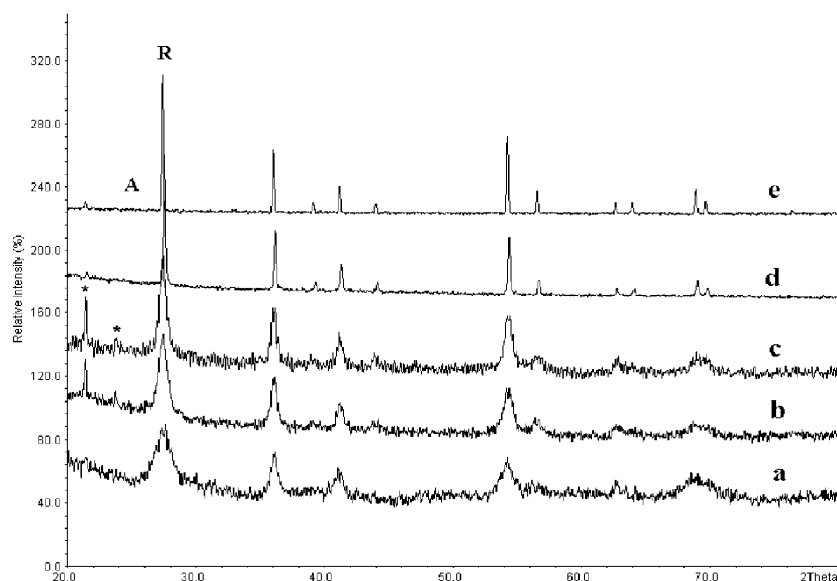


**Figure 3-12 : XRD patterns of powders prepared from acidic condition, as prepared (a) and after calcination at temperatures of (b)400 (c)600 (d)900 (e)1,200 °C (\* : peaks from sample mounting, A : anatase, R : rutile).**

An acid catalysed reaction is thought to favour the rutile phase because a yellow as prepared powder with broad peak of anatase character that transforms to anatase-rutile mixture phase TiO<sub>2</sub> after calcination at 600 °C was prepared by this method under basic condition, consistent to previous work that synthesised mixed anatase and rutile at low temperature by controlling acidity.<sup>126</sup> The reaction mechanism is thought to involve an acid catalysed combustion reaction between titanium peroxy species and NH<sub>4</sub>NO<sub>3</sub> because the NH<sub>4</sub>NO<sub>3</sub> phase was found in the XRD pattern of as prepared powder before drying at 150 °C as shown in figure3-13a. Nakajima and Kudo reported that nitrogen species of tungsten nitride after dissolution with H<sub>2</sub>O<sub>2</sub> were transformed to NH<sub>4</sub><sup>+</sup>~80% , NO<sub>3</sub><sup>-</sup> ~2% and N<sub>2</sub> ~20%, perhaps corresponding to an appearance of NH<sub>4</sub>NO<sub>3</sub> in this method. To investigate this proposal, we have compared samples obtained by drying at 90 °C and 150 °C after evaporating and samples obtained by filtering and washing the evaporated powder before drying.

Amorphous samples without  $\text{NH}_4\text{NO}_3$  were obtained after filtering and washing the evaporated powder (Figure 3-13d), which is transformed to white powder of anatase phase  $\text{TiO}_2$  after calcination at  $600\text{ }^\circ\text{C}$  (Figure 3-13e). Whereas, pale yellow anatase-rutile mixture phase (Figure 3-13b) and intense yellow rutile phase (Figure 3-13c) were obtained for the samples prepared by drying the evaporated powder at  $90\text{ }^\circ\text{C}$  and  $150\text{ }^\circ\text{C}$ , respectively. Thus,  $\text{NH}_4\text{NO}_3$  and drying temperature influence the properties of product. It can be concluded that yellow  $\text{TiO}_2$  can be synthesised by the acid catalysed combustion reaction of titanium peroxy species and  $\text{NH}_4\text{NO}_3$ . Rutile phase tends to be formed at higher acidity and higher drying or ignition temperature, which correspond to the conventional combustion method. Properties of products depend on the ignition temperature.

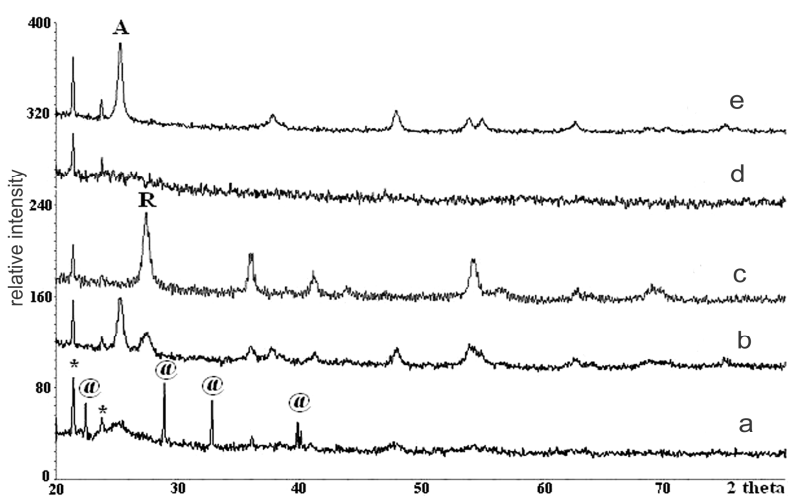
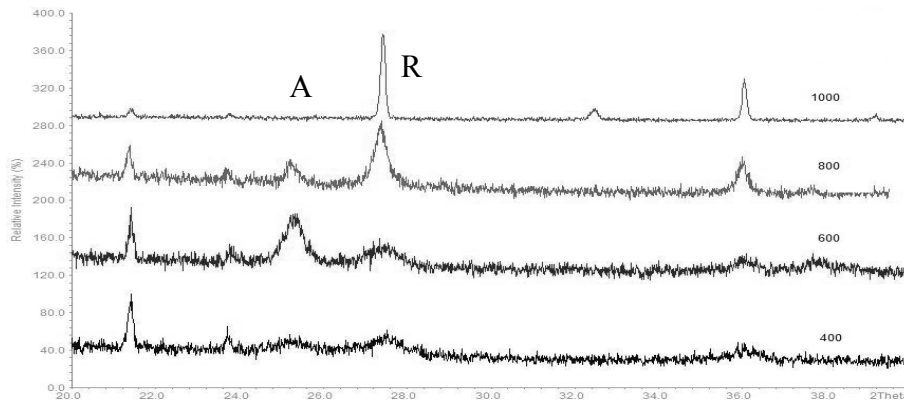


**Figure 3-13 : XRD patterns of samples after evaporation of solution, before drying(a) and after drying at temperatures of (b)90 °C (c)150 °C followed by heating at 600 °C. XRD patterns of samples after filtering and washing evaporated powder, before drying (d) and after drying and heating at 600 °C(e) (\* : peaks from sample mounting, @ :  $\text{NH}_4\text{NO}_3$ , A : anatase, R : rutile).**

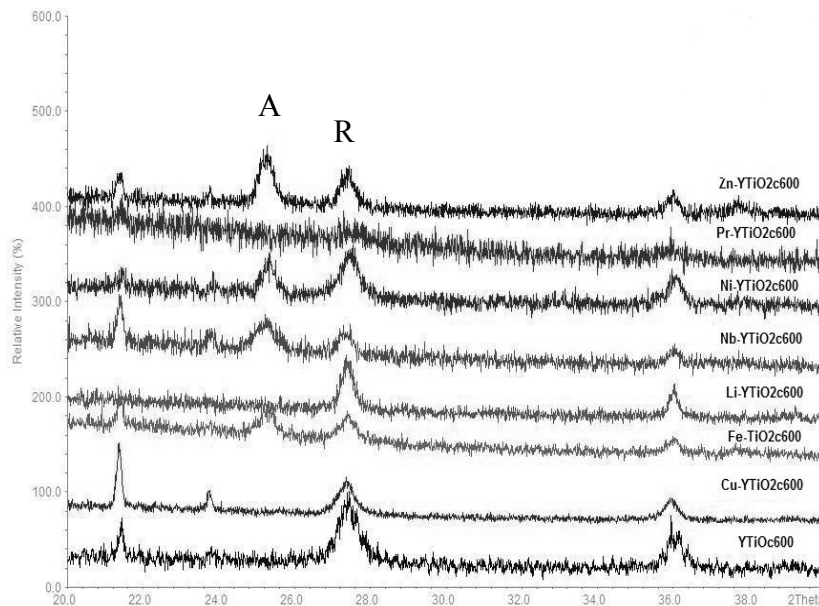
Titanium peroxy species in this method were thought to be  $\eta'$ -TiOOH because it is demonstrated that gentle drying of the TS-1-H<sub>2</sub>O<sub>2</sub>/H<sub>2</sub>O system leads to the transformation of the yellow peroxy groups into noncoloured species of  $\eta'$ -TiOOH, correlating with our synthesis that white precipitate was obtained when the red brown solution almost dry.<sup>125</sup>

Figure 3-14 shows phase transformation of yellow TiO<sub>2</sub> after evaporation and drying at 90 °C at various temperatures. As discussed before, acidity is favourable for rutile phase, the rutile phase is still produced in as prepared powder after drying at lower temperature than 150 °C. However, the anatase phase can be produced as well, which is different from drying at 150 °C. It may be confirmed that a milder combustion leads to the anatase phase appearing as a main phase at low temperature. When temperature reached 800 °C, the rutile phase is becomes the majority because anatase is a thermally metastable phase, while rutile is stable phase.

Apart from drying temperature, dopants or loaded elements affect the combustion condition and give a variety of phase content as well. When 5 mol% of Fe, Nb, Ni and Zn were added to the red brown solution before evaporating and drying at 150 °C, for which only a rutile phase would obtained in undoped yellow TiO<sub>2</sub>, various contents of anatase character were obtained after calcining at 600 °C as shown in figure 3-15. Milder combustion reaction was observed with lots of bubbling during drying, not like a typical combustion reaction sometimes. Dopants affect not only phase transformation temperature but also the amorphous character. Pr doped yellow TiO<sub>2</sub> is still amorphous even firing at 600 °C.



**Figure 3-14 : XRD patterns of powders prepared from acidic condition and drying at 90 °C after calcination at various temperatures.**



**Figure 3-15 : XRD patterns of impurity doping or loading yellow TiO<sub>2</sub> after calcination at 600 °C for 10 hours.**

Surface area is normally decreased with increasing temperature because of higher crystallinity, variation in surface area can also be affected by dopants. The surface area of yellow TiO<sub>2</sub> was higher with Nb dopant while the other dopants decrease surface area. Table 3-1 shows the physical properties of yellow TiO<sub>2</sub> after drying at 90 °C and 150 °C in various conditions. The introduction of metal ions and combustion

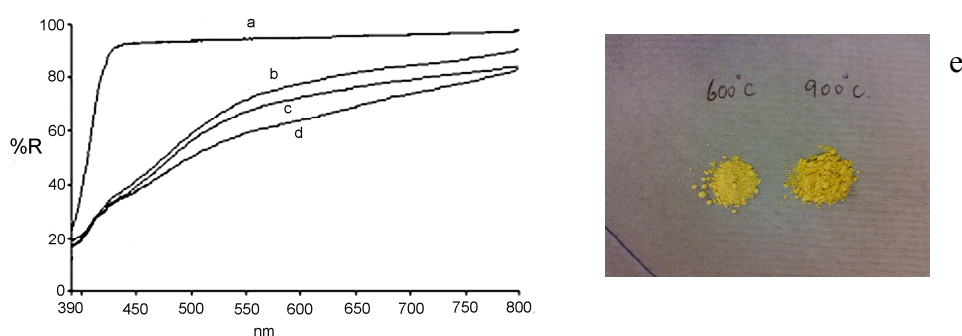
condition resulting from each dopant might affect to phase transformation of yellow TiO<sub>2</sub> as reported in some works that the physical properties of doped TiO<sub>2</sub> depends on dopants.<sup>127</sup>

SAMPLES		TEMP ( C )	XRD	BET(m <sup>2</sup> /g)	COLOUR
YTiO <sub>2</sub> Dry 90 °C	undoped	400	31% A : 69% R	117.46	pale yellow
		600	67% A : 33% R		pale yellow
		800	16% A : 84% R		pale yellow
		1,000	R		pale yellow
YTiO <sub>2</sub> dry150 °C	undoped	150	R		Yellow
		400	R	63.11	Yellow
		600	R	44.77	Yellow
		900	R	2.5	Yellow
		900+ball milled	R	3.40	Yellow
		1,200	R		brown- yellow
		1,350	R		Brown
	Ce <sub>0.05</sub> YTiO <sub>2</sub>	800	800(R+CeO <sub>2</sub> )	3.53	Yellow
	Cu <sub>0.05</sub> YTiO <sub>2</sub>	600	R		pale orange
		900	R		Grey
	Ni <sub>0.05</sub> YTiO <sub>2</sub>	600	24% A : 76% R		Green
	Nb <sub>0.05</sub> YTiO <sub>2</sub>	600	71% A : 29% R	65.19	Yellow
	Ce <sub>0.025</sub> Nb <sub>0.025</sub> YTiO <sub>2</sub>	800	R	4.02	Yellow
	Zn <sub>0.05</sub> YTiO <sub>2</sub>	600	55% A : 45% R	26.01	Yellow

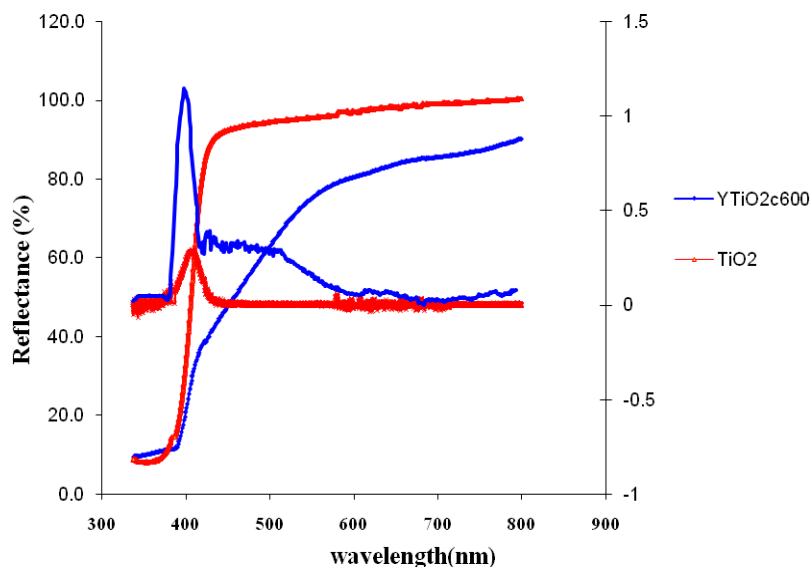
**Table 3-1 : Physical properties of yellow TiO<sub>2</sub> after drying at 90 °C and 150 °C under various conditions.**

### 3.2.2 UV-Visible diffuse reflectance

Usually, a blue shift of absorption edge of yellow TiO<sub>2</sub> with increasing heat treatment temperature may be observed.<sup>128</sup> The diffuse reflectance spectra and the image of yellow TiO<sub>2</sub> samples are shown in figure 3-16, which shows a red shift of the absorption edge into the visible region compared with commercial rutile TiO<sub>2</sub> and the red shift of adsorption edge increases with the treatment temperature. The wavelength of absorption edge can be seen more clearly by plotting as a differential as shown in figure 3-17. The commercial rutile TiO<sub>2</sub> has one peak around 400-410 nm. While two peaks can be observed for the yellow TiO<sub>2</sub> after calcination at 600 °C, one peak at 400-410 nm similar to the commercial rutile TiO<sub>2</sub> and another broad peak around 450-600 nm indicating that the absorption edge extending into visible region. The form of the reflectance spectrum indicates that the direct band gap is not changed on doping with trap states being introduced into the band gap, the broad character is possibly indication of indirect transition.

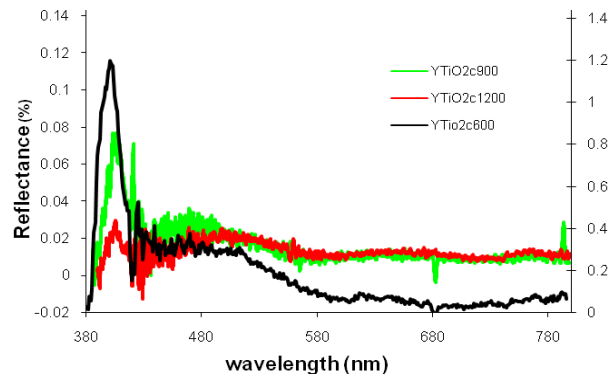


**Figure 3-16 : The UV-Visible diffuse reflectance of commercial rutile TiO<sub>2</sub> (a) and yellow TiO<sub>2</sub> after heating at (b)400 °C, (c)600 °C, (d)900 °C and (e) the image of yellow TiO<sub>2</sub>.**



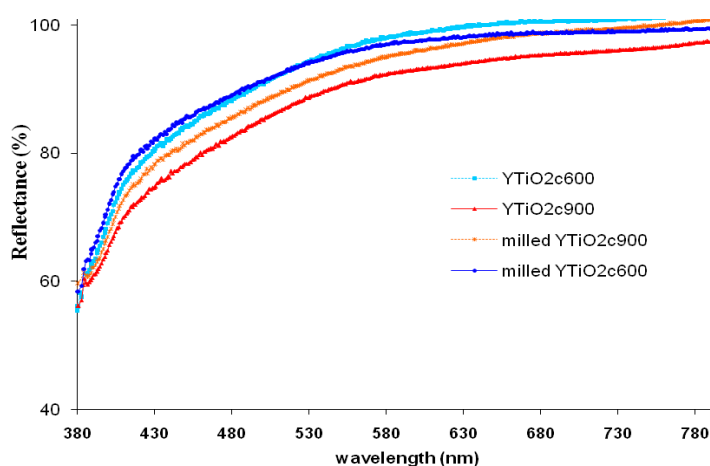
**Figure 3-17 : The UV-Visible diffuse reflectance and differential plot (right hand y-axis) of commercial rutile TiO<sub>2</sub> and 600 °C calcined yellow TiO<sub>2</sub>**

Comparing the differential plots of the yellow TiO<sub>2</sub> calcined at 600 °C, 900 °C and 1200 °C, it was found that the direct band gap is still in the range of 400-410 nm and the indirect band gap is fairly similar as shown in figure 3-18. However, a % reflectance slightly decreases with increasing treatment temperature (Figure 3-16). There are several factors that may affect the percentage of reflectance such as phase content, particle size, absorption capacity of metal dopant, composition.<sup>17,51,129</sup> Since this is the same sample, same phase and is undoped, particle size might influence to the shape and % reflectance of spectrum. The bigger particle size of crystalline powder shows a lower % reflectance than smaller particle size powder because the increased scattering caused by larger particle, larger grain size and surface roughness results in reduced reflection.<sup>130,131</sup>



**Figure 3-18 : The differential plot of yellow TiO<sub>2</sub> calcined at 600 °C (right hand y-axis), 900 °C and 1,200 °C ( left hand y-axis)**

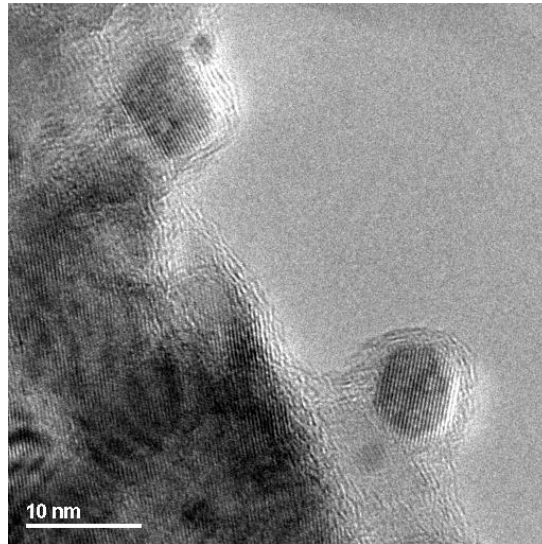
The yellow TiO<sub>2</sub> calcined at 600 °C and 900 °C have been ball milled for 1 h in order to clarify whether differences in indirect band gap come from difference of particle size. UV-Visible diffuse reflectance spectra of yellow TiO<sub>2</sub> calcined at 600 °C and 900 °C comparing before and after ball milling were not different in terms of adsorption edge and trend but % reflectance is slightly different as shown in figure 3-19. Reflectance percentage was a little bit increased in the 900 °C calcination sample revealing the increase of % reflectance caused by decreasing of particle size, presumed by an increase of surface area from 2.5 to 3.4 m<sup>2</sup>/g. Spectra are quite similar for 600 °C calcination sample because particle size is quite small so that ball milling didn't make any difference resulting in the same % reflectance. However, the shape of spectra of yellow TiO<sub>2</sub> obtained from various calcination temperatures are different with both red shift of band edge and reduction of % reflectance, it may be concluded that particle size is not the main issue causing a red shift of these samples, probably due to difference degree of oxygen deficiency leading to reduction of % reflectance as reported in some work.<sup>76</sup>



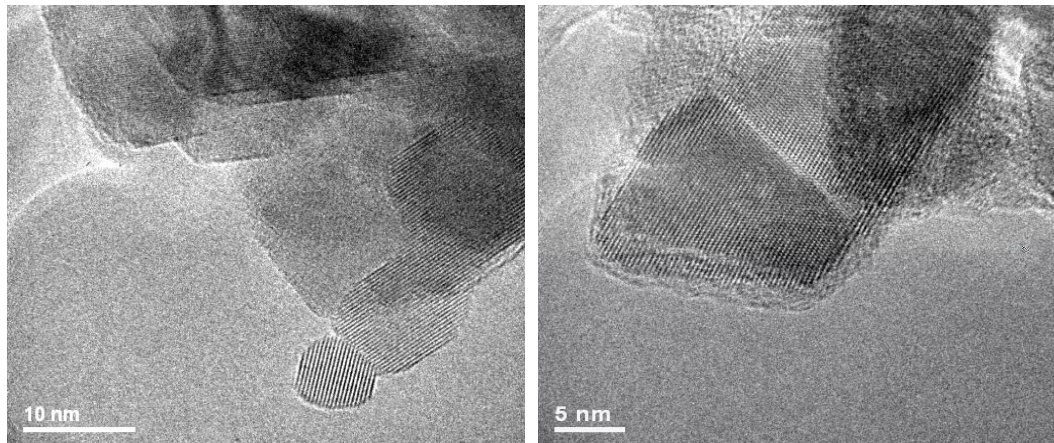
**Figure 3-19 : UV-Visible diffuse reflectance spectra of YTiO<sub>2</sub> calcined at 600 °C and 900 °C comparing before and after ball milling.**

### 3.2.3 TEM

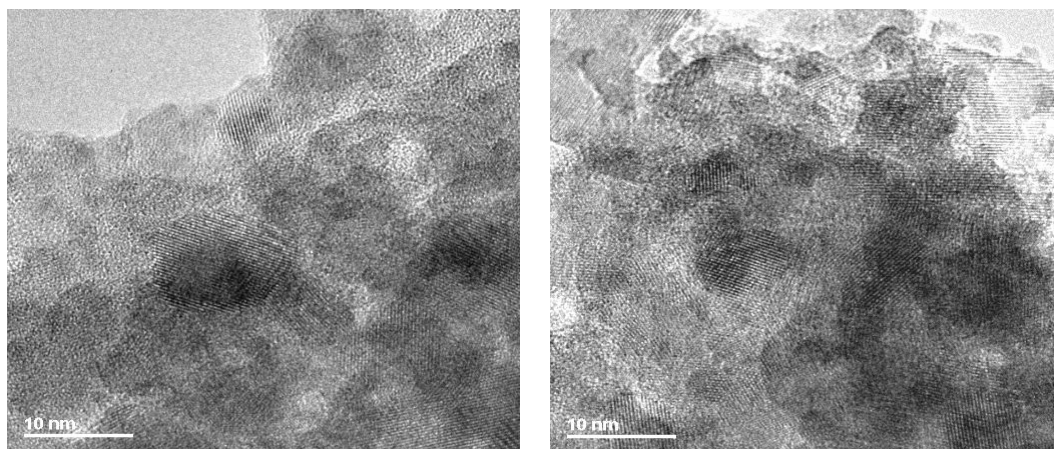
TEM images of yellow TiO<sub>2</sub> after calcining at 400 °C, 600 °C, 900 °C and 1,350 °C are shown in figures 3-20, 3-21, 3-22 and 3-23 respectively. Nanoparticlar TiO<sub>2</sub> around 5-20 nm can be prepared by this method. Crystalline particles were observed in all samples although it was not quite clear in some areas as amorphous character was observed as well. It is notable that crystalline-amorphous core shell TiO<sub>2</sub> might be obtained, even at high temperature. Core shell TiO<sub>2</sub> character can be seen clearly from the TEM image of the 400 °C sample.



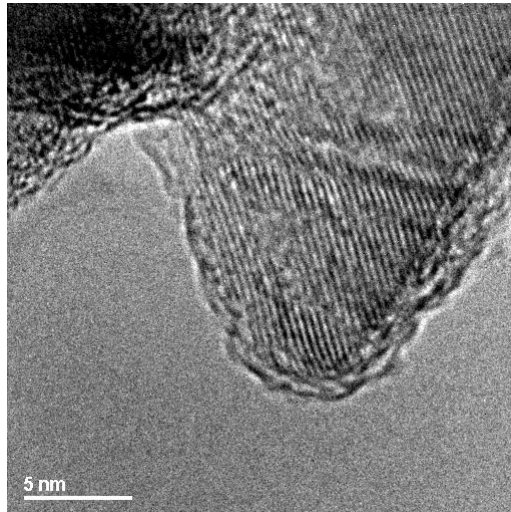
**Figure 3-20 : TEM images of yellow TiO<sub>2</sub> after calcining at 400 °C.**



**Figure 3-21 : TEM images of yellow TiO<sub>2</sub> after calcining at 600 °C.**

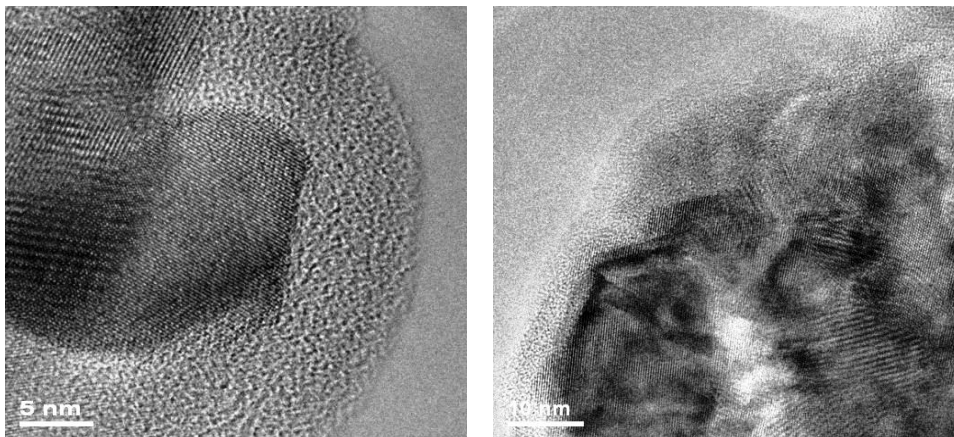


**Figure 3-22 : TEM images of yellow TiO<sub>2</sub> after calcining at 900 °C.**



**Figure 3-23 : TEM images of yellow TiO<sub>2</sub> after calcining at 1,350 °C.**

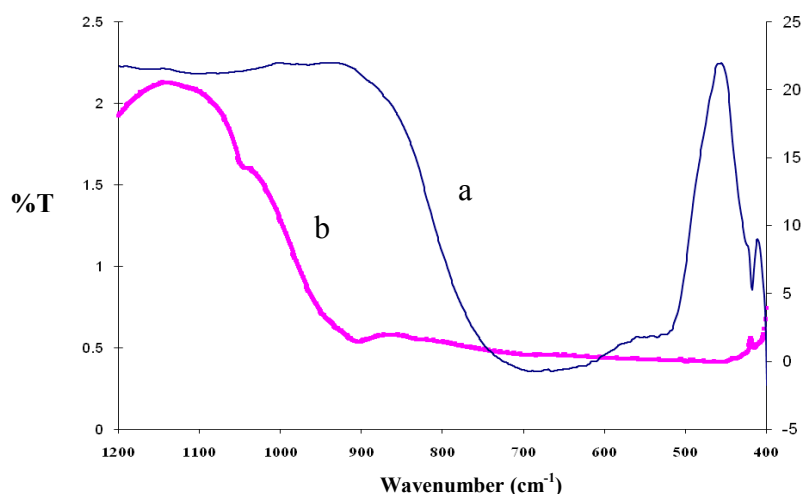
TEM images of Ni doped yellow TiO<sub>2</sub> and firing at 600 °C, which shows more amorphous character than naked yellow TiO<sub>2</sub>, were shown in figure 3-24.



**Figure 3-24 : TEM images of Ni doped yellow TiO<sub>2</sub> after calcining at 600 °C.**

### 3.2.4 FT-IR

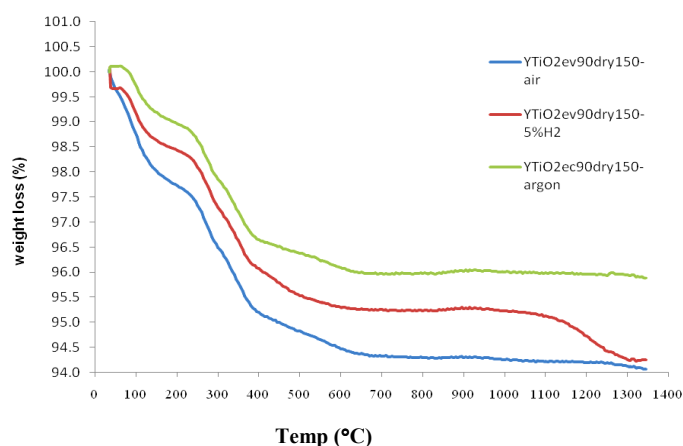
Infrared spectrum of yellow  $\text{TiO}_2$  after calcination at  $600\text{ }^\circ\text{C}$  is presented in figure 3-25. It shows two broad absorption bands at  $520\text{ cm}^{-1}$  and  $679\text{ cm}^{-1}$  and one sharp absorption band at  $418\text{ cm}^{-1}$  which is consistent with two broad absorption bands between  $450\text{-}750\text{ cm}^{-1}$  and one band at  $420\text{ cm}^{-1}$  of rutile  $\text{TiO}_2$ .<sup>132,133</sup> There is no absorption band around  $880\text{-}900\text{ cm}^{-1}$  of peroxy vibration which was seen in yellow amorphous titanium peroxy sample obtained by using the same precursor as yellow  $\text{TiO}_2$  but precipitating the red brown solution with ammonia solution, then filtration and dry at room temperature.<sup>83,84,87,119,120</sup>



**Figure 3-25 : FT-IR spectra of yellow  $\text{TiO}_2$  after calcining at  $600\text{ }^\circ\text{C}$  (a) compared with Yamor-pH2 (b)**

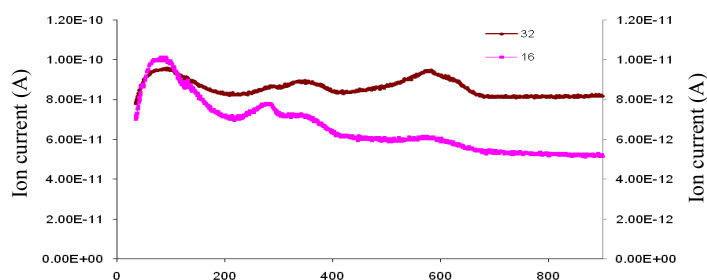
### 3.2.5 TGA

The weight loss of as prepared yellow  $\text{TiO}_2$  dried at  $150\text{ }^\circ\text{C}$  differs slightly depending on treatment atmosphere, with weight loss in air  $>$   $\text{H}_2 >$  argon as shown in figure 3-26. Considerable weight losses can be observed in  $\text{H}_2$  at temperature higher than  $1,100\text{ }^\circ\text{C}$  because of phase transformation, as XRD pattern changes from rutile at  $900\text{ }^\circ\text{C}$  to no peaks at  $1,350\text{ }^\circ\text{C}$ .

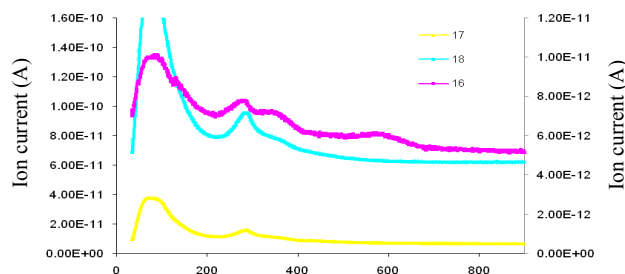


**Figure 3-26 : Thermogram of yellow  $\text{TiO}_2$  after drying at  $150\text{ }^\circ\text{C}$  under different atmospheres.**

Investigation of evolved molecules during heating on in situ decomposition by using mass spectrometer indicating that weight loss up to  $300\text{ }^\circ\text{C}$  was adsorbed water as peaks of mass number 17 and 18 of water parent molecule were detected. There may be some  $\text{O}_2^{2-}$  decomposed as well in this region since mass number 16 and 32 signals were observed as shown in figure 3-27 and 3-28. However, it is clearly shown that  $\text{O}_2^{2-}$  was the main species to decompose during  $300\text{-}600\text{ }^\circ\text{C}$  since the peaks of mass number 16 and 32 of  $\text{O}_2$  decomposition were parallel in appearing against temperature as shown in figure 3-27.

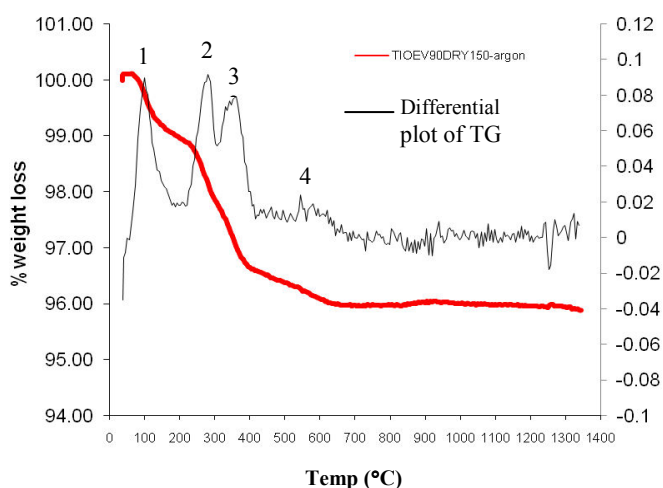


**Figure 3-27 : Mass spectra of mass number 16 (right hand y-axis) and 32 (left hand y-axis) of O<sub>2</sub> parent molecule.**



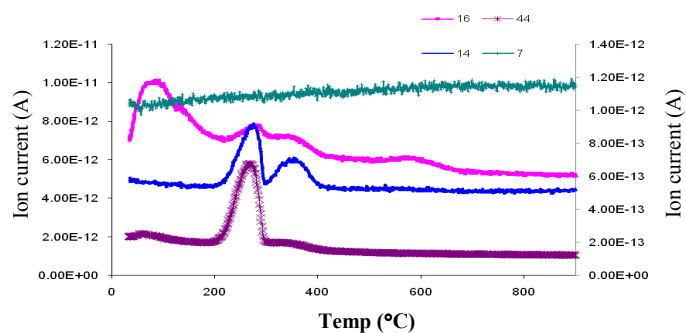
**Figure 3-28 : Mass spectra of mass number 16, 17 (right hand y-axis), and 18 (left hand y-axis) of H<sub>2</sub>O parent molecule.**

Figure 3-29 shows a differential plot of thermogram of the yellow TiO<sub>2</sub> after drying at 150 °C under argon. It can be seen that there are 4 main peaks that indicate the changes during heating. These peaks are consistent with the mass spectra of mass number 16, 17, 18 and 32. It might be concluded that peak 1 at around 100 °C and peak 2 at around 300 °C were associated with H<sub>2</sub>O and O<sub>2</sub> parent molecules, whereas peak 3 at around 300-400 °C and peak 4 at around 600 °C were associated with O<sub>2</sub> parent molecule.



**Figure 3-29 : Thermogram of yellow TiO<sub>2</sub> after drying at 150 °C under argon atmosphere with heating rate 5°C/min and differential plot (right hand y-axis)**

Moreover, mass number 7, 14, 16, 28, 44 (figure 3-30) and 14,17 (figure 3-31) of plausible parent molecules N<sub>x</sub>O<sub>x</sub> and NH<sub>3</sub> were measured. It can be seen that these spectra have no parallel at each temperature, indicating that there is no nitrogen incorporation in this sample. However, there are very low intensity of mass number 14 and 44, probably due to the evolution of CO<sub>2</sub> that adsorbed on the surface of the yellow TiO<sub>2</sub> as the chemisorption of CO<sub>2</sub> onto the surface of TiO<sub>2</sub> is usual and the adsorption and thermal desorption of CO<sub>2</sub> has been used to identify the surface properties of TiO<sub>2</sub>.<sup>134</sup>



**Figure 3-30 : Mass spectra of mass number 7, 14 (right hand y-axis), 16 (left hand y-axis) and 44 (right hand y-axis) of N<sub>x</sub>O<sub>x</sub> and CO<sub>2</sub> molecule.**

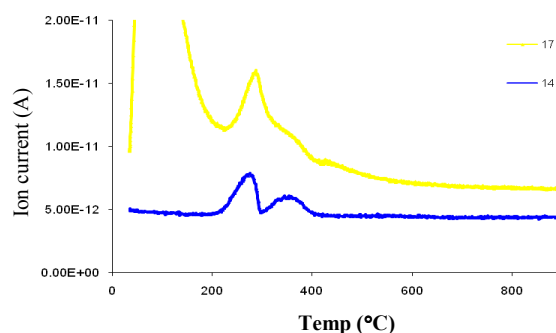


**Figure 3-31 : Mass spectra of mass number 14 and 17 of NH<sub>3</sub> parent molecule.**

As TG-MS was operated under argon, in order to reveal oxygen involvement, weight loss was lower than in air, probably owing to less reaction during firing as lack of oxygen. Thermogram comparing between various temperatures shows a steeper slope of weight loss from 400-600 °C in air and weight loss is more than in argon as shown in figure 3-26. Peroxo group might be less remaining or completely removed at 600 °C when firing in air atmosphere.

### 3.2.6 ESR

Yellow TiO<sub>2</sub> contained a paramagnetic species possessing a strong signal in the ESR spectrum at room temperature and pressure as shown in figure 3-32. As prepared powder (figure 3-32a) and 600 °C calcination sample (Figure 3-32b) showed a similar strong signal at  $g \sim 1.97$  while samples calcined at 900 °C (Figure 3-32c) and 1,200 °C (Figure 3-32e) show a broad and sharp signal at  $g \sim 2.003$ , respectively. An electron trapped on an oxygen vacancy is suggested relate to  $g \sim 2.003$ . The existence of  $g \sim 1.97$  indicates that Ti<sup>3+</sup> is present which may be confirmed by the formation of the same signal of Ti<sup>3+</sup> caused via surface photoreduction of TiO<sub>2</sub> by *in situ* UV

illumination of 900 °C sample (figure 3-32d). These g values differ from the g values and spectrum character of  $O_2^-$ ,  $O_3^-$  and nitrogen species.<sup>81,135,136,137,138</sup> The g values of  $O_2^-$  were  $g_1 \sim 2.019$ ,  $g_2 \sim 2.010$ ,  $g_3 \sim 2.003$  and g values of  $O_3^-$  were  $g_1 \sim 2.014$ ,  $g_2 \sim 2.010$ ,  $g_3 \sim 2.002$ . Valentin et al.<sup>77</sup> have analysed N-doped  $TiO_2$  by using ESR and found that two types of paramagnetic species were detected. Type I consists of molecular nitrogen oxide species, NO ( $g_1 \sim 2.001$ ,  $g_2 \sim 1.998$ ,  $g_3 \sim 1.927$ ), and  $NO_2$  ( $g_1 \sim 2.004$ ,  $g_2 \sim 2.001$ ,  $g_3 \sim 1.990$ ), trapped in microvoids of the solid. Type II is the paramagnetic nitrogen species ( $g_1 \sim 2.005$ ,  $g_2 \sim 2.004$ ,  $g_3 \sim 2.003$ ). Joung et al.<sup>139</sup> also reported ESR signal of N-doped  $TiO_2$  that N-doped  $TiO_2$  produced three g values at  $g_1 \sim 1.97$ - $1.99$ ,  $g_2 \sim 2.003$ ,  $g_3 \sim 2.018$ .

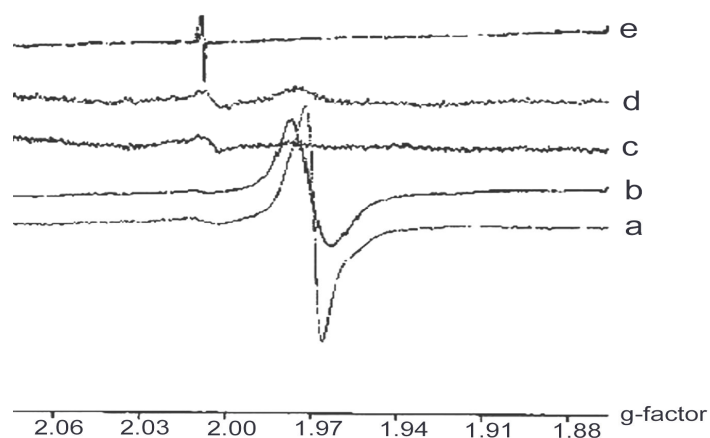


**Figure 3-32 : ESR spectra of (a) as prepared powder after 150 °C drying, after heating at (b) 600 °C, (c) 900 °C, (d) 900 °C +UV and (e) 1,200 °C.**

### 3.2.7 XPS

No nitrogen can be detected by XPS measurements either as shown in figure 3-33. Ti and O XPS data confirm the presence of  $Ti^{3+}$  with an additional set of Ti peaks and broadening of the O XPS signal. The  $Ti^{4+}$  and  $Ti^{3+}$  peaks are of similar intensities indicating a high surface  $Ti^{3+}$  concentration as shown in figure 3-34. Broadening of the O XPS signal is observed with additional set of O peaks at lower binding energy indicating that different environment of oxygen are present. Normally there are two O1s peaks detected from XPS, which are a small peak of oxygen from surface hydroxyl groups at higher binding energy and main peak of lattice oxygen in  $TiO_2$  at lower binding energy.<sup>121,122</sup> Sometimes there may be one more at higher binding energy than surface oxygen of O-C as shown in  $TiO_2$  spectrum in figure 3-35, possibly due to using graphite as an internal standard during operation. However, an O1s peak at lower binding energy than lattice of oxygen can be observed in case of  $YTiO_2c600$ , probably it is an oxygen from oxygen deficiency or O- $Ti^{3+}$ . Ti species are also different from titanium species on the surface of TiN, which always consists of three peaks of titanium oxynitride species, not just  $Ti^{3+}$ .<sup>140-146</sup>

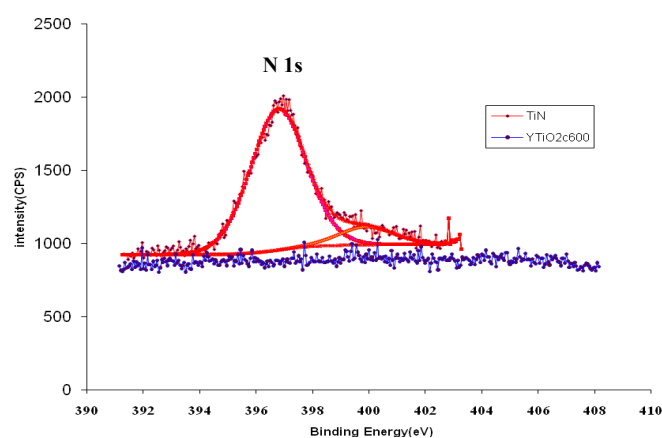


**Figure 3-33 : XPS spectra of N species in TiN compared with yellow  $TiO_2$  calcined at 600 °C.**

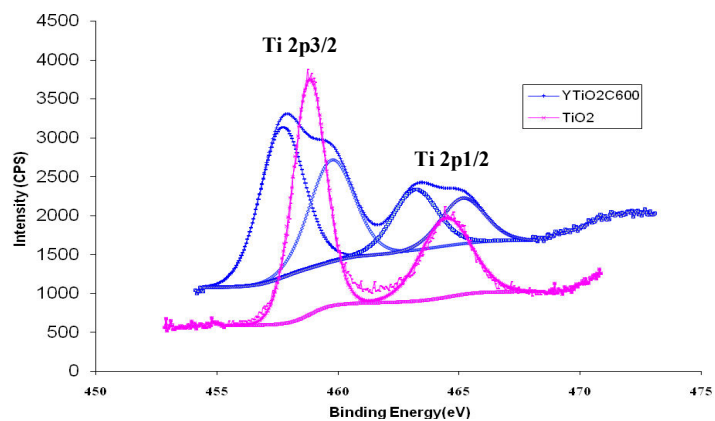


**Figure 3-34: XPS spectra of Ti species in TiO<sub>2</sub> compared with yellow TiO<sub>2</sub> calcined at 600 °C.**

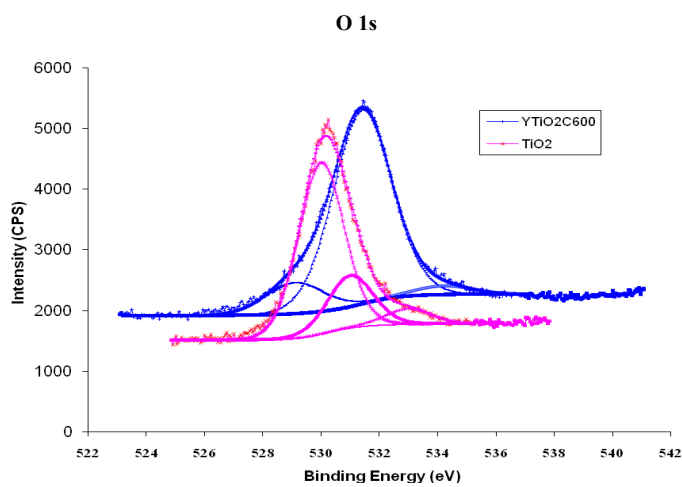


**Figure 3-35 : XPS spectra of O species in TiO<sub>2</sub> compared with yellow TiO<sub>2</sub> calcined at 600 °C.**

### 3.2.8 Magnetometry

Magnetic properties have normally been reported in doped TiO<sub>2</sub> as leading to generation of Ti<sup>3+</sup>.<sup>147-150</sup> The magnetization versus temperature (zero field cooled) of yellow TiO<sub>2</sub> compared with commercial rutile TiO<sub>2</sub> is shown in figure 3-36. The paramagnetic property of yellow TiO<sub>2</sub> is consistent with data from ESR and XPS measurements, while commercial rutile TiO<sub>2</sub> is diamagnetic. Figure 3-37 shows a linear correlation between molar susceptibility and reciprocal temperature of yellow TiO<sub>2</sub> calcined at 600 °C, which gives C = 0.00017. An effective magnetic moment calculated from the obtained Curie constant according to

$$C = \frac{N\mu_{eff}^2}{3k_B}$$

is 0.037 Bohr magnetons. Comparison with 1.732 Bohr magnetons of the effective magnetic moment of Ti<sup>3+</sup>, it may be concluded that 2.13% of total Ti is Ti<sup>3+</sup> in yellow TiO<sub>2</sub> after calcination at 600 °C. This is consistent with a value around 2% obtained from a weight gain in TGA when reoxidising the yellow TiO<sub>2</sub> calcined at 600 °C from room temperature to 900 °C. It implies that there is a significant bulk concentration of Ti<sup>3+</sup> and that it is not a surface species only.

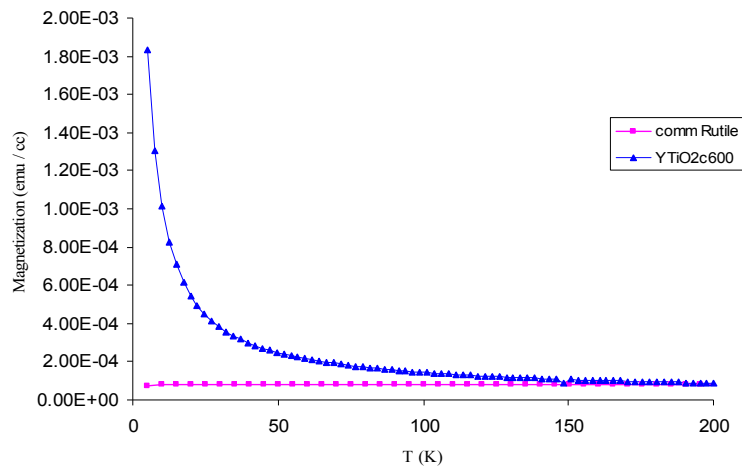


**Figure 3-36 : Magnetisation of commercial rutile  $\text{TiO}_2$  and 600 °C calcined yellow  $\text{TiO}_2$ .**

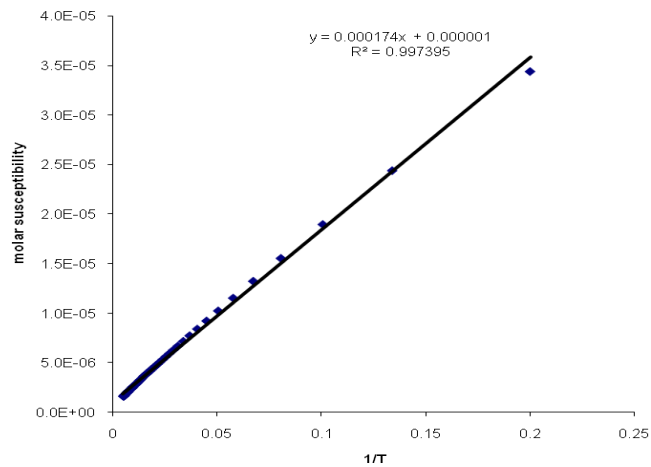


**Figure 3-37 Molar susceptibility versus reciprocal temperature of yellow  $\text{TiO}_2$  calcined at 600 °C**

### 3.2.9 SEM

As the colour of yellow  $\text{TiO}_2$  turns to brown when calcined at temperature higher than 1,200 °C, it is interesting to investigate some properties of the yellow  $\text{TiO}_2$  after calcination at very high temperature. It was found that an intense brown coloured powder was obtained after calcination as prepared yellow  $\text{TiO}_2$  at 1,350 °C. SEM image was shown in figure 3-38, it shows a large grain size. A shiny brown pellet is

obtained by sintering the yellow  $\text{TiO}_2$  calcined at  $600\text{ }^\circ\text{C}$  at  $1,350\text{ }^\circ\text{C}$  for 10 hours as shown in figure 3-39.

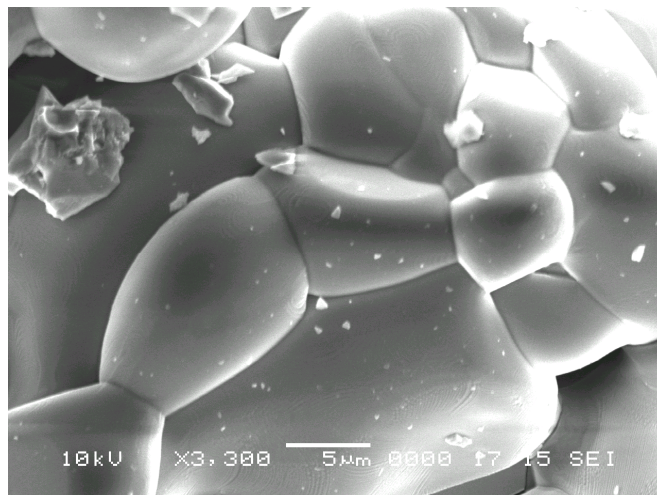


**Figure 3-38 : SEM image of the yellow  $\text{TiO}_2$  powder after calcining at  $1,350\text{ }^\circ\text{C}$ .**



**Figure 3-39 : Image of the yellow  $\text{TiO}_2$  pellet calcined at  $1,350\text{ }^\circ\text{C}$ .**

### 3.2.10 Conductivity dependence upon $p(\text{O}_2)$

Since the yellow  $\text{TiO}_2$  pellet calcined at  $1,350\text{ }^\circ\text{C}$  is apparently quite dense and the colour is quite different from the commercial  $\text{TiO}_2$ , conductivity measurement was investigated.

The isothermal electrical conductivity as a function of oxygen might be used to identify type of material. In an n-type, conductivity increases with decreasing  $p(\text{O}_2)$  where conductivity increases with increasing  $p(\text{O}_2)$  in a p-type. The yellow  $\text{TiO}_2$  sintered at  $1,350\text{ }^\circ\text{C}$  might be classified as the n-type  $\text{TiO}_2$  since conductivity increases with decreasing  $p(\text{O}_2)$  as shown in figure 3-40.

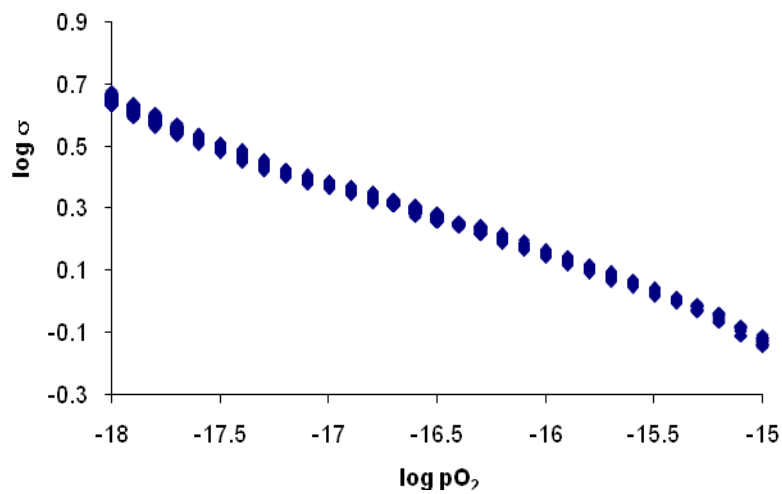


**Figure 3-40 : Electrical conductivity of the yellow  $\text{TiO}_2$  sintered at  $1,350\text{ }^\circ\text{C}$  as a function of oxygen activity at  $900\text{ }^\circ\text{C}$**

Activation energy of  $0.114\text{ eV}$  and  $0.074\text{ eV}$  can be obtained from the Arrhenius plot of electrical conductivity of yellow  $\text{TiO}_2$  sintering at  $1,350\text{ }^\circ\text{C}$  in air (Figure 3-41) and after reducing in  $5\%\text{H}_2$  at  $900\text{ }^\circ\text{C}$  (Figure 3-42), respectively. Electrical conductivity of the reduced yellow  $\text{TiO}_2$  sintered at  $1,350\text{ }^\circ\text{C}$  is quite high, it can reach  $12\text{ S/cm}$  and continue increasing during isothermal treatment at  $900\text{ }^\circ\text{C}$ .

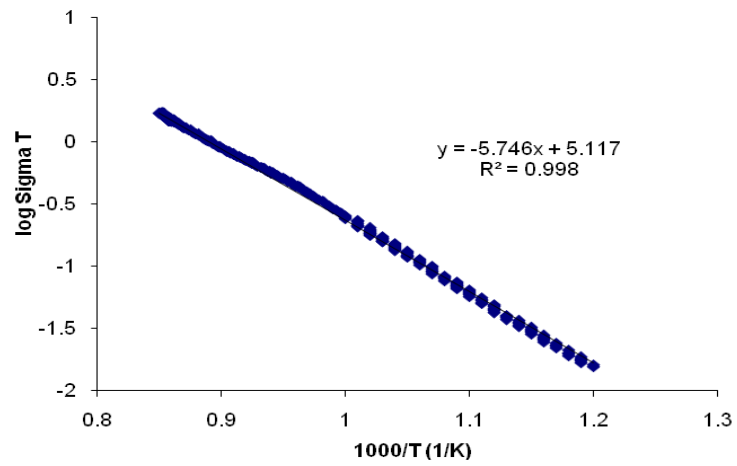


**Figure 3-41 : Arrhenius plot of electrical conductivity of yellow TiO<sub>2</sub> sintering at 1,350 °C in air**

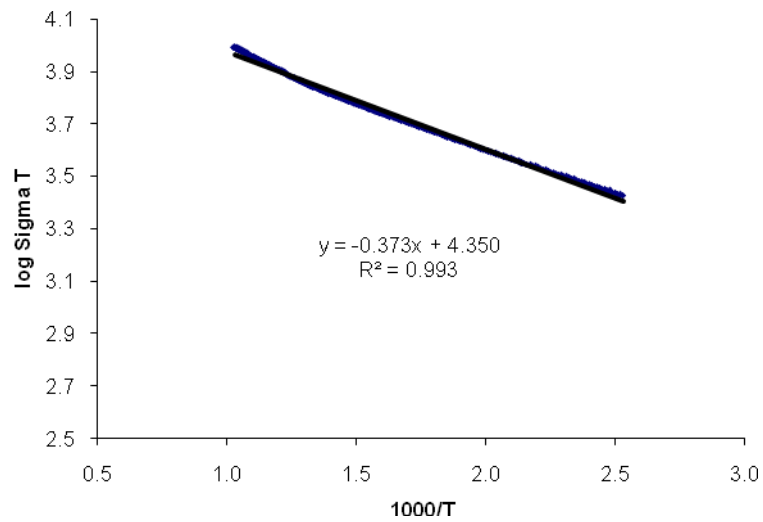


**Figure 3-42 : Arrhenius plot of electrical conductivity of yellow TiO<sub>2</sub> sintering at 1,350 °C in 5% H<sub>2</sub>**

## Summary

Nanoparticle yellow rutile  $\text{TiO}_2$  can be synthesised at low temperature by a clean, low cost and  $\text{CO}_2$  free method as using  $\text{TiN}$ ,  $\text{H}_2\text{O}_2$  and  $\text{HNO}_3$  as precursors. Combustion reaction of titanium peroxo,  $\eta^1$ - $\text{TiOOH}$  and  $\text{NH}_4\text{NO}_3$ , by products of dissolution of  $\text{TiN}$  detected by XRD, were proposed. Acid catalysis is found to favour rutile phase formation with anatase being produced by this method in basic condition. The  $\text{Ti}^{3+}$  and the oxygen vacancy are the key factor in the yellow colour as can be detected by ESR, XPS and SQUID with no evidence of nitrogen species from XPS, elemental analysis, ESR, TG-MS and no evidence of peroxo group from FT-IR and ESR.

Defects might come from a removal of peroxo group during combustion reaction as there are some reports on  $\text{Ti}^{3+}$  formation by removing a lattice oxygen atom and electron in vacuum or reducing atmosphere<sup>151</sup> or by removing of the terminal titanium alkoxide group on surface during calcination in oxidising atmosphere and produced defect of oxygen vacancy site.<sup>137</sup> Furthermore,  $\text{Ti}^{3+}$  might be occurred by the reduction of  $\text{Ti}^{4+}$  at dangling bonds with an electron left in it on the surface of amorphous or nanosized material<sup>152,153</sup> as amorphous shell character can be seen from TEM.

## CHAPTER 4

### Results and discussion on photodecolourisation of methylene blue

The photodecolourisation of Methylene blue has been widely studied in heterogeneous photocatalysis. However, there are some concerns about the bleaching of MB due to the photoreduction to colourless form<sup>154,155</sup> and photoabsorption of MB.<sup>157</sup> There are two main forms of MB, the blue colour of oxidised form (MB) and the colourless reduced form (leuco form, LMB). MB can be photoreduced to LMB by TiO<sub>2</sub> under UV light under anaerobic condition and in the presence of a sacrificial electron donor. It was found that MB itself can act as the sacrificial electron acceptor.<sup>154</sup> However, this process is reversed on the addition of O<sub>2</sub> to the anaerobic system. Although LMB is readily oxidised back to MB by oxygen, this reaction depends on pH. The rate increases with pH, LMB is moderately stable under acidic condition but reacts rapidly with air under basic condition.<sup>155</sup> As continuous air bubbling of a neutral solution was utilised in this work and no reducing agent was added to the system, it is likely that the dominant bleaching process is the photomineralisation of MB rather than the reductive formation of LMB. This system, MB/TiO<sub>2</sub>/air-saturated water system, has widely been utilised for the demonstration of semiconductor photocatalysis,<sup>156</sup> as reviewed by Mills and Wang.<sup>154</sup> It is possible or even probable that partial rather than complete mineralisation into CO<sub>2</sub>, NH<sub>4</sub><sup>+</sup>, NO<sub>3</sub><sup>-</sup>, and SO<sub>4</sub><sup>2-</sup> is occurring as the main observable in bleaching MB. The photoabsorption of MB can be an issue for visible light driven photocatalyst investigation because MB can absorb visible light, especially, in the range 600–700 nm. Yan et al.<sup>157</sup> concluded that MB was not an appropriate substrate for a visible-light photocatalytic activity test particularly in the range of 540–680 nm irradiation. However, the most important and

intense emitting wavelength of the metal halide lamp used in this work is in the range of about 200–580 nm. After equipping with a UV cut-off filter, the emitting wavelength is in the range of 420–580 nm, which has little overlap with the absorption of MB as shown in Fig.4-1. As a result, the photoabsorption of MB should not significantly effect the determination of visible light photocatalytic activity test in this work.

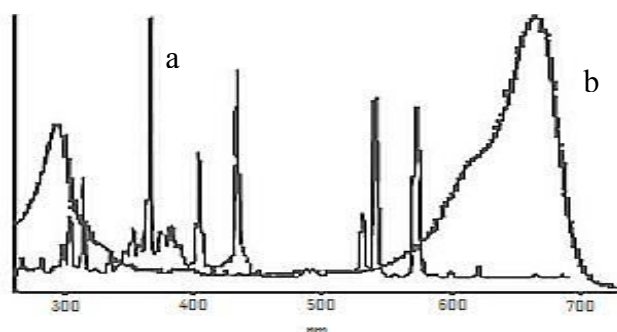


**Figure 4-1 : The emitting wavelength of metal halide lamp (a) and UV-Vis absorption spectrum of MB (b).**

% Decolourisation is calculated by

$$decolourisation(\%) = \left( \frac{C_i - C_t}{C_i} \right) \times 100$$

where

$C_i$  = initial concentration of MB

$C_t$  = concentration of MB at any time, t

#### 4.1 Yellow amorphous TiO<sub>2</sub>

It was found that 10% bleaching of MB was shown after visible light irradiation of only MB for 5 hours (Figure 4-2a), whereas slightly higher, 15% photodecolourisation of MB, was obtained by using 0.5 g/L Yamor-pH10 as photocatalyst (Figure 4-2b). However, the latter amount was obtained after 45% of  $1 \times 10^{-4}$  M MB was adsorbed, indicated that the initial concentration of MB before photodecolourisation was about  $5.5 \times 10^{-5}$  M. Comparison with using 0.5 g/L Yamor-pH2, about 97% adsorption and 2% photocatalytic activity was measured (Figure 4-2c). It can be concluded that the adsorption capacity of Yamor-pH2 was significantly higher than Yamor-pH10, however, the extent of adsorption must hinder the heterogeneous photoactivity. Therefore, a decreased amount of Yamor-pH2 to 0.2 g/L was performed for photoactivity comparison (Figure 4-2d). It can be seen that about 46% photodecolourisation of MB after adsorption was obtained, which was considerably higher than using Yamor-pH10 in spite of using less photocatalyst and a higher concentration of MB remained after adsorption. Moreover, only 9% photodecolourisation was observed for 0.5 g/L of Degussa P25 in  $1 \times 10^{-5}$  M MB under visible light for 2 hours (compared to 93% under UV for 1 hour) showing that the Yamor-pH2 was much more effective, ~40% under visible light for 2 hours. An important point to note is that the adsorbed MB seemed much less intense in colour and indeed the colour had changed to pale purple/violet. This could indicate a thionine intermediate formation by N-demethylation of MB.<sup>57</sup>

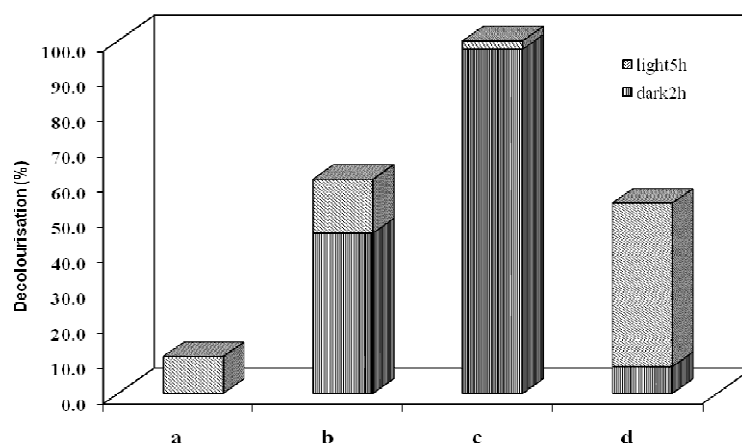
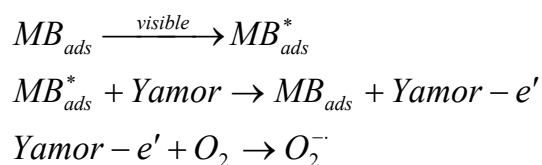


**Figure 4-2 : Photocatalytic decolourisation of MB comparing (a) blank test ( $2 \times 10^{-5}$ M MB), (b) 0.5g/l Yamor-pH10, (c) 0.5g/l Yamor-pH2 and (d) 0.2g/l Yamor-pH2.**

The irreversibility of the photodecolourisation process on continuous air bubbling for 24 hours in the dark after complete decolourisation of MB and the disappearance of the bands associated with MB (294 nm and 665 nm) with no appearance of band associated with LMB (256 nm)<sup>155</sup> as shown in figure 4-3 were observed, further confirm that photoreduction of MB to LMB was not the dominant process.

However, as Yamor adsorbed a high amount of MB, a photosensitisation of MB owing to the visible light photoabsorption might be significant in this case,<sup>157</sup> although MB just absorb small proportion of the emitting wavelength of the lamp in the range 570 – 580 nm. A possible mechanism is the adsorbed MB is excited by the visible light and injects electron into Yamor, followed by a formation of reactive oxygen species at the surface, resulting in the oxidative decomposition of the electron deficient MB.



These results show that Yamor-pH2 can act as a visible light-driven photocatalyst better than Yamor-pH10, in parallel with a red shift of the absorption edge into the visible region. However, an increase in visible absorption edge does not guarantee consistency in visible light photoactivity, recombination and surface area are also important factors.

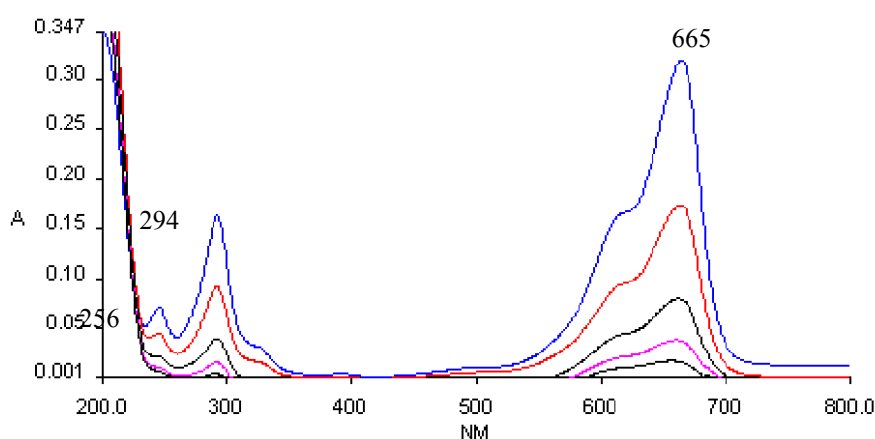


**Figure 4-3 : Decrease of UV-Vis absorption spectra of MB (294nm and 665 nm) after photodecolourisation for several hours with no appearance of LMB (256 nm).**

Recyclability and stability of photocatalysts are important factors for any practical applications. Therefore, we have attempted to investigate cyclability and stability. In general, the photoactivity of crystalline  $\text{TiO}_2$  is observed by monitoring the degradation of MB in an aqueous solution. Adsorbed MB is not usually concern probably due to small amount of MB that was adsorbed on crystalline  $\text{TiO}_2$ . The recyclability of crystalline  $\text{TiO}_2$  is normally assessed by elimination of adsorbed MB on  $\text{TiO}_2$  by oxidation at temperatures greater than  $190\text{ }^\circ\text{C}$ , which is the decomposition temperature of MB. However, removal of adsorbed MB by calcination cannot be used in the case of the amorphous form because crystallisation will be induced. As a result,

the cyclability of Yamor-pH2 was measured by two different methods, with and without removal of adsorbed MB. The first way, completely remove adsorbed MB on the surface by using photoactivity itself until the original colour of Yamor-pH2 was recovered. Due to a large amount of MB being adsorbed on the surface, 48 hours UV irradiation was used for adsorbed MB removal in order to reduce the duration of adsorbed MB removal and to evaluate the stability of Yamor-pH2 under UV light simultaneously. Figure 4-4 shows the recyclability by using UV irradiation for adsorbed MB removal. The 0.5 g/L ratio of catalyst to volume of MB was chosen because of the incomplete MB adsorption, hence, the visible-light photoactivity can be monitored, and the quantity of catalyst will be sufficient for removal of the high amount of adsorbed MB in 48 hours. About 97% adsorption and 2% photoactivity in 5 hours were obtained in the preliminary photoactivity test (Figure 4-4a). After the mixture was irradiated with UV light for 48 hours, the violet powder of visible light irradiated/adsorbed MB was changed to yellow powder as the original colour with a small amount of violet specks. Some violet specks indicated incomplete removal of adsorbed MB. Thereafter, the colourless aqueous solution was removed from the mixture by rinsing and the remaining powder left to dry at room temperature. The first reuse was performed by reading 200 mL of  $1 \times 10^{-4}$  M MB. A slight decrease of adsorption and photoactivity was obtained for the first and second recycles (Figure 4-4b, c). A small decrease of adsorption capacity and photoactivity presumably caused by incomplete adsorbed MB removal and decrease of efficiency or stability of amorphous structure after prolonged UV irradiation. The colour changing from yellow to pale yellow can be observed by the naked eye (XRD data showed that it remained amorphous in structure). However, if considering only photoactivity by using MB concentration after adsorption, about  $2 \times 10^{-5}$  M estimated from the

percentage of bleaching, as an initial concentration, about 80% bleaching of MB under visible light irradiation can be reached in 5 hours both in the first and second recycles (Figure 4-4d, e).

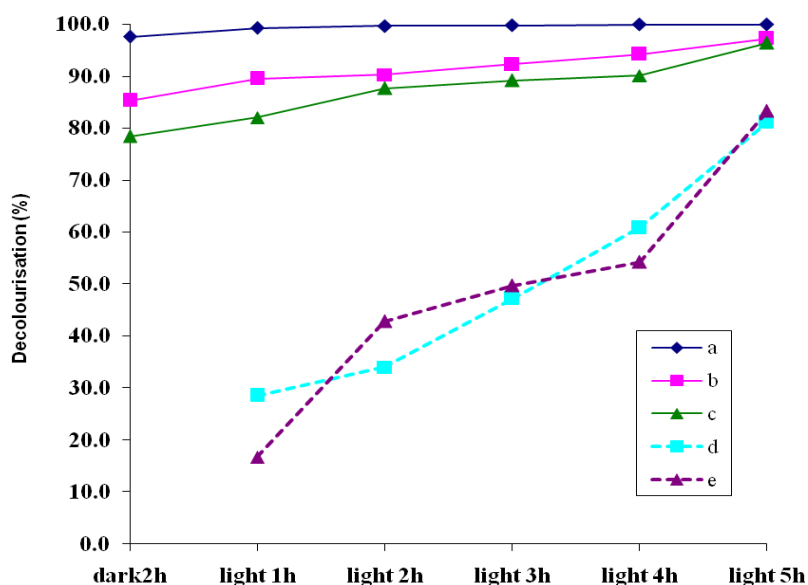


**Figure 4-4: Recyclability with removal of adsorbed MB : (a) MB + 0.5g/L Yamor-pH2, (b) 1st reuse, (c) 2nd reuse, (d) photoactivity after correcting for absorption of 1st reuse, (e) photoactivity after correcting for absorption of 2nd reuse.**

The second way of recyclability testing was performed by readding 200 mL  $1 \times 10^{-4}$ M MB without removal of adsorbed MB. The results are shown in Figure 4-5. The adsorption capacity significantly decreased in the first and second reuses as expected, 75% and 22%, respectively (Figure 4-5b, c), as MB was adsorbed 97% of  $1 \times 10^{-4}$ M MB in the preliminary photoactivity test before recycling (Figure 4-5a). The photodecolourisation of MB in the first reuse, including adsorption and photoactivity, was 85% in 4 hours and 99% in 24 hours (Figure 4-5b), while 51% and 95%, respectively, in the second reuse (Figure 4-5c). However, considering only the

photoactivity, the percentage of bleaching of MB under visible light irradiation can be about 40% in 5 hours and more than 90% in 24 hours both in the first and second recycles (Figure 4-5d, e). These results show the reusability of Yamor-pH2. As mentioned above about the gradual colour changing of Yamor-pH2 from yellow to pale yellow after irradiation, it was found that it remained pale yellow and can be a visible- light-driven photocatalyst even on prolonged irradiation, although the reaction rate decreased. The color change probably due to some  $\eta^2$ -peroxide being converted to a hydroxide form upon photoirradiation . The intense yellow can be recovered after further addition of  $H_2O_2$ . For this reason, Yamor-pH2 can be reused several times with addition of  $H_2O_2$ .

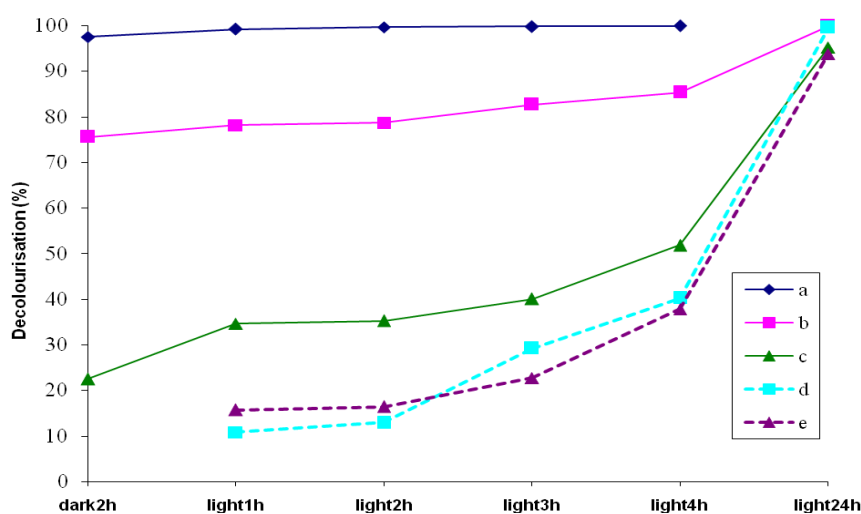


**Figure 4-5 : Recyclability without removal of adsorbed MB : (a) MB + 0.5 g/L Yamor-pH2, (b) 1st reuse, (c) 2nd reuse, (d) photoactivity after correcting for absorption of 1st reuse, (e) photoactivity after correcting for absorption of 2nd reuse.**

## 4.2 Yellow crystalline TiO<sub>2</sub>

As surface area, crystallinity, phase content, dopants and photon energy have been reported as the major factors affecting activity of a photocatalyst, comparison of various temperatures, various phase contents, various loading elements or dopants and various types of light have been performed.

### 4.2.1 Effect of calcination temperature

It was found that samples calcined at 600 °C (surface area ~ 44 m<sup>2</sup>/g) exhibits high activity under visible light around 90% decolouration with 25% MB adsorption . No activity was found under dark condition with a little increase in concentration of MB was observed, perhaps due to evaporation of aqueous solution. 15% of decolourisation of MB without photocatalyst were found, probably because there is a small overlap energy of emitting wavelength of lamp and absorption spectrum of MB which might lead to some photolysis. As prepared powder exhibits a limited photoactivity, around 25 % and adsorbs a small amount of MB, possibly due to amorphous character e.g. pores might not be available resulting in less adsorption. In addition, around 48% activity was obtained from a sample calcined at 900 °C (surface area ~ 2.5 m<sup>2</sup>/g), which is less than for the 600 °C sample in spite of the 900°C sample absorbing more visible in UV-Vis diffuse reflectance.

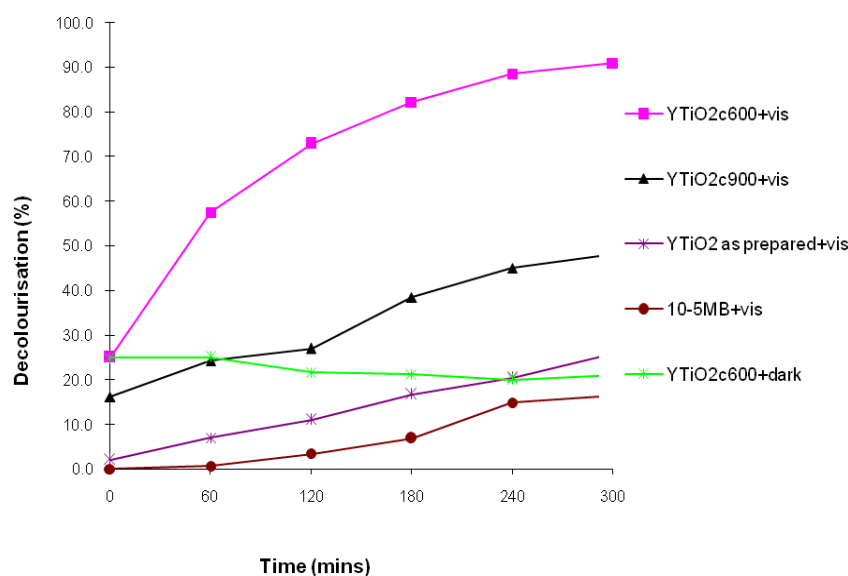


**Figure 4-6 : Photodecolourisation of MB comparing yellow TiO<sub>2</sub> samples calcined at various temperatures, including control experiments (1x10<sup>-5</sup> M MB + light, yellow TiO<sub>2</sub> + MB + dark).**

Thus yellow TiO<sub>2</sub> exhibits an interesting property of being photoactive under visible light. The best photocatalytic performance was observed for 600 °C calcination, probably reflecting a compromise between red shift and surface area with changing temperature.

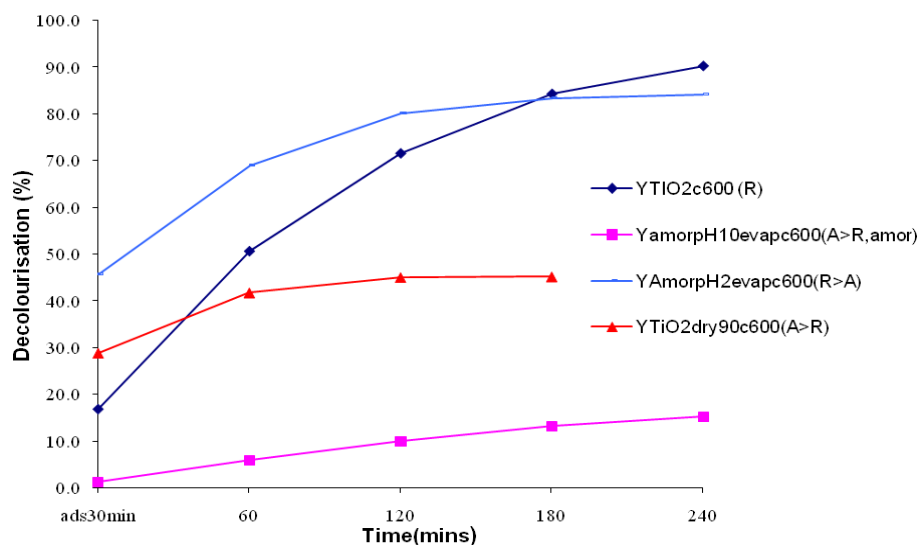
Since yellow TiO<sub>2</sub> calcined at 600 °C exhibits a high performance without charge separation, yellow TiO<sub>2</sub> itself might behave as charge separator. One possibility is that residual amorphous material on the surface as can be observed from TEM images as in a crystalline-amorphous core shell might enable charge separation. Photogenerated electrons might transfer to the amorphous region resulting in less electron hole recombination. The photogenerated holes are then active enough to produce hydroxyl radical and decompose methylene blue effectively. Crystalline-amorphous core shell

structure has been reported in enhancement of activity in lithium ion battery<sup>158</sup> and photovoltaic.<sup>159,160</sup>

#### 4.2.2 Effect of phase content

The influence of phase content of TiO<sub>2</sub> to photoactivity has been widely investigated. Anatase is believed to have higher photoactivity than rutile, however, Degussa P25, well known for high photoactivity TiO<sub>2</sub>, is a mixture of 80% anatase : 20% rutile. Mixed phase with major phase of anatase leading to a higher photoactivity has been reported.<sup>161,162</sup> Nevertheless, some work reported that rutile is as good or better than anatase as in some case.<sup>163,164</sup>

Previously, research on the effect of phase content on photoactivity has usually been studied in UV light, there has not been much studied under visible light. Since our rutile yellow TiO<sub>2</sub> can be prepared at low temperature and as discussed earlier conditions controlled during synthesis can induce some anatase, so that it is a good opportunity to investigate this issue under visible light. Mixed phase yellow TiO<sub>2</sub> powders were prepared by using same starting materials but different combustion condition. Yellow major phase of anatase 67% A : 33% R was obtained by drying evaporated acidic solution at 90 °C, brown yellow 67%A : 33% R and some amorphous character was obtained by evaporating yellow amorphous pH10 and pale yellow 14% A : 86% R was obtained by evaporating yellow amorphous pH2. It was figured out that the anatase phase might be induced on milder combustion as drying at low temperature or basic condition both affect a milder combustion.



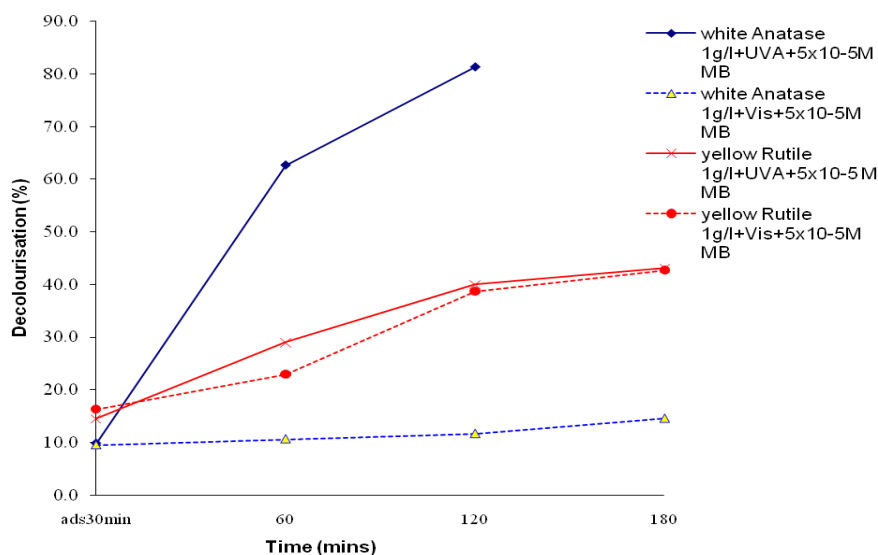
**Figure 4-7 : Photodecolourisation of MB comparing different phase content of yellow TiO<sub>2</sub> powders.**

Figure 4-7 shows a photodecolourisation of MB comparing different phase contents of yellow TiO<sub>2</sub> powders after calcining at 600 °C. Comparison of adsorption capacity among these samples, evaporated Yamor-pH2 has the highest adsorption, consistent with a surface area of 291.16 m<sup>2</sup>/g after calcination at 600 °C. Lower drying temperature of yellow TiO<sub>2</sub> adsorbed more MB than lower surface area of 150 °C drying temperature. Evaporated Yamor-pH10 is the lowest in terms of adsorption despite higher amorphous character compared with others. It is notable that the adsorption behaviour of amorphous character in Yamor-pH10 is similar to as prepared yellow TiO<sub>2</sub> dried 150 °C, probably amorphous character by this method is different from non crystalline powder in terms of compactness or porosity. Surface areas of Yamor-pH10 and as prepared yellow TiO<sub>2</sub> dried 150 °C after calcining at 600 °C are 22.14 and 43.49 m<sup>2</sup>/g, respectively.

Photoactivity after subtracting adsorption capacity shows a higher activity of rutile phase than anatase phase as can be seen that 100% rutile phase yellow TiO<sub>2</sub> dried 150 °C and 86% rutile phase evaporated Yamor-pH2 are significantly better than anatase major phase of other two samples. It may be concluded that for these yellow phases, rutile is more active than anatase under visible light.

#### 4.2.3 Effect of colour on visible light photoactivity

In order to assure that yellow colour has benefit to photoactivity under visible light, pure white anatase was compared with yellow rutile TiO<sub>2</sub> under both UVA and visible light as shown in figure 4-8. White anatase was obtained by calcination of Yamor-pH2 at 600 °C. As white anatase is expected to be quite active under UVA and will completely remove  $1 \times 10^{-5}$  M MB in just a short period, increasing concentration of MB to  $5 \times 10^{-5}$  M was chosen in this investigation. Anatase TiO<sub>2</sub> is quite active under UVA, it can remove about 85% MB in 2 hours, while is almost inactive under visible light. Photoactivity of yellow TiO<sub>2</sub> calcined 600 °C under UVA is a bit better than under visible light, around 40% of MB is decolourised in 3 hours. The results show that extending of absorption edge into visible region has a beneficial effect to visible light photoactivity of TiO<sub>2</sub>.



**Figure 4-8 : Photodecolourisation of MB comparing between white anatase TiO<sub>2</sub> and yellow rutile TiO<sub>2</sub>.**

#### 4.2.4 Effect of dopants or loading elements

In order to improve performance of a photocatalyst, doping or loading with impurity is used to enable charge separation. Numerous works have reported the advantages of doping or loading small amounts of other elements e.g. metal ion, anion, metal on the improvement of photoactivity by acting as an charge separator inhibiting a recombination of photogenerated electrons and phogenerated holes. On the other hand, considerable amount of work reports some drawback of doping or loading that may act as charge carrier trapping as well. Amount of impurity, synthetic method, surface area, surface properties and compatibility between photocatalyst and dopants need to be taken into account.<sup>38,45,72,127</sup>

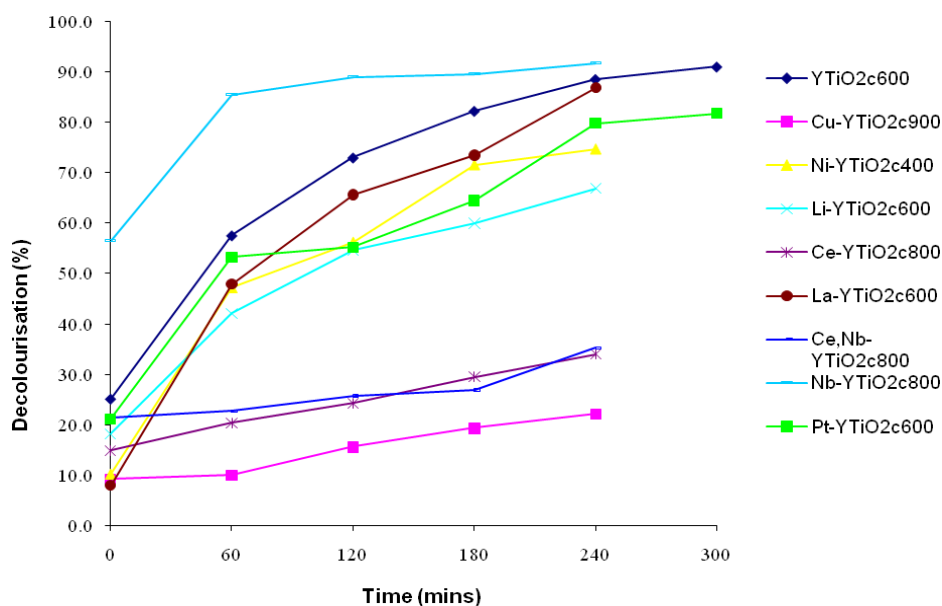


**Figure 4-9 : Photodecolourisation of MB by various doping or loading elements yellow TiO<sub>2</sub>.**

Ce, Cu, Nb, Fe, Li and La were chosen as dopants or loading elements in this work as it has been reported that these can enhance photoactivity of TiO<sub>2</sub>. Results are shown in figure 4-9.

Physical properties of yellow TiO<sub>2</sub> such as phase content, surface area and colour after adding impurities vary depending upon dopants or loading elements as summarised in table 3-1, probably due to nature of impurities or combustion conditions.

Ni - yellow TiO<sub>2</sub> is green while Nb-yellow TiO<sub>2</sub> and Zn - yellow TiO<sub>2</sub> are still yellow. Ni, Zn and Nb induced anatase phase for 24%, 55%, 71% respectively, probably due to a mild combustion reactions as lots of bubbling can be seen during drying. However, there is no correlation between colour and phase content because yellow can be obtained from both pure rutile phase and mixed phase, on the other

hand, various colours appear in both pure rutile phase and mixed phase. Colour might be influenced by defect disorder from impurities, nature of dopant and its oxidation state, and calcination temperature. Cu doped yellow TiO<sub>2</sub> is pale orange at 400 °C but turns to grey at 900 °C even in the same rutile phase.

Photoactivity of the Cu-yellow TiO<sub>2</sub> calcined 900 °C, Ce-yellow TiO<sub>2</sub> calcined 800 °C and Ce,Nb-yellow TiO<sub>2</sub> calcined 800 °C are quite low, less than 40% in 4 hours, possibly due to higher calcination temperature, and lower surface area consequently. These three samples were calcined at higher temperature because dominant amorphous character was still existed at 600 °C. Cerium impurity in our yellow TiO<sub>2</sub> might diminish photoactivity of yellow TiO<sub>2</sub> as can be observed when comparing among Ce-yellow TiO<sub>2</sub> calcined 800 °C, Nb-yellow TiO<sub>2</sub> calcined 800 °C and Ce,Nb-yellow TiO<sub>2</sub> calcined 800 °C. It was found that Nb-yellow TiO<sub>2</sub> calcined 800 °C is much better than Ce-yellow TiO<sub>2</sub> calcined 800 °C and Ce,Nb-yellow TiO<sub>2</sub> calcined 800 °C is in between in terms of adsorption but photoactivity after 4 hours is quite close to Ce-yellow TiO<sub>2</sub> calcined 800 °C. It is notable that almost half of the activity of Nb-yellow TiO<sub>2</sub> calcined 800 °C comes from adsorption, around 30% more than naked yellow TiO<sub>2</sub> calcined 600 °C, and Ce,Nb-yellow TiO<sub>2</sub> calcined 800 °C has a bit more adsorption capacity than Ce-yellow TiO<sub>2</sub> calcined 800 °C. It might be said that Nb impurity is helpful to adsorption, in accord with previous work on TiO<sub>2</sub>.<sup>165</sup>

La-yellow TiO<sub>2</sub> calcined 600 °C, Li-yellow TiO<sub>2</sub> calcined 600 °C and Ni-yellow TiO<sub>2</sub> calcined 400 °C slightly inhibit performance of yellow TiO<sub>2</sub> calcined 600 °C. However, regarding the adsorption capacity comparing to activity after 4 hours, La-

yellow TiO<sub>2</sub> calcined 600 °C has highest photoactivity, higher than naked yellow TiO<sub>2</sub> calcined 600 °C.

Doping or loading impurities into yellow TiO<sub>2</sub> prepared by this method does not enhance overall activity but improved adsorption capacity in the case of niobium impurity and enhanced photoactivity by lanthanum impurity.

Loading metals such as Pt, Pd and Ag on the surface has been widely used in reducing electron hole pair recombination of photocatalysts. Photodeposition of H<sub>2</sub>PtCl<sub>6</sub> was used for loading 1 mol% Pt onto the surface of yellow TiO<sub>2</sub> calcined 600 °C. The yellow colour of yellow TiO<sub>2</sub> calcined 600 °C turns to grey after loading of Pt. Photoactivity of Pt-yellow TiO<sub>2</sub> calcined 600 °C is not increased as envisaged, slightly decreasing in both adsorption capacity and photoactivity in spite of the grey colour which might indicate more absorbed visible light. Pt loading might affect the character of amorphous shell, resulting in drop in photoactivity.

#### 4.2.5 Effect of photon energy

It has previously been found that some yellow TiO<sub>2</sub> prepared by cation or anion doping lost activity under UV light due to the recombination.<sup>166,167</sup> To validate this issue, we have compared photoactivity of our 600 °C calcined yellow TiO<sub>2</sub> under visible light, UVA light and both of UVA and visible light as shown in figure 4-10. Adsorption capacity is quite close, less than 5% in difference. Trend of photoactivity behavior of samples under various photon energies are similar. The yellow TiO<sub>2</sub> calcined 600 °C is quite good under visible light, almost 85% bleaching 1x10<sup>-5</sup>M MB is obtained in 4 hours. Around 5% photoactivity increase when measuring under UVA

and 10% under UVA+visible. UVA might accelerate the reaction in the beginning as faster photoactivity than under visible light was observed while visible light might assist in lasting activity as can be seen from the difference of photoactivity after 1 hour between UVA+visible and UVA. Additionally, the photoactivity of yellow TiO<sub>2</sub> calcined 600 °C under UVA is higher than a commercial rutile TiO<sub>2</sub> (Alfa Aesar) under UVA, which is quite close to yellow TiO<sub>2</sub> under visible light. As a result, it can be concluded that our yellow TiO<sub>2</sub> assists photoactivity under visible light and did not act as an electron hole pair recombination centre. It is important to note the activity in visible light was similar in magnitude to that in UVA, confirming the practicality of visible light photocatalysis at this yellow TiO<sub>2</sub>.

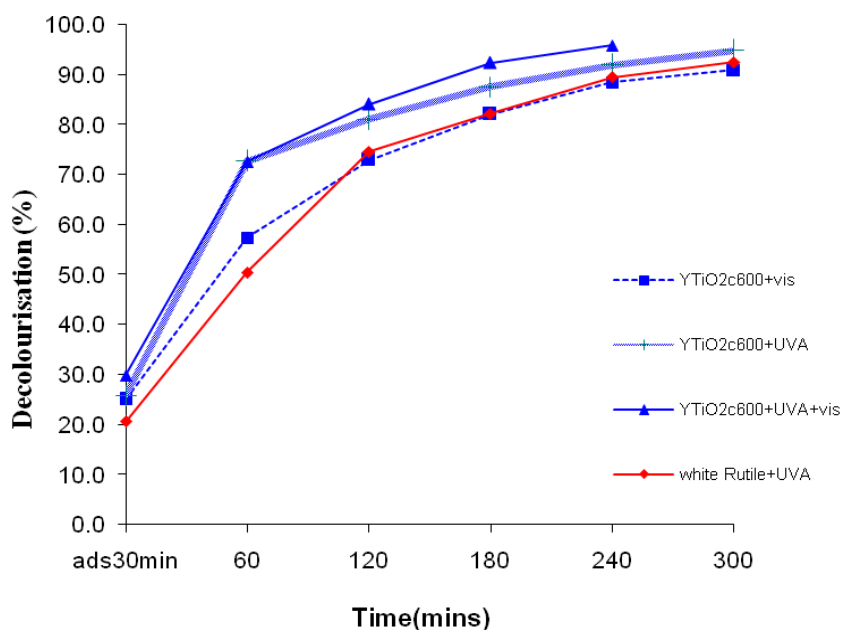


**Figure 4-10 : Photodecolourisation of MB by using yellow TiO<sub>2</sub> calcined 600 °C comparing visible, UVA and UVA+visible.**

#### 4.2.5 Effect of recyclability

Reuse of photocatalyst is also important issue in approaching a practical application. As solar energy consists of both UV and visible light, reuse and tolerance to UVA is measured simultaneously. Photoactivity was evaluated under visible light first and then recovering sample by filtering and removing adsorbed MB at 300 °C heat treatment, afterward, retesting under UVA light. A similar cycle was performed before retesting under visible light again and both UVA and visible light, respectively. The result is shown in figure 4-11. It was found that photoactivity of the yellow TiO<sub>2</sub> calcined at 600 °C for 10 hours under both UVA and visible light was still highest although it is the 4<sup>th</sup> use. The photoactivity under UVA was a bit higher than under visible light, which is quite similar for the first testing and the second testing.

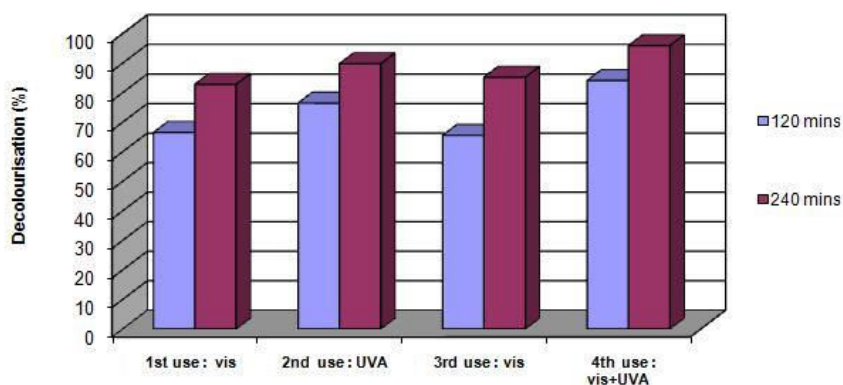


**Figure 4-11 : Recyclability of yellow TiO<sub>2</sub> calcined at 600 °C in photodecolourisation of MB.**

## CHAPTER 5

### Results and discussion on photocatalytic water splitting

The photocatalytic water splitting throughout this work was evaluated by suspending 0.1 g of TiO<sub>2</sub> in 200 mL of pure deionised water, or in 10% by volume of ethanol or in 0.025 molar of oxalic acid in the case of sacrificial agent investigation, in a gas tight box with headspace around 800 mL. The photoactivity was determined under anaerobic atmosphere (nitrogen) and under aerobic atmosphere (air) for comparison. Then illuminating the suspension from above with the high intensity discharge 250W iron doped metal halide UV bulb equipped with UV cutoff filter,  $\lambda \geq 420\text{nm}$ . The set up is shown in figure 2-9. The evolved gases were monitored by gas chromatography. The quantum yields (QY) or quantum efficiencies (QE) were calculated by the percentage of the number of reacted electrons to the number of incident photons, which determined by using ferrioxalate actinometer.

#### 5.1 Yellow amorphous TiO<sub>2</sub>

Amorphous or hydrated powder is generally assumed to have negligible photoactivity because of high recombination rate from defect disorder. Some research groups<sup>73,168</sup> have reported photoactivity of amorphous TiO<sub>2</sub> and other oxide compounds such as ZrO<sub>2</sub> and Nb<sub>2</sub>O<sub>5</sub>, which depends on synthetic method. It was found that amorphous Nb<sub>2</sub>O<sub>5</sub> prepared by solvothermal process has a higher photoactivity than crystalline Nb<sub>2</sub>O<sub>5</sub> in hydrogen production and mineralisation of acetic acid.<sup>168</sup> High photocatalytic rates for hydrogen production were also obtained by using hydrated

TiO<sub>2</sub> with methanol as sacrificial agent under UV light because of a higher density of active sites and reduced electron–hole recombination.<sup>73</sup>

Although Yamor-pH2 is active for photodecolourisation of MB, the conduction band edge position needs to be suitable for hydrogen production in order to split water into hydrogen and oxygen.

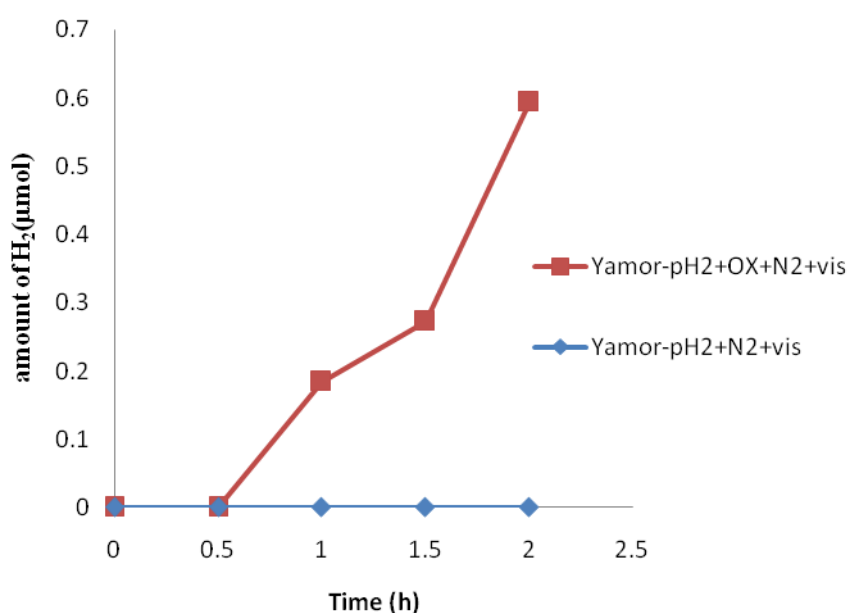


**Figure 5-1 : Hydrogen production from photocatalytic water splitting using yellow amorphous TiO<sub>2</sub> as photocatalyst with and without sacrificial agent.**

No hydrogen could be produced by using Yamor-pH2 as photocatalyst without any sacrificial agent while a small amount of hydrogen was found when adding oxalic acid as shown in figure 5-1. It is thought that the conduction band edge of Yamor-pH2 might not be appropriate for hydrogen production as there is a low recombination rate and a high photoactivity for CO<sub>2</sub> production from photooxidation of oxalic acid in figure 5-2.

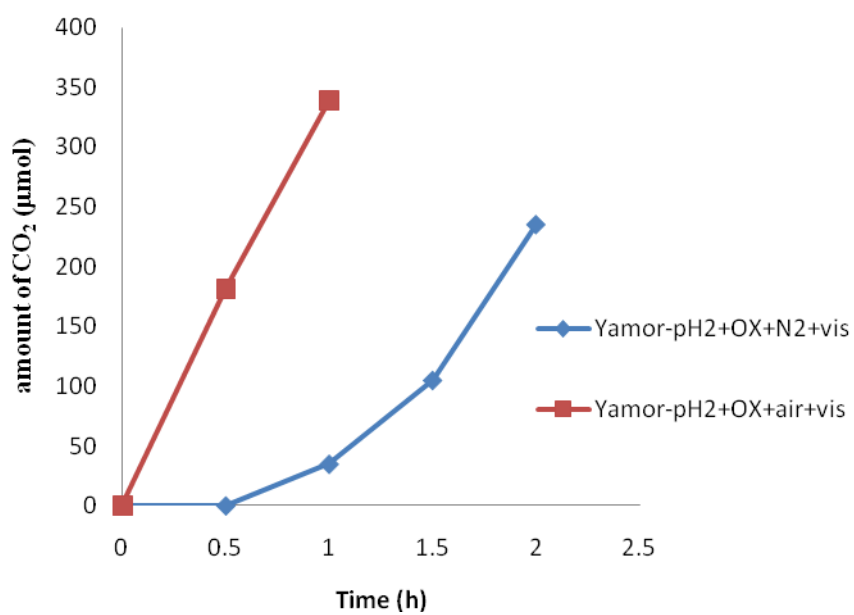


**Figure 5-2 : CO<sub>2</sub> production from photocatalytic water splitting using yellow amorphous TiO<sub>2</sub> as photocatalyst with oxalic acid as sacrificial agent.**

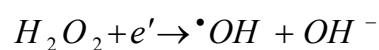
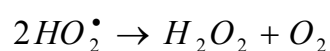
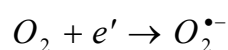
## 5.2 Yellow crystalline TiO<sub>2</sub>

In contrast to photooxidation in which the valence band plays an important role, the conduction band is a key factor for photoreduction. Hydrogen can be produced by photocatalytic water splitting at the conduction band. The conduction band edge should be higher or more negative than the hydrogen potential level,  $E_{H_2/H_2O}$ . Several materials have a suitable band gap energy and suitable potentials of the conduction band and the valence band edge under UV light. However, there are a few materials that can produce hydrogen from water splitting under visible light because the band gap is narrow and thus the conduction band is less negative than the hydrogen potential level. Band gap narrowing whilst keeping the conduction band edge in the right position is required for visible light photocatalytic water splitting. Apart from the potential of the conduction band edge, a high recombination rate also affects the photocatalytic water splitting. Separation of photogenerated electrons and photogenerated holes is also required. Charge separation may be achieved by adding sacrificial agents such as methanol, ethanol, oxalic acid, KI, EDTA to remove holes or loading charge separator e.g. Pt, Pd, Ag on the surface.<sup>30,32,112,171,172</sup>

Therefore, to investigate the photoactivity of yellow TiO<sub>2</sub> on photocatalytic water splitting, the effect of various parameters such as atmospheres, photon energy, sacrificial agents, doping or loading elements, have been studied.

### 5.2.1 Effect of atmosphere

Hydrogen production from photocatalytic water splitting has generally been studied under inert atmosphere or vacuum. It has rarely been reported under air atmosphere since oxygen will react with the photogenerated electrons instead of the hydrogen ion, resulting in less or negligible amount of hydrogen.



Hydrogen evolution in air was obtained directly by modifying a material with co-catalyst, as reported in case of  $Rh_{2-y}Cr_yO_3$  loaded  $(Ga_{1-x}Zn_x)(N_{1-x}O_x)$ .<sup>111</sup>

It would be interesting to see if the yellow  $TiO_2$  can produce hydrogen under air atmosphere and without any sacrificial agent because it might better reflect to a practical application.

Photocatalytic water splitting using yellow  $TiO_2$  calcined at  $600^\circ C$  as photocatalyst under visible light and without any sacrificial agent under various atmospheres is compared with a blank and white  $TiO_2$  in figure 5-3. No hydrogen was produced from the blank or from the white rutile  $TiO_2$  but the yellow  $TiO_2$  could produce hydrogen without any sacrificial agent or co-catalyst in anaerobic and even in aerobic conditions. A greater amount of hydrogen was produced under nitrogen atmosphere than under air atmosphere as expected.

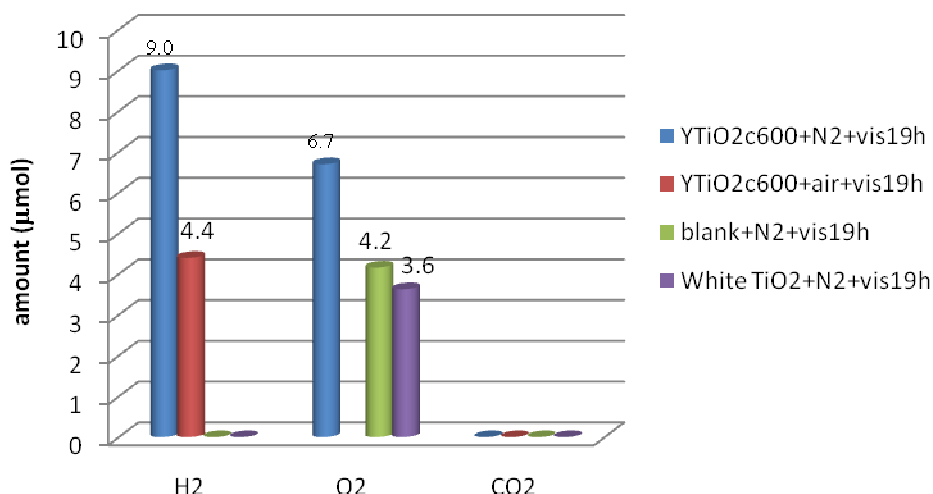


**Figure 5-3 : Photocatalytic water splitting using yellow TiO<sub>2</sub> calcined at 600°C as photocatalyst under visible light and without any sacrificial agent in various atmospheres compared with the blank and the white TiO<sub>2</sub>.**

It may be concluded that the band edge position of the conduction band of the yellow TiO<sub>2</sub> calcined at 600°C is high or negative enough to reduce the hydrogen ion. It is important to note that the recombination rate of photogenerated electron hole pairs in the yellow TiO<sub>2</sub> is not very high as hydrogen can be produced without any sacrificial agent or co-catalyst. The crystalline-amorphous core-shell structure and the difference of amount of Ti<sup>3+</sup> between around 50% on surface detected by XPS and 2% in bulk detected by SQUID magnetometer might be a key factor in providing charge separation. The crystalline-amorphous core-shell has previously been reported as a key factor. TiO<sub>2</sub> film coated electrodes in photoelectrochemical solar cells fabricated with a crystalline core of Degussa P25 and amorphous shell from hydrolysis of TiCl<sub>4</sub> solution at 100°C has been reported as a promising electrode owing to an improvement of electron injection from dye to amorphous phase.<sup>160</sup> Silicon crystalline-amorphous core-shell nanowire has been used as anode material for

lithium ion batteries by growing directly on the stainless steel current collector. A high charge storage capacity and high charging and discharging rates were reported.<sup>158</sup> The crystalline- amorphous core-shell of Ge nanoneedle arrays has been envisaged to provide a high efficiency in the photovoltaic and photodetector applications since it has a narrow band gap energy around 1 eV and exhibits high optical absorption efficiency.<sup>159</sup>

Considering rather similar amount of oxygen produced by the blank and the white TiO<sub>2</sub>, there may be some air remaining in the water after purging and evolved after temperature of the water increases by the heat from the lamp or there may be some air from a leak. According to slightly greater amount of the oxygen produced by using the yellow TiO<sub>2</sub> than the blank or the white TiO<sub>2</sub>, some oxygen might be obtained from water splitting. It may be proposed that the photoirradiation of the yellow TiO<sub>2</sub> calcined at 600°C can split water into hydrogen and oxygen. However, with the observation of a high level of background O<sub>2</sub> in the blank makes all the O<sub>2</sub> data in this work tentative at the least.

### 5.2.2 Effect of photon energy

As the yellow TiO<sub>2</sub> calcined at 600°C assists the photodecolourisation of MB under visible light and the activity was similar in a magnitude to that in UVA, the photoreduction was also performed. Hydrogen production using yellow TiO<sub>2</sub> calcined at 600°C under visible light, UVA and UVA+visible light is shown in figure 5-4. The results were similar to the photooxidation of MB in the case of UVA as the amount of

hydrogen under UVA was slightly higher than under visible light. However, a remarkably greater amount of hydrogen was produced under UVA+visible light, which is completely different from the slight increase in the photooxidation of MB. The increase of reaction rate in the case of UVA+visible light might be caused by the increase of temperature, around 10°C, since the temperature of the box was not precisely controlled. However, considering the oxygen production under visible > UVA > UVA+visible as shown in figure 5-5, UVA might affect the photocatalytic process as well.

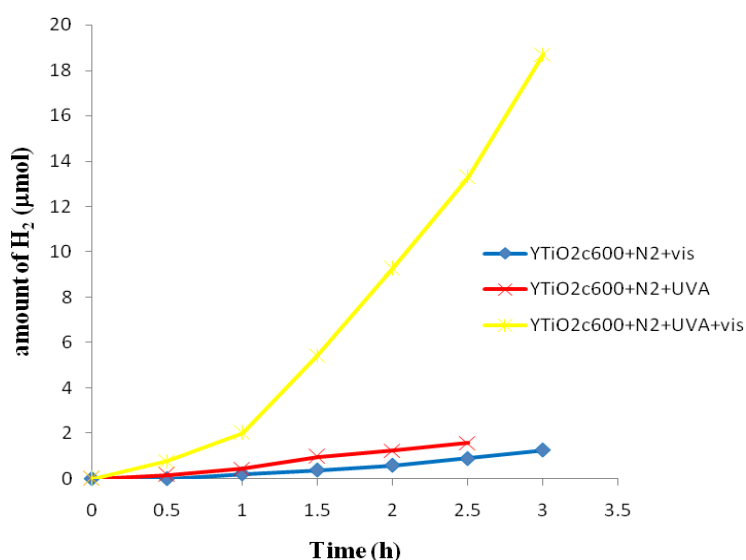


**Figure 5-4 : Hydrogen production by photocatalytic water splitting using yellow TiO<sub>2</sub> calcined at 600°C as photocatalyst comparing Vis, UVA and UVA+Vis.**

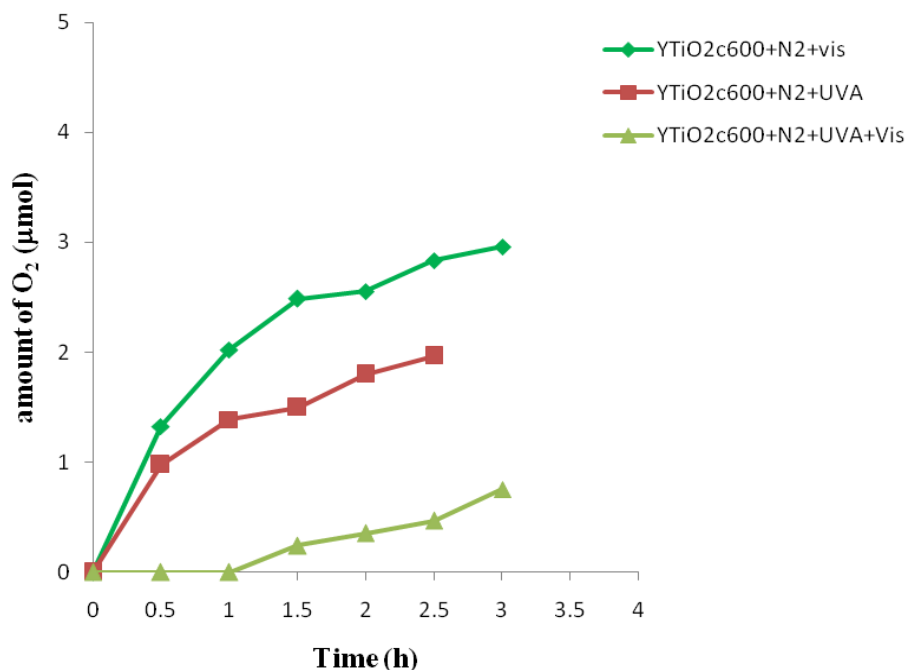


**Figure 5-5 : Oxygen production by photocatalytic water splitting using yellow TiO<sub>2</sub> calcined at 600°C as photocatalyst comparing Vis, UVA and UVA+Visible.**

### 5.2.3 Effect of sacrificial agent

Ethanol and oxalic acid were chosen as sacrificial agents because ethanol is widely used as a sacrificial agent in photocatalytic water splitting whereas oxalic acid is a kind of waste that can be used as sacrificial agent for the photoreduction and for the photooxidation by monitoring CO<sub>2</sub> evolution simultaneously.<sup>171</sup>

Alcohols such as ethanol and methanol have been widely reported as sacrificial agent<sup>30,32</sup> since its potential energy is higher than the valence band of TiO<sub>2</sub>. Therefore, the photogenerated holes can be separated from the photogenerated electrons by reacting with electrons from the alcohol. Methanol is reported to be a good electron

donor for hydrogen production.<sup>30,112</sup> Decomposition of alcohol will occur as it is a sacrificial agent. CO<sub>2</sub> is usually the main product from the reaction of alcohol with the photogenerated holes.<sup>160,169</sup> Other intermediates might be found as well such as methane, CH<sub>3</sub>COO and HCOO from the dissociation of -CH<sub>3</sub> and -CH<sub>2</sub>O- on the surface of TiO<sub>2</sub>, i.e. acetaldehyde and formaldehyde. It has been reported that the oxidation of ethanol will not occur in the dark condition or from thermal activity below 100°C. However, CO<sub>2</sub> produced by using alcohol as a sacrificial agent may not be detected since the photoreduction of hydrogen is generally performed in anaerobic condition in order to remove the effect of oxygen at the conduction band.<sup>32,73,140,169,170</sup>

Oxalic acid has been used as a probe for the photooxidation and sacrificial agent for the photoreduction. Use as a sacrificial agent, pH of oxalic solution should be adjusted to around 3 since the dissociation of oxalic acid occurs with pK<sub>1</sub>=1.25 and pK<sub>2</sub>=4.28. At pH 3.5 the fraction of oxalic acid present as HC<sub>2</sub>O<sub>4</sub><sup>-</sup> is more than 85%.<sup>171,172</sup> The photocatalytic hydrogen production using Pt-TiO<sub>2</sub> and oxalic acid as sacrificial agent has a higher evolution rate at pH 2-4 since oxalic acid is mostly in the form of HC<sub>2</sub>O<sub>4</sub><sup>-</sup>.<sup>171,173</sup>

CO<sub>2</sub>, CO, H<sub>2</sub>O, and HCOOH will be the products from the decomposition of oxalic acid, CO<sub>2</sub> + HCOOH were produced first and then HCOOH decomposed to CO and H<sub>2</sub>O.<sup>174</sup> Comparing H<sub>2</sub>C<sub>2</sub>O<sub>4</sub>, HCOOH and HCHO as sacrificial agents for the photocatalytic hydrogen production using Pt-TiO<sub>2</sub> suspension, the efficiency of H<sub>2</sub>C<sub>2</sub>O<sub>4</sub> > HCOOH > HCHO, which is consistent with the adsorption affinity of the electron donors on TiO<sub>2</sub>. Oxalic acid is a bidentate ligand and adsorbs on TiO<sub>2</sub> surface as a chelating binding. The adsorption is then stronger than formic acid, which occurs

as a bridging linkage. As a result, the electron transfer might be more efficient.<sup>175</sup> In the absence of photocatalyst and light source, neither mineralisation of the parent oxalic acid nor its dissociated ions could be detected.<sup>176</sup>

As MB might not suitable as a probe molecules for monitoring the photoactivity under visible light due to the photoabsorption, monitoring CO<sub>2</sub> production from the decomposition of oxalic acid would be helpful to confirm the photooxidation of the yellow TiO<sub>2</sub>. It is of interest to combine the photocatalytic hydrogen production with the destruction of pollutants. A 10% by volume of ethanol and 0.025 molar of oxalic acid, pH of aqueous solution around 2-3, were used throughout the experiments.

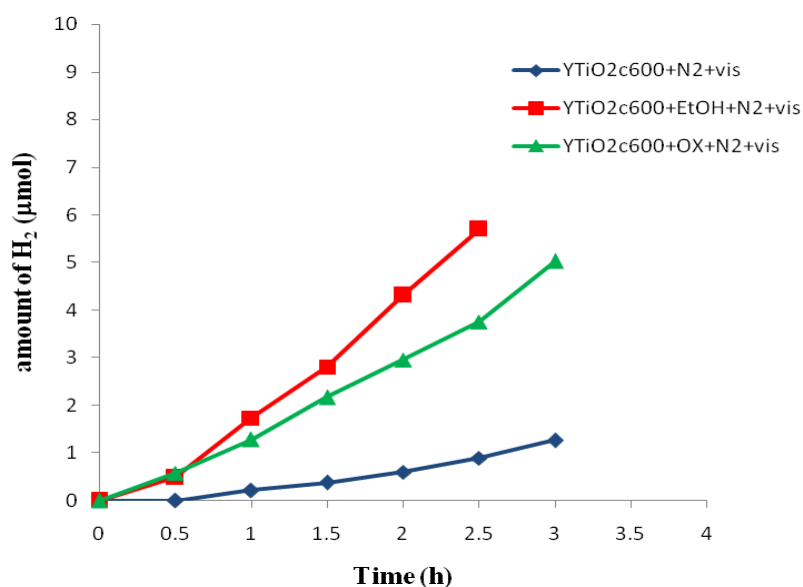


**Figure 5-6 : Hydrogen production from the photocatalytic water splitting using yellow TiO<sub>2</sub> calcined at 600°C as photocatalyst comparing ethanol and oxalic acid as sacrificial agents.**

The amount of hydrogen produced by photocatalytic water splitting comparing between using oxalic acid and ethanol as sacrificial agent is shown in figure 5-6. It

can be seen that the sacrificial agents were useful in the process as the amount of hydrogen is higher than without sacrificial agents. Ethanol was better than oxalic acid in terms of hydrogen production using yellow  $\text{TiO}_2$  calcined at  $600^\circ\text{C}$  as photocatalyst. The values is comparable to other materials.<sup>27,37</sup> The recombination rate in the case of using ethanol as sacrificial agent might be less than oxalic acid because the photogenerated holes were removed more rapidly by reacting with the donor electron and less oxygen was obtained consequently. Figure 5-7 shows the amount of oxygen produced when using ethanol and oxalic acid as sacrificial agent compared to without sacrificial agent. The results were consistent with the hydrogen production as a lower amount of oxygen was obtained when using ethanol than using oxalic acid and without sacrificial agents.

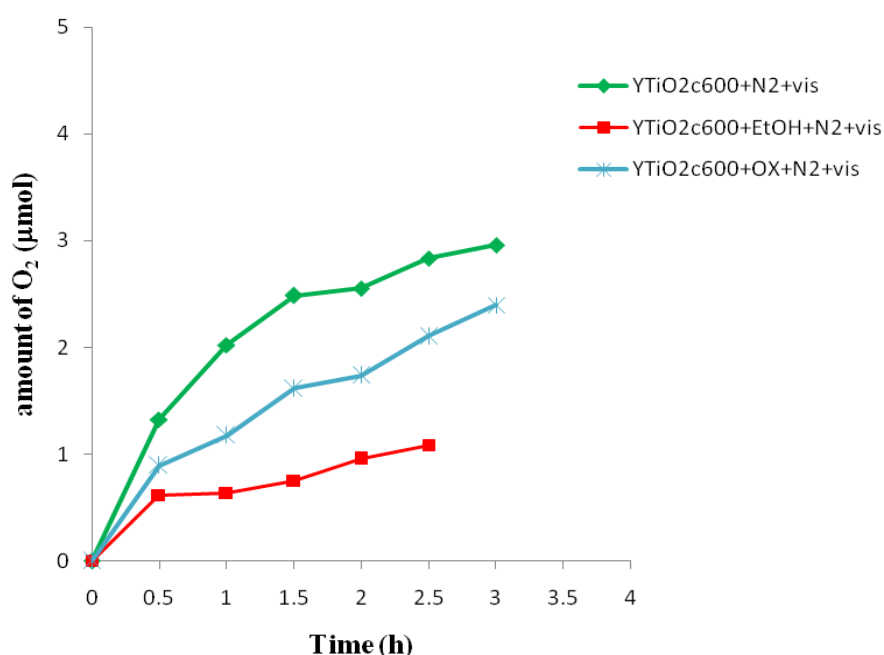


**Figure 5-7 : Oxygen production by photocatalytic water splitting using yellow  $\text{TiO}_2$  calcined at  $600^\circ\text{C}$  as photocatalyst comparing ethanol and oxalic acid as sacrificial agents.**

Investigation of the photooxidation of oxalic acid comparing between under air and under nitrogen atmosphere might be helpful for the confirmation of the effect of atmosphere because the greater amount of hydrogen can be observed under nitrogen atmosphere while the greater amount of CO<sub>2</sub> production can be observed under air atmosphere. Considerably less amount of hydrogen under air than under nitrogen when using oxalic acid as a sacrificial agent is observed in figure 5-8 confirming the effect of atmosphere as expected. Additionally, the effect of oxalic acid was also confirmed to assist the hydrogen production because a higher amount of hydrogen was obtained than without oxalic acid.

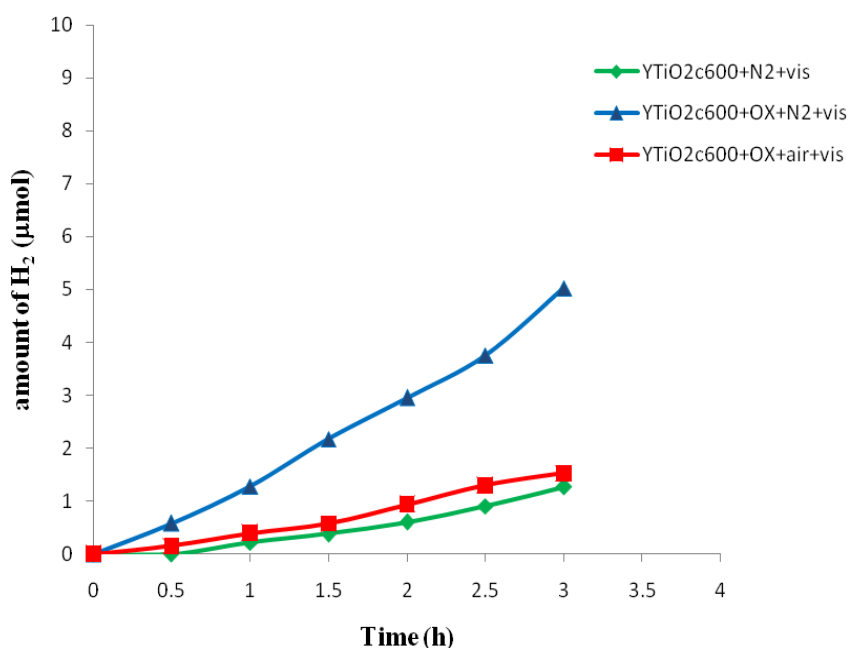


**Figure 5-8 : Hydrogen production by photocatalytic water splitting using yellow TiO<sub>2</sub> calcined at 600°C as photocatalyst and oxalic acid as sacrificial agent comparing between aerobic and anaerobic conditions.**

Decomposition of oxalic acid to CO<sub>2</sub> was achieved by photocatalytic process using yellow TiO<sub>2</sub> calcined at 600°C as photocatalyst. The amount of CO<sub>2</sub> was completely different when measuring under air and under nitrogen atmosphere as shown in figure 5-9. The oxygen in air would react with the photogenerated electrons and produces more hydroxyl radical, which plays an important role in the photooxidation (Figure 1-11). As a result, less amount of hydrogen and greater amount of CO<sub>2</sub> were obtained under air atmosphere.

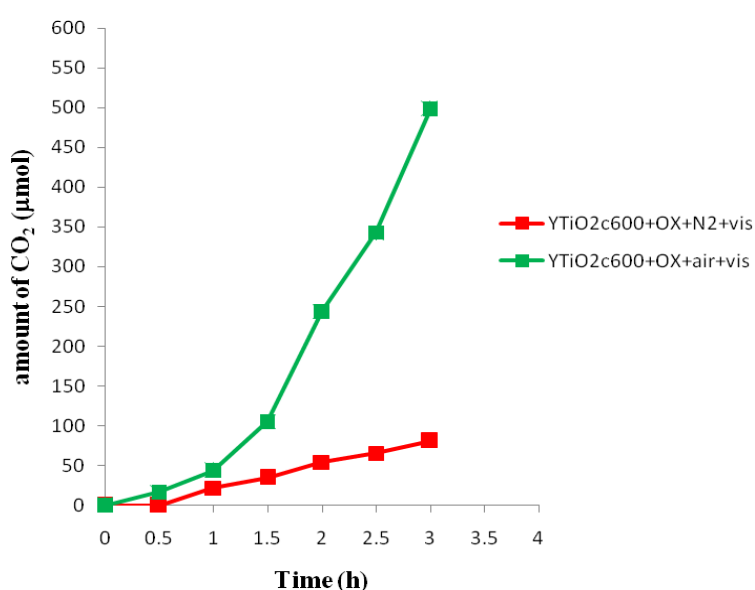


**Figure 5-9 : CO<sub>2</sub> production from the photocatalytic water splitting using yellow TiO<sub>2</sub> calcined at 600°C as photocatalyst and oxalic acid as sacrificial agent comparing aerobic and anaerobic conditions.**

In order to clearly see the effect of sacrificial agent, photoirradiation for 19 hours was performed as shown in figure 5-10. A comparison of the amount of hydrogen, oxygen and carbon dioxide were revealed under various conditions : without sacrificial agent under nitrogen atmosphere, with oxalic acid under nitrogen atmosphere and with ethanol under air atmosphere. The amount of hydrogen obtained by using oxalic acid as sacrificial agent under nitrogen atmosphere was 5 times greater than without

sacrificial agent, whereas the amount of hydrogen between without sacrificial agent and with ethanol under air was comparable. The oxygen produced without sacrificial agent was higher than with oxalic acid and in the blank, indicating that some oxygen was partly from the water splitting. CO<sub>2</sub> production from ethanol under air atmosphere, owing to the decomposition of ethanol, was also observed.

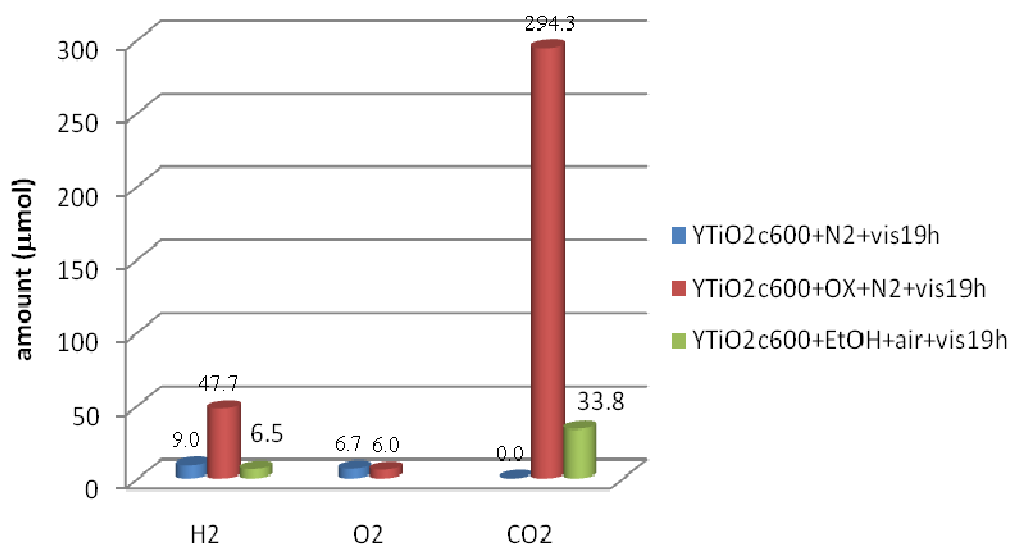


**Figure 5-10 : Photocatalytic water splitting using yellow TiO<sub>2</sub> calcined at 600°C as photocatalyst at various conditions.**

#### 5.2.4 Effect of calcination temperature

As the yellow TiO<sub>2</sub> calcined at 900°C exhibits some photoactivity on the decolourisation of MB, photoreduction was also investigated. However, it was found that no hydrogen can be produced when using the yellow TiO<sub>2</sub> calcined at 900°C, probably due to the change of the band edge position of the conduction band to be lower or more positive than hydrogen potential level. Figure 5-11 shows the

schematic representation of the band model of  $\text{TiO}_2$ . It can be seen that the presence of oxygen vacancy and titanium interstitials defect disorders leading to a lowering of the available electron energies near the conduction band edge, consistent with the oxygen vacancy of the yellow  $\text{TiO}_2$  calcined at  $900^\circ\text{C}$  detected by ESR.

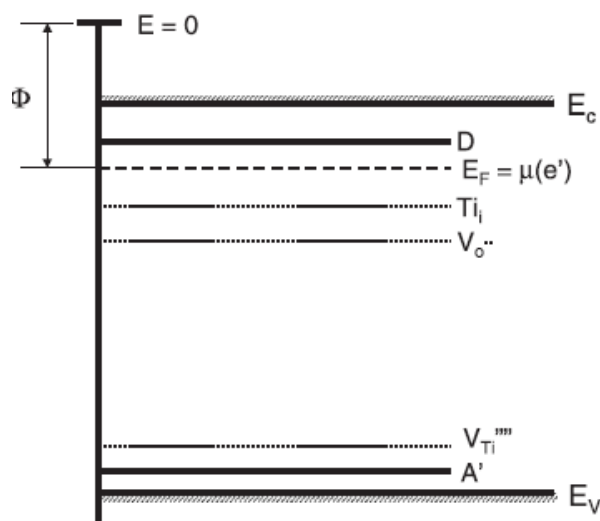


**Figure 5-11 : Schematic representation of the band model of  $\text{TiO}_2$  (reproduced from [177]).**

### 5.2.5 Effect of phase content

No hydrogen was detected from the mixed phase powders, yellow 67% A : 33% R prepared by drying evaporated acidic solution at  $90^\circ\text{C}$ , brown yellow 67%A : 33% R and some amorphous character obtained by evaporating yellow amorphous pH10 and pale yellow 14% A : 86% R obtained by evaporating yellow amorphous pH2, possibly due to the milder combustion leading to a substantial recombination rate of the photogenerated electron hole pairs as can be seen from the low photoactivity of the photodecolourisation of MB.

### 5.2.5 Effect of doping or loading elements

Doped or loaded yellow TiO<sub>2</sub> was not helpful for photocatalytic water splitting since no hydrogen could be detected as well as did not improve the photoactivity of the photodecolourisation of MB. A high recombination rate and/or the inappropriate of the band edge position of the conduction band might be caused by the increase in potential energy level of the impurities between the valence band and the conduction band. A redox reaction between doped or loaded elements with Ti<sup>3+</sup> might change the available electron energies in the yellow TiO<sub>2</sub>.

### 5.2.6 Effect of Pt loading

Platinum loading was generally found to improve the photoactivity around 3-5 times.<sup>73</sup> Platinum is a promising co-catalyst for hydrogen production.<sup>75</sup> Pt loaded yellow TiO<sub>2</sub> calcined at 600°C was prepared by photodeposition method. As yellow TiO<sub>2</sub> could produce hydrogen without any sacrificial agent, Pt loading was first performed under nitrogen atmosphere without any sacrificial agent. However, no hydrogen could be observed after photoirradiation for 3 hours. Then, ethanol was added as sacrificial agent and some hydrogen can be found as shown in figure 5-12. The amount of hydrogen was much less than unloaded yellow TiO<sub>2</sub> in ethanol solution under nitrogen atmosphere. Pt loading might not be helpful in producing hydrogen using yellow TiO<sub>2</sub> as photocatalyst.

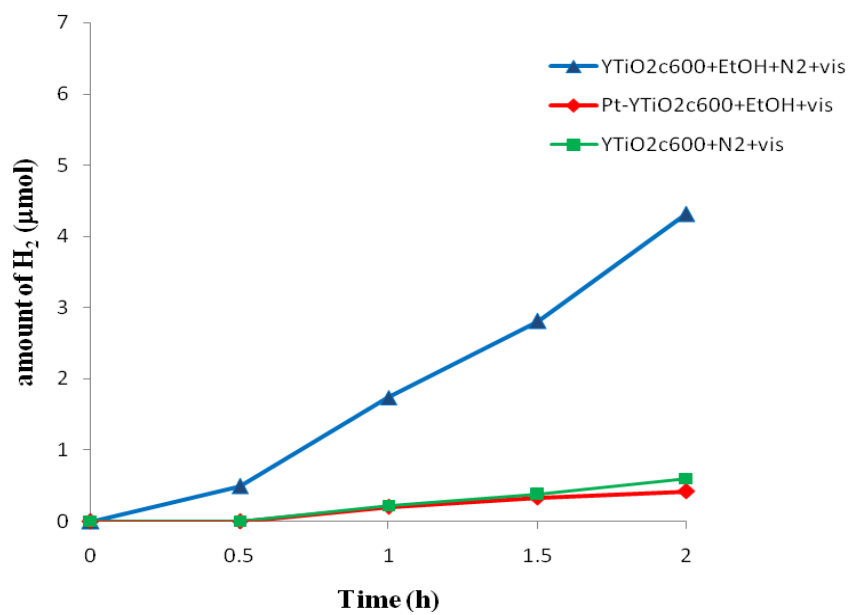


**Figure 5-12 : Hydrogen production by photocatalytic water splitting comparing unloaded and Pt loaded yellow TiO<sub>2</sub> calcined at 600°C as photocatalyst.**

## 5.3 Efficiency

### 5.3.1 Photon flux

Ferrioxalate actinometer was used to determine a photon flux entering into a box. A 0.006 M solution and the difference of the absorbance at 510 nm were examined. The photon flux was calculated and shown in table 5-1.

Wavelength (nm)	Photon flux (Einstein/s)	Photon flux (Einstein/h)
>350 (UVA+visible)	0.000000938	0.003376
>420 (visible)	0.000000731	0.002633

**Table 5-1 Photon flux entering into the box obtained by irradiation of 250 watts iron doped metal halide lamp with different filters.**

The photon flux obtained by our box is comparable to the value from the previous work,  $1.67 \times 10^{-7}$  Einstein/s, that used the same kind and power of lamp but irradiates from the side and use 45 mL cylindrical quartz vessel.<sup>178</sup> The value of the photon flux varies depend on type and power of the bulb, shape of the reactor, direction of illumination, path length between lamp and reactor, for instance, the photon flux of  $1.52 \times 10^{-8}$  einstein/s was obtained from a side illumination of 4 x 4 watts black light to a glass optical cell (1.0 cm×1.0 cm×4.0 cm),<sup>156</sup>  $8.33 \times 10^{-7}$  einstein/s was obtained from the full light high pressure 1000 watts mercury lamp to 250 ml beaker<sup>74</sup> and  $2.4 \times 10^{-8}$  einstein/s was obtained from 8 watts blacklight inside the 13.3 cm<sup>3</sup> tubular.<sup>169</sup>

However, the obtained photon flux values might not be exactly accurate as the photon flux under visible range too close to the photon flux under UVA+visible range in spite of the ferrioxalate actinometer just absorb wavelength range 250-500 nm, which is small proportion of emitting wavelength of the lamp in the visible range can be absorbed comparing to UVA+visible range.

### 5.3.2 Quantum efficiency

The quantum yields (QY) or quantum efficiencies (QE) were calculated by the percentage of the number of reacted electrons to the number of incident photons, which is 2 electrons for hydrogen production and 4 electrons for oxygen production.<sup>36,37,179</sup>

Therefore, the quantum efficiency can be calculated by mole of evolved gases as follows

$$QE = \frac{\text{The number of evolved } H_2 \text{ molecules} \times 2}{\text{The number of incident photons}} \times 100$$

$$QE = \frac{\text{The number of evolved } O_2 \text{ molecules} \times 4}{\text{The number of incident photons}} \times 100$$

	Visible		Visible+UVA		OX+Visible		EtOH+Visible	
	H <sub>2</sub>	O <sub>2</sub>						
<b>μmol/h</b>	0.42	0.39	6.23	0.25	1.67	0.79	2.28	0.43
<b>QE(%)</b>	0.032	0.058	0.37	0.03	0.12	0.12	0.17	0.07

**Table 5-2 Quantum efficiency of yellow TiO<sub>2</sub> calcined at 600°C after photoirradiation for 3 hours at various conditions.**

The Quantum efficiency shown in table 5-2 is a maximum values as the ferrioxalate actinometer just absorb wavelength range 250-500 nm. The maximum quantum efficiency obtained by using yellow TiO<sub>2</sub> as photocatalyst varies from 0.03 to 0.37 for hydrogen production and from 0.03 to 0.12 for oxygen production, depending on photon energy and sacrificial agents as shown in table 5-2. Photon energy is the most important factor determining quantum efficiency of hydrogen production, with around an order of magnitude increase when irradiating with UVA+visible light compared to irradiating with visible light. Sacrificial agents can improve the performance around 4-5 times over that without sacrificial agents.

In terms of charge balance it is important to compare hydrogen and oxygen yields, although the main focus of this study was to consider hydrogen production. Indeed there are much greater uncertainties in oxygen yields so we should focus upon charge balance in more qualitative terms. The amount of oxygen produced is not just from water splitting because some dissolved air also is released due to the increase in temperature on irradiation and in a few samples there was indication of a small air leak. The evolution of oxygen from the air remaining in the water of the blank experiments (water +N<sub>2</sub>+visible) is shown in table 5-3.

<b>Photoirradiation time (h)</b>	<b>Total of amount of oxygen (μmol)</b>
0.5	1.0 ± 0.2
1	1.6 ± 0.3
1.5, 2	1.7 ± 0.3
2.5, 3	1.8 ± 0.3

**Table 5-3 : the amount of oxygen from the air remaining in the water on irradiating with visible light.**

As can be seen from table 5-3 the uncertainty in oxygen production will be greatest at short times as the photoproduced oxygen will be expected to increase in proportion with time whereas the dissolved oxygen being released will increase much more slowly at longer times. It is therefore best to focus on longer periods utilised in considering oxygen efficiency. The values of oxygen from overall water splitting in table 5-2 are corrected for estimated values of oxygen evolved from solution due to heating under irradiation.

The quantum efficiency of hydrogen production is very low but comparable with other reports in the case of overall water splitting into hydrogen and oxygen gas under visible light. The efficiency of 0.0023 % and 0.66% have been reported when using platinum-loaded strontium titanate (Pt-SrTiO<sub>3</sub>) (core)-silica (shell) powder<sup>50</sup> and In<sub>1-x</sub>Ni<sub>x</sub>TaO<sub>4</sub> as catalysts.<sup>38</sup> Maeda et al,<sup>180</sup> achieved 0.14% quantum efficiency by using RuO<sub>2</sub> loaded GaN:ZnO as photocatalyst and it reached 2.5% when loaded yellow powder (Ga<sub>1-x</sub>Zn<sub>x</sub>)(N<sub>1-x</sub>O<sub>x</sub>) with nanoparticles of rhodium–chromium mixed oxide.<sup>181</sup>

## CHAPTER 6

### Conclusions

Photocatalytic water splitting is a promising process to produce hydrogen that may be used as a fuel for our energy future. Using water as a power source would be interesting in terms of producing an abundant and renewable source as well as consuming just light as an input energy of photocatalysis process. Furthermore, carbon dioxide free production by this process would be helpful for environmental issues of global warming and greenhouse effects due to carbon dioxide emission. However, carbon dioxide might be produced during synthesis of photocatalyst. Therefore, synthesis of photocatalyst without carbon precursor would be useful.

There are a number of materials active under UV light because most semiconductor materials can absorb UV light. Titanium compounds such as  $\text{TiO}_2$ ,  $\text{SrTiO}_3$ ,  $\text{CeTi}_2\text{O}_6$  have been proven as good photocatalysts, including layered perovskite compounds such as  $\text{Sr}_2(\text{Ta}_{1-x}\text{Nb}_x)_2\text{O}_7$ . However, much attention has been devoted to visible light driven photocatalysts recently for approaching to practical application of using sunlight, which consists about 45% visible light and just 5% of UV light. There are several compounds active under visible light, for example, sulphide compounds ( $\text{CdS}$ ,  $\text{AgGaS}_2$ ,  $\text{AgInZn}_7\text{S}_9$ ),  $\text{BiVO}_4$ ,  $\text{AgNbO}_3$ ,  $\text{CeCo}_{0.05}\text{Ti}_{0.95}\text{O}_{3.97}$ ,  $\text{Nd}_2\text{Zr}_2\text{O}_7$ ,  $\text{Sm}_2\text{Zr}_2\text{O}_7$ , red color of  $\text{Nb}_2\text{Zr}_6\text{O}_{17-x}\text{N}_x$  and modified UV active titanium compounds.

Titanium dioxide ( $\text{TiO}_2$ ) has been the most promising material in the fields of photocatalysis and solar energy conversion due to its activity, it being chemically and biologically inert, having strong oxidising power, cost-effectiveness, long-term

stability and environmentally friendliness. Additionally, the conduction band and the valence band edges are suitable for photocatalytic water splitting into hydrogen and oxygen.

Synthesis of visible light active TiO<sub>2</sub> by cation or anion doping, noble metal loading or nonstoichiometric TiO<sub>2</sub> have been successful recently. However, there are some restriction of these techniques such as using high temperature, complicated method, unstable at high temperature or at ambient temperature, low surface area and mostly using carbon compound as precursors, resulting in CO<sub>2</sub> emission.

Here we investigated a preparation of visible light active amorphous TiO<sub>2</sub> and high temperature stable yellow crystalline TiO<sub>2</sub> by CO<sub>2</sub> free, low cost and simple novel method. Titanium nitride as a precursor and peroxide based route were chosen. The peroxide based route without any organic solvent and chloride ion should be useful for synthesis of photocatalysts whereas TiN is an air and moisture stable compound. It is known that aqueous solutions of Ti(IV) and hydrogen peroxide give a peroxytitanato [Ti(OH)<sub>3</sub>O<sub>2</sub>]<sup>-</sup> ion, often called peroxytitanic acid. The mechanism of the peroxytitanic acid formation is very complex and still not completely understood. Clear red-brown solution of titanium peroxo species was obtained by dissolution of TiN in H<sub>2</sub>O<sub>2</sub> and HNO<sub>3</sub> acid at room temperature without stirring. The obtained precursor solution is stable for several days under ambient atmosphere. The resultant red- brown solution is then used as a titanium solution precursor for yellow amorphous and yellow crystalline TiO<sub>2</sub> synthesis. Yellow amorphous precipitate was formed after adjusting the pH of the solution to 2 by slowly adding ammonia solution with the constant stirring. The precipitate is filtered and washed with distilled water

several times. It was then dried at room temperature. Yellow crystalline powder was obtained after evaporation of the resultant red-brown solution at 90 °C and drying at 90 °C or 150 °C. Visible light photoactivity of the samples are evaluated by photooxidation of methylene blue and photoreduction of hydrogen from water splitting.

### **Yellow amorphous TiO<sub>2</sub>**

The BET surface area of yellow amorphous TiO<sub>2</sub>, Yamor-pH2, was 261 m<sup>2</sup>/g. It is interesting that intense yellow powders obtained at pH2 and using titanium nitride as precursor is quite stable, it can be kept in clear vial at ambient atmosphere for several months. It was found that Yamor-pH2 shows the red shift of the absorption edge into the visible region.

The Yamor-pH2 exhibits an interesting property of being both surface adsorbent and photoactive under visible light for photodecolourisation of aqueous solution of methylene blue by using a 250 W metal halide bulb equipped with UV cut-off filter ( $\lambda > 420$  nm) under aerobic condition. It was assigned to the  $\eta^2$ -peroxide, an active intermediate form of the addition of H<sub>2</sub>O<sub>2</sub> into crystalline TiO<sub>2</sub> photocatalyst. It might be concluded that an active intermediate form of titanium peroxo species in photocatalytic process can be synthesised and used as a visible light driven photocatalyst. Visible light photoactive in decolourising MB of Yamor-pH2 prepared by this method might prove of a low recombination of photogenerated electron hole pair. However, conduction band need to be suitable for hydrogen production level in

order to split water into hydrogen and oxygen. No hydrogen could be produced by using Yamor-pH2 as photocatalyst without sacrificial agent, while small amount of hydrogen was found when adding oxalic acid. It is thought that conduction band of Yamor-pH2 might not be appropriate for hydrogen production since low recombination rate would be occurred as can be seen from CO<sub>2</sub> production from photooxidation of oxalic acid.

### **Yellow crystalline TiO<sub>2</sub>**

It was found that a rutile phase TiO<sub>2</sub> without any anatase phase can be prepared at low temperature treatment by this method. An acid catalysed reaction is thought to favour the rutile phase because a yellow anatase-rutile mixture phase TiO<sub>2</sub> after calcination at 600 °C can be prepared by this method under basic condition. The reaction mechanism is thought to involve an acid catalysed combustion reaction between titanium peroxo species and NH<sub>4</sub>NO<sub>3</sub> because NH<sub>4</sub>NO<sub>3</sub> phase was found in the XRD pattern of as prepared powder before drying at 150 °C. Rutile phase tend to be formed at higher acidity and higher drying or ignition temperature. Nanoparticulate TiO<sub>2</sub> (~10 nm) can be seen from TEM images. The diffuse reflectance spectra of yellow TiO<sub>2</sub> sample shows a red shift of the absorption edge into the visible region compared with commercial rutile TiO<sub>2</sub> and the red shift of adsorption edge increases with the treatment temperature. The reflectance spectrum indicates that the direct band gap is not changed on doping with trap states being introduced into the band gap, the broad character is possibly indication of an indirect transition.

Yellow TiO<sub>2</sub> contained a paramagnetic species possessing a strong ESR spectrum at room temperature and pressure. A g value around 1.97 of Ti<sup>3+</sup> was obtained until 600 °C calcination while an electron trapped on an oxygen vacancy with signal at g~2.003 was observed at 900 °C and 1,200 °C. These g values differ from the g values and spectrum character of O<sub>2</sub><sup>-</sup>, O<sub>3</sub><sup>-</sup> and nitrogen species. Ti and O XPS data confirm the presence of Ti<sup>3+</sup> with an additional set of Ti. The Ti<sup>4+</sup> and Ti<sup>3+</sup> peaks are of similar intensities indicating a high surface Ti<sup>3+</sup> concentration. Furthermore, paramagnetic property of yellow TiO<sub>2</sub> obtained by SQUID is consistent with data from ESR and XPS measurements. A calculated effective magnetic moment is 0.037 Bohr magnetons. Comparison with 1.732 Bohr magnetons of the effective magnetic moment of Ti<sup>3+</sup>, it may be concluded that 2.13% of total Ti is Ti<sup>3+</sup> in yellow TiO<sub>2</sub> after calcination at 600 °C.

Defect disorder of yellow TiO<sub>2</sub> might come from either a removal of peroxo group during combustion reaction or by reduction of Ti<sup>4+</sup> at dangling bond with an electron left with it on the surface of amorphous or nanosized material. An amorphous shell character can be seen from TEM.

Yellow TiO<sub>2</sub> is photoactive under visible light. The best photocatalytic performance was observed for 600 °C calcination, probably reflecting a compromise between red shift and surface area with changing temperature. Moreover, it is reusable and activity in visible light was similar in magnitude to that in UV confirming the practicality of visible light photocatalysis at this yellow TiO<sub>2</sub>. However, doping or loading impurities into yellow TiO<sub>2</sub> prepared by this method does not enhance an overall activity.

Apart from using for photooxidation, yellow TiO<sub>2</sub> can be used in hydrogen production from photocatalytic water splitting. Hydrogen and oxygen can be produced without any sacrificial agent. It may be concluded that crystalline-amorphous core shell seen from TEM images and difference of amount of Ti<sup>3+</sup> between around 50% on surface detected by XPS and 2% in bulk detected by SQUID magnetometer might be a key factor in providing charge separation. UV and sacrificial agents was found to be helpful in accelerating hydrogen production. Ethanol is better than oxalic acid. However, doping or loading did not benefit this process, consistent to photodecolourisation of MB. It is important to note that hydrogen could be generated even under air atmosphere, which might be suitable for practical application.

The maximum quantum efficiency obtained by using yellow TiO<sub>2</sub> as photocatalyst varies from 0.03 to 0.37 for hydrogen production and from 0.03 to 0.12 for oxygen production, depending on photon energy and sacrificial agents. The quantum efficiency is very low but comparable with other reports in the case of overall water splitting into hydrogen and oxygen gas under visible light.

There are some factors might cause a low quantum efficiency in these and other photocatalysts.

- The yellow TiO<sub>2</sub> might absorb a small proportion of the photon flux compared with the chemical actinometry which the total number of photons is adsorbed by the solution. Furthermore, although the diffuse reflectance spectra of yellow TiO<sub>2</sub> showed the red shift of absorption edge into visible range, it has a small overlap

with the emitting wavelength of the lamp as shown in figure 6-1. The main absorption is in the range of 400-450 nm and 530-550 nm, which yellow TiO<sub>2</sub> can absorb around 60% and 30%, respectively. Whereas there is very small emitting wavelength of the lamp in the range of 450-530 nm. However, there may be some light lost from the light scattering on the surface too.

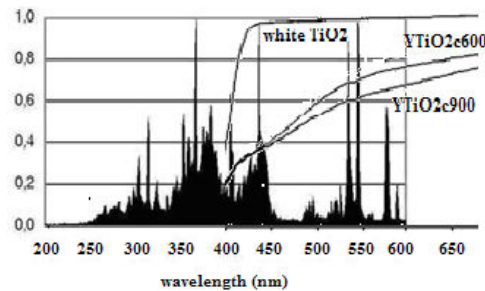


**Figure 6-1 : Illustration of the emitting wavelength of the lamp and the diffuse reflectance spectra of the yellow TiO<sub>2</sub> and the white TiO<sub>2</sub>.**

- The recombination rate of photogenerated electron hole pairs might be significant during the process as the quantum efficiency increases when using sacrificial agents.

However, this process might effective for a practical application as it can be achieved under visible light without co-catalyst and even under air atmosphere or without sacrificial agent, although the quantum efficiency is still low. Enhancing available surface area might improve this.

## REFERENCES

- [1] B. Sakintunaa, F. Darkrimb, M. Hirscher, *International Journal of Hydrogen Energy*, 2007, **32**, 1121 – 1140.
- [2] X. Vitart, A. L. Duigou and P. Carles, *Energy Conversion and Management*, 2006, **47**, 740–2747.
- [3] J.T. S. Irvine, *Journal of Power Sources*, 2004, **136**, 203–207.
- [4] M. W. Kanan and D. G. Nocera, *Science Express*, 31 July 2008.
- [5] G. Peharz, F. Dimroth and U. Wittstadt, *International Journal of Hydrogen Energy*, 2007, **32**, 3248 – 3252.
- [6] X. Wang, K. Maeda, A. Thomas, K. Takanabe, G. Xin, J. M. Carlsson, K. Domen and M. Antonietti, *Nature Materials*, 2009, **8**, 76-80.
- [7] S. S. Martinez, L. A. Sanchez, A. A. Gallegos, P. J. Sebastian, *International Journal of Hydrogen Energy*, 2007, **32**, 3159 – 3162.
- [8] H. Z. Wang, D. Y. C. Leung, M. K. H. Leung and M. Ni, *Renewable and Sustainable Energy Reviews*, 2009, **13**, 845–853.
- [9] R. B. Gonzales, V. J. Law, J. C. Prindle, *International Journal of Hydrogen Energy*, 2009, **34**, 4179-4188.
- [10] Tokio Ohta, *Applied Energy*, 2000, **67**, 181-193.
- [11] Michael Grätzel, *Nature*, 2001, **414**, 338-344.
- [12] A. Currao, *Chimia*, 2007, **61**, 815–819.
- [13] J. Nowotny, T. Bak, M. K. Nowotny and L. R. Sheppard, *International Journal of Hydrogen Energy*, 2007, **32**, 2609 – 2629.
- [14] A. A. Tahir, K. G. U. Wijayantha, *Journal of Photochemistry and Photobiology A: Chemistry*, 2010, doi:10.1016/j.jphotochem.2010.07.032

- [15] Z. Zhang, Md. F. Hossain and T. Takahashi, *International journal of hydrogen energy*, 2010, **35**, 8528-8535.
- [16] A. West, Basic Solid State Chemistry, John Wiley & Sons, Ltd, 2<sup>th</sup> edn. Ch.2, pp. 110-123.
- [17] M. R. Hoffmann, S. T. Martin, W. Choi, and D. W. Bahnemann, *Chem. Rev.*, 1995, **95**, 69-96.
- [18] A. West, Basic Solid State Chemistry, John Wiley & Sons, Ltd, 2<sup>th</sup> edn. Ch.7, pp. 315-320.
- [19] C. Kittel, Introduction to Solid State Physics, John Wiley & Sons, Ltd, 8<sup>th</sup> edn. Ch.8, pp. 187-219.
- [20] A. L. Linsebigler, G. Lu and J. T. Yates, Jr., *Chem. Rev.*, 1995, **95**, 735-758.
- [21] A. Fujishima and K. Honda, *Nature*, 1972, **238**, 37 – 38.
- [22] O. Carp, C. L. Huisman and A. Reller, *Progress in Solid State Chemistry*, 2004, **32**, 33–177.
- [23] S. Malato, J. Blanco, A. Vidal and C. Richter, *Applied Catalysis B: Environmental*, 2002, **37**, 1–15.
- [24] D. F. Ollis, *Chemistry*, 2000, **3**, 405–411.
- [25] A. V. Vorontsov, A.A. Altyinnikov, E. N. Savinov and E. N. Kurkin, *Journal of Photochemistry and Photobiology A: Chemistry*, 2001, **144**, 193–196.
- [26] A. Fujishima, X. Zhang and D. A. Tryk, *Surface Science Reports*, 2008, **63**, 515-582.
- [27] K. Sayama, K. Mukasa, R. Abe, Y. Abe and H. Arakawa, *Journal of Photochemistry and Photobiology A: Chemistry*, 2002, **148**, 71–77.

- [28] K. R. Thampi, M. S. Rao, W. Schwarz, M. Gratzel and J. Kiwi, *J. Chem. Soc., Faraday Trans. I*, 1988, **84**, 1703-1712.
- [29] A. Verma, A. Goyal, R. K. Sharma, *Thin Solid Films*, 2008, **516**, 4925–4933.
- [30] S. Ekambaram, *Journal of Alloys and Compounds*, 2008, **448**, 238–245.
- [31] J. C.-S. Wu and C.-H. Chen, *Journal of Photochemistry and Photobiology A: Chemistry*, 2004, **163**, 509–515.
- [32] M. Ashokkumar, *International Journal of Hydrogen Energy*, 1998, **23**, 427-438.
- [33] A. Kudo, *International Journal of Hydrogen Energy*, 2006, **31**, 197 – 202.
- [34] A. Kudo, *International Journal of Hydrogen Energy*, 2007, **32**, 2673 – 2678.
- [35] M. Uno, A. Kosuga, M. Okui, K. Horisaka, H. Muta, K. Kurosaki, S. Yamanaka, *Journal of Alloys and Compounds*, 2006, **420**, 291–297.
- [36] Y. Hosogi, H. Katoa and A. Kudo, *J. Mater. Chem.*, 2008, **18**, 647–653.
- [37] H. G. Kima, O. S. Beckerb, J. S. Jangb, S. M. Jib, P. H. Borseb, J. S. Leeb, *Journal of Solid State Chemistry*, 2006, **179**, 1214–1218.
- [38] Z. Zou, J. Ye, K. Sayama and H. Arakawa, *Nature*, 2001, **414**, 625-627.
- [39] D. W. Hwang, H. G. Kim, J. S. Jang, S. W. Bae, S. M. Ji and J. S. Lee, *Catalysis Today*, 2004, **93–95**, 845–850.
- [40] T. Ohno, T. Tsubota, Y. Nakamura and K. Sayama, *Applied Catalysis A: General*, 2005, **288**, 74–79.
- [41] J. Wang, S. Yin, Q. Zhang, F. Saito and T. Sato, *Solid State Ionics*, 2004, **172**, 191–195.
- [42] K. G. Kanadea, J. Baega, B. B. Kale, S. M. Lee, S. Moon and K. Kong, *International Journal of Hydrogen Energy*, 2007, **32**, 4678–4684.

- [43] L. Zhou, W. Wang, S. Liu, L. Zhang, H. Xu and W. Zhu, *Journal of Molecular Catalysis A: Chemical*, 2006, **252**, 120–124.
- [44] Y. Takahara, J. N. Kondo, D. Lu and K. Domen, *Solid State Ionics*, 2002, **151**, 305–311.
- [45] A. Kudo, R. Niishiro, A. Iwase, H. Kato, *Chemical Physics*, 2007, **339**, 104–110.
- [46] D. Guo, G. Zhang, Z. Zhang, Z. Xue and Z. Gu, *J. Phys. Chem. B*, 2006, **110**, 1571-1575.
- [47] S. Yamada, A. Y. Nosaka and Y. Nosaka, *Journal of Electroanalytical Chemistry*, 2005, **585**, 105–112.
- [48] H. Kato and A. Kudo, *Journal of Photochemistry and Photobiology A: Chemistry*, 2001, **145**, 129–133.
- [49] H. Jeong, T. Kim, D. Kim and K. Kim, *International Journal of Hydrogen Energy*, 2006, **31**, 1142 – 1146.
- [50] S. Ikeda, K. Hirao, S. Ishino, M. Matsumura and B. Ohtani, *Catalysis Today*, 2006, **117**, 343–349.
- [51] S. Matsuo, T. Omata and M. Yoshimura, *Journal of Alloys and Compounds*, 2004, **376**, 262–267.
- [52] Y. Xie and C. Yuan, *Applied Catalysis B: Environmental*, 2003, **46**, 251–259.
- [53] W. Shangguan, *Science and Technology of Advanced Materials*, 2007, **8**, 76–81.
- [54] H. Park and W. Choi, *J. Phys. Chem. B*, 2005, **109**, 11667-11674.
- [55] S. B. Zhu, T. G. Xu, H. B. Fu, J. C. Zhao, and Y. F. Zhu, *Environ. Sci. Technol.*, 2007, **41**, 6234-6239.
- [56] M. Matsuoka and M. Anpo, *Journal of Photochemistry and Photobiology C: Photochemistry Reviews*, 2003, **3**, 225–252.

- [57] S. Matsuo and M. Ueda, *Journal of Photochemistry and Photobiology A: Chemistry*, 2004, **168**, 1–6.
- [58] T. Omata and S. Otsuka-Yao-Matsuo, *Journal of Photochemistry and Photobiology A: Chemistry*, 2003, **156**, 243–248.
- [59] A. Kudo and H. Kato, *Chemical Physics Letters*, 2000, **331**, 373-377.
- [60] N. Arai, N. Saito, H. Nishiyama, K. Domen, H. Kobayashi, K. Sato and Y. Inoue, *Catalysis Today*, 2007, **129**, 407–413.
- [61] K. Maeda, K. Teramura, H. Masuda, T. Takata, N. Saito, Y. Inoue and K. Domen, *J. Phys. Chem. B*, 2006, **110**, 13107-13112.
- [62] Y. Yuan, J. Zheng, X. Zhang, Z. Li, T. Yua, J. Ye and Z. Zou, *Solid State Ionics*, 2008, **178**, 1711–1713.
- [63] K. D. Rogers, D. W. Lane, J. D. Painter and A. Chapman, *Thin Solid Films*, 2004, **466**, 97– 102.
- [64] M. Okada, M. Tazawa, P. Jin, Y. Yamada, and K. Yoshimura, *Vacuum*, 2006, **80**, 732–735.
- [65] A. Rampaul, I. P. Parkin and L. P. Cramer, *Journal of Photochemistry and Photobiology A: Chemistry*, 2007, **191**, 138–148.
- [66] A. Fujishima, X. Zhang and D. A. Tryk, *Surface Science Reports*, 2008, **63**, 515-582.
- [67] A.B. Murphy, *Solar Energy Materials & Solar Cells*, 2008, **92**, 363–367.
- [68] J. L. Gole, J. D. Stout, C. Burda, Y. Lou and X. Chen, *J. Phys. Chem. B*, 2004, **108**, 1230-1240.
- [69] J. Wuw, B. Huang, M. Wang, and A. Osaka, *J. Am. Ceram. Soc*, 2006, **89**, 2660–2663.

- [70] R. Chatti, S. S. Rayalu, N. Dubey, N. Labhsetwar, S. Devotta, *Solar Energy Materials & Solar Cells*, 2007, **91**, 180–190.
- [71] E. Kim, J. Park, G. Y. Han, *Journal of Power Sources*, 2008, **184**, 284–287.
- [72] Y. Bessekhoud, D. Robert, J. Weber and N. Chaoui, *Journal of Photochemistry and Photobiology A: Chemistry*, 2004, **167**, 49–57.
- [73] Z. Zhang and P. A. Maggard, *Journal of Photochemistry and Photobiology A: Chemistry*, 2007, **186**, 8–13.
- [74] E. A. Kozlova and A. V. Vorontsov, *Applied Catalysis B: Environmental*, 2007, **77**, 35–45.
- [75] J. Zhao, C. Chen and W. Ma, *Topics in Catalysis*, 2005, **35**, 269–278.
- [76] M. Radecka, A. Zajac, K. Zakrzewska, M. Rekas, *Journal of Power Sources*, 2007, **173**, 816–821.
- [77] C. D. Valentin, E. Finazzi, G. Pacchioni, A. Selloni, S. Livraghi, M. C. Paganini and E. Giamello, *Chemical Physics*, 2007, **339**, 44–56.
- [78] T. Ihara, M. Miyoshi, Y. Iriyama, O. Matsumoto and S. Sugihara, *Applied Catalysis B: Environmental*, 2003, **42**, 403–409.
- [79] H. Kato and A. Kudo, *J. Phys. Chem. B*, 2002, **106**, 5029–5034.
- [80] K. Iketani, R. Sun, M. Toki, K. Hirota and O. Yamaguchi, *Materials Science and Engineering B*, 2004, **108**, 187–193.
- [81] S. Yamazoe, T. Okumura and T. Tanaka, *Catalysis Today*, 2007, **120**, 220–225.
- [82] E. R. Camargo and M. Kakihana, *Chem. Mater.* 2001, **13**, 1181–1184.
- [83] M. Kakihana, M. Tada, M. Shiro, V. Petrykin, M. Osada and Y. Nakamura, *Inorg. Chem.*, 2001, **40**, 891–894.
- [84] Y. Gao, Y. Masuda, W.-S. Seo, H. Ohta and K. Koumoto, *Ceramics International*, 2004, **30**, 1365–1368.

- [85] B.R. Sankapal, M. C. Lux-Steiner and A. Ennaoui, *Applied Surface Science*, 2005, **239**, 165–170.
- [86] Z. Wang and X. Hu, *Thin Solid Films*, 1999, **352**, 62-65.
- [87] Z. Wang, J. Chen and X. Hu, *Materials Letters*, 2000, **43**, 87 – 90.
- [88] J. J. Muyco, J. J. Gray, T. V. Ratto, C. A. Orme, J. McKittrick and J. Frangos, *Materials Science and Engineering C*, 2006, **26**, 1408 – 1411.
- [89] Y. Deng, Z. Zhou, H. Wan and K. - R. Tsai, *Inorganic Chemistry Communications*, 2004, **7**, 169–172.
- [90] E. R. Camargo and M. Kakihana, *Chem. Mater.*, 2001, **13**, 1181-1184.
- [91] G. Pfaff, *Journal of the European Ceramic Society*, 1992, **9**, 121-125.
- [92] N. Uekawa, T. Kudo, F. Mori, Y. J. Wu and K. Kakegawa, *Journal of Colloid and Interface Science*, 2003, **264**, 378–384.
- [93] M. Kitano, M. Matsuoka, M. Ueshima and M. Anpo, *Applied Catalysis A: General*, 2007, **325**, 1–14.
- [94] J. Zhu and M. Zäch, *Current Opinion in Colloid & Interface Science*, 2009, **14**, 260–269.
- [95] Q. Li, Z. Chen, X. Zheng and Z. Jin, *The Journal of Physical Chemistry*, 1992, **96**, 5959-5962.
- [96] M. Yan, F. Chen, J. Zhang and M. Anpo, *J. Phys. Chem. B*, 2005, **109**, 8673-8678.
- [97] R. Spurr and H. Myers, *Analytical Chemistry*, 1957, **29**, 760-762.
- [98] [http://www.mpip-mainz.mpg.de/~andrienk/journal\\_club/xray.pdf](http://www.mpip-mainz.mpg.de/~andrienk/journal_club/xray.pdf) 12 July 2010.
- [99] R. M. German, *Powder Metallurgy Science*. New Jersey : Metal Powder Industries Federation. 1984.
- [100] <http://www.purdue.edu/REM/rs/sem.htm>. 15 July 2010.

- [101] [http://www.nhml.com/i/resources\\_NHML\\_Scanning-Electron-Microscopes\\_fig1\\_lg.gif](http://www.nhml.com/i/resources_NHML_Scanning-Electron-Microscopes_fig1_lg.gif) 15 July 2010.
- [102] FEI company, All you wanted to know about Electron Microscopy. ISBN number 90-9007755-3. 15 July 2010.
- [103] [http://en.wikipedia.org/wiki/Transmission\\_electron\\_microscopy](http://en.wikipedia.org/wiki/Transmission_electron_microscopy). 15 July 2010.
- [104] P. Atkins, T. Overton, J. Rourke, M. Weller and F. Armstrong, Shriver & Atkins Inorganic Chemistry, Oxford University press, 4<sup>th</sup> edn. Ch.6, pp. 169-195.
- [105] <http://www.chem.agilent.com/Library/usermanuals/Public/G2801-90118.pdf>. 16 October 2010.
- [106] [http://las.perkinelmer.com.cn/content/RelatedMaterials/ProductNotes/PRD\\_DiffuseReflectanceTransmittance.pdf](http://las.perkinelmer.com.cn/content/RelatedMaterials/ProductNotes/PRD_DiffuseReflectanceTransmittance.pdf). 16 July 2010.
- [107] [http://www.chem.qmul.ac.uk/surfaces/scc/scat5\\_3.htm](http://www.chem.qmul.ac.uk/surfaces/scc/scat5_3.htm). 17 July 2010.
- [108] [http://en.wikipedia.org/wiki/X-ray\\_photoelectron\\_spectroscopy](http://en.wikipedia.org/wiki/X-ray_photoelectron_spectroscopy) 17 July 2010.
- [109] W. O. Aruda, Agrenetics, Report, Wilmington, MA 01887-1319. 1999.
- [110] T. Ruiz, C. Lozano, V. Tomas and M. Iniesta, *Microchim. Acta*, 2005, **149**, 67–72.
- [111] K. Maeda, K. Teramura, H. Masuda, T. Takata, N. Saito, Y. Inoue and K. Domen, *J. Phys. Chem. B*, 2006, **110**, 13107-13112.
- [112] M. Zalas and M. Laniecki, *Solar Energy Materials & Solar Cells*, 2005, **89**, 287–296.
- [113] K. Lee, W. S. Nam and G. Y. Han, *International Journal of Hydrogen Energy*, 2004, **29**, 1343 – 1347.
- [114] M. Uno, A. Kosuga, M. Okui, K. Horisaka and S. Yamanaka, *Journal of Alloys and Compounds*, 2005, **400**, 270–275.

- [115] <http://www.uv-light.co.uk/pdfs/datasheets/DSC-UV250HL.pdf>
- [116] H. J. Kuhn, S. E. Braslavsky and R. Schmidt, *Pure Appl. Chem.*, 2004, **76**, 2105–2146.
- [117] G. M. Eisenberg, *Industrial Engineering Chemistry*, Vol. 15, No. 5.
- [118] Gilbert H. Ayres, Edmay M. Vienneau, *Ind. Eng. Chem. Anal. Ed.*, 1940, **12**, 96-96.
- [119] M. Dakanali, E. T. Kefalas, C. P. Raptopoulou, A. Terzis, G. Voyiatzis, I. Kyrikou, T. Mavromoustakos and A. Salifoglou, *Inorganic Chemistry*, 2003, **42**, 4632-4639.
- [120] D. Srinivas, P. Manikandan, S. C. Laha, R. Kumar and P. Ratnasamy, *Journal of Catalysis*, 2003, **217**, 160–171.
- [121] J. Jun, J. Shin and M. Dhayal, *Applied Surface Science*, 2006, **252**, 3871–3877.
- [122] H. Jensen, A. Soloviev, Z. Li and E. G. Søgaard, *Applied Surface Science*, 2005, **246**, 239–249.
- [123] F. Bonino, A. Damin, G. Ricchiardi, M. Ricci, G. Spano, R. D'Aloisio, A. Zecchina, C. Lamberti, C. Prestipino and S. Bordiga, *J. Phys. Chem. B*, 2004, **108**, 3573-3583.
- [124] T. Hirakawa, K. Yawata and Y. Nosaka, *Applied Catalysis A: General*, 2007, **325**, 105–111.
- [125] W. Lin and H. Frei. *J. Am. Chem. Soc.*, 2002, **124**, 9292-9298.
- [126] J. H. Lee and Y. S. Yang, *Journal of the European Ceramic Society*, 2005, **25**, 3573.
- [127] A. L. Castro, M. R. Nunes, M. D. Carvalho, L. P. Ferreira, J. -C. Jumas, F. M. Costa and M. H. Florencio, *Journal of Solid State Chemistry*, 2009, **182**, 1838–1845.

- [128] J. Yuan, M. Chen, J. Shi and W. Shangguan, *International Journal of Hydrogen Energy*, 2006, **31**, 1326 – 1331.
- [129] H. Nakajima, T. Mori, Q. Shen and T. Toyoda, *Chemical Physics Letters*, 2005, **409**, 81–84.
- [130] M. Radecka and M. Rekas, *Journal of the European Ceramic Society*, 2002, **22**, 2001–2012.
- [131] R. A. J. Borg. Explosives Ordnance Division, Aeronautical and Maritime Research Laboratory. DSTO-TR-0065. Report. Melbourne, Victoria.
- [132] J. Wang, T. Ma, Z. Zhang, X. Zhang, Y. Jiang, G. Zhang, G. Zhao, H. Zhao and P. Zhang, *Ultrasonics Sonochemistry*, 2007, **14**, 246–252.
- [133] M. Ocana, V. Fornes, J. V. Garcia Ramos and C. J. Serna, *Journal of Solid State Chemistry*, 1988, **75**, 364-372.
- [134] T. L. Thompson, O. Diwald, and J. T. Yates, Jr., *J. Phys. Chem. B*, 2003, **107**, 11700-11704.
- [135] J. Yu, J. Chen, C. Li, X. Wang, B. Zhang and H. Ding, *J. Phys. Chem. B*, 2004, **108**, 2781-2783.
- [136] P. F. Cornaz, J. H. C. van Hooff, F. J. Pluijma and G. C. A. Schuit, *Discussions of the Faraday Society*, 1966, **41**, 290-304.
- [137] K. Suriye, B. Jongsomjit, C. Satayaprasert and P. Praserttham, *Applied Surface Science*, 2008, **255**, 2759–2766.
- [138] Y. Nakaoka and Y. Nosaka, *Journal of Photochemistry and Photobiology A: Chemistry*, 1997, **110**, 299-305.
- [139] S. Joung, T. Amemiya, M. Murabayashi and K. Itoh, *Applied Catalysis A: General*, 2006, **312**, 20–26.

- [140] P. M. Jayaweera, E. L. Quah, and H. Idriss, *J. Phys. Chem. C*, 2007, **111**, 1764-1769.
- [141] I. Bertoti, *Surface and Coatings Technology*, 2002, **151–152**, 194–203.
- [142] N. Jiang, H. J. Zhang, S. N. Bao, Y. G. Shen and Z. F. Zhou, *Physica B*, 2004, **352**, 118–126.
- [143] M. A. Baker, S. J. Greaves, E. Wendler and V. Fox, *Thin Solid Films*, 2000, **377-378**, 473-477.
- [144] C. Liang, G. Cheng, R. Zhenga, H. Liu, J. Li, H. Zhang, G. Ma and Y. Jiang, *Surface & Coatings Technology*, 2007, **201**, 5537–5540.
- [145] M. Balaceanu, M. Braic, D. Macoveia, M. J. Genetb, A. Maneaa, D. Pantelicac, V. Braica and F. Negoitac, *Journal of Optoelectronics and Advanced Materials*, 2002, **4**, 107-114.
- [146] I. Takahashi, D.J. Payne, R.G. Palgrave, R.G. Egdell *Chemical Physics Letters* 454 (2008) 314–317.
- [147] Y. Matsumoto, M. Murakami, T. Shono, T. Hasegawa, T. Fukumura, M. Kawasaki, P. Ahmet, T. Chikyow, S. Koshihara and H. Koinuma, *Science*, 2001, **291**, 854-856.
- [148] A. K. Rumaiz, B. Ali, A. Ceylan, M. Boggs, T. Beebe and S. I. Shah, *Solid State Communications*, 2007, **144**, 334–338.
- [149] K. A. Regan, Q. Huang, M. Lee, A. P. Ramirez and R.J. Cava, *Journal of Solid State Chemistry*, 2006, **179**, 195–204.
- [150] G. Glaspell and A. Manivannan, *Journal of Cluster Science*, 2005, **16**, 501-513.
- [151] J. M. Coronado, A. J. Maira, J. C. Conesa, K. L. Yeung, V. Augugliaro and J. Soria, *Langmuir*, 2001, **17**, 5368-5374.
- [152] W. F. Zhang, Z. Yin and M. S. Zhang, *Appl. Phys. A*, 2000, **70**, 93–96.

- [153] D. Cao, M. Q. Cai, Y. Zheng and W. Y. Hu, *Phys. Chem. Chem. Phys.*, 2009, **11**, 10934–10938.
- [154] A. Mills and J. Wang, *Journal of Photochemistry and Photobiology A: Chemistry*, 1999, **127**, 123–134.
- [155] S. Lee and A. Mills, *Chem. Commun*, 2003, 2366–2367.
- [156] S. Yamazaki and N. Nakamura, *Journal of Photochemistry and Photobiology A: Chemistry*, 2008, **193**, 65–71.
- [157] X. Yan, T. Ohno, K. Nishijima, R. Abe and B. Ohtani, *Chemical Physics Letters*, 2006, **429**, 606–610.
- [158] L. Cui, R. Ruffo, C. K. Chan, H. Peng and Y. Cui, *Nano Letters*, 2009, **9**, 491–495.
- [159] Y. L. Chueh, Z. Fan, K. Takei, H. Ko, R. Kapadia, A. A. Rathore, N. Miller, K. Yu, M. Wu, E. E. Haller and A. Javey, *Nano Lett*, 2010, **10**, 520–523.
- [160] D. Zhang, H. Hu, L. Li and D. Shi, *Journal of Nanomaterials*, Volume 2008, Article ID 271631, 4 pages doi:10.1155/2008/271631.
- [161] A. Bojinova, R. Kralchevska, I. Poullos and C. Dushkin, *Materials Chemistry and Physics*, 2007, **106**, 187–192.
- [162] S. Bakardjieva, J. Subrt, V. Stengl, M. J. Dianez and M. J. Sayagues, *Applied Catalysis B: Environmental*, 2005, **58**, 193–202.
- [163] H. Harada, C. Hosoki, A. Kudo, *Journal of Photochemistry and Photobiology A: Chemistry*, 2001, **141**, 219–224.
- [164] F. Bosc, A. Ayrat, N. Keller and V. Keller, *Applied Catalysis B: Environmental*, 2007, **69**, 133–137.
- [165] M. Hiranow and K. Matsushima, *J. Am. Ceram. Soc.*, 2006, **89**, 110–117.
- [166] R. Beranek and H. Kisch. *Photochem. Photobiol.Sci*, 2008, **7**, 40.

- [167] J. Wang, D. N. Tafen, J. P. Lewis, Z. Hong, A. Manivannan, M. Zhi and N. Wu. *J. Am. Chem. Soc.*, 2009, **131**, 12290-12297.
- [168] H. Kominami, K. Oki, M. Kohno, S. Onoue, Y. Keraa and B. Ohtanib, *J. Mater. Chem.*, 2001, **11**, 604-609.
- [169] J. C. Kennedy and A. K. Datye, *Journal of Catalysis*, 1998, **179**, 375–389.
- [170] Y. Z. Yang, C. Chang and H. Idriss, *Applied Catalysis B: Environmental*, 2006, **67**, 217–222.
- [171] M. M. Kosanic, *Journal of Photochemistry and Photobiology A: Chemistry*, 1998, **119**, 119-122.
- [172] V. Iliev, D. Tomova, L. Bilyarska and G. Tyuliev, *Journal of Molecular Catalysis A: Chemical*, 2007, **263**, 32–38.
- [173] Y. Li, G. Lu and S. Li, *Applied Catalysis A: General*, 2001, **214**, 179–185.
- [174] S. Yamamoto and R. A. Back, *J. Phys. Chem.* 1985, **89**, 622-625.
- [175] Y. Li, G. Lu and S. Li, *Chemosphere*, 2003, **52**, 843–850.
- [176] W. Y. Teoh, R. Amal, L. Madler, and S. E. Pratsinis, *Catalysis Today*, 2007, **120**, 203–213.
- [177] J. Nowotny, T. Bak, M. K. Nowotny and L. R. Sheppard, *International Journal of Hydrogen Energy*, 2007, **32**, 2630 – 2643.
- [178] G. L. Chiarello, E. Selli and L. Forni, *Applied Catalysis B: Environmental*, 2008, **84**, 332–339.
- [179] A. Hameed and M. A. Gondal, *Journal of Molecular Catalysis A: Chemical*, 2004, **219**, 109–119.
- [180] K. Maeda, T. Takata, M. Hara, N. Saito, Y. Inoue, H. Kobayashi and K. Domen, *J. Am. Chem. Soc.* 2005, **127**, 8286-8287.
- [181] D. Lu, T. Takata, N. Saito, Y. Inoue and K. Domen, *Nature*, 2006, **440**, 295-295.